Catarina Isabel Parente Chaparro

Licenciatura em Bioquímica

Application of Hyperthermia for Cancer Treatment: Synthesis and Characterization of Magnetic Nanoparticles and their internalization on Tumor Cell Lines

Dissertação para obtenção do Grau de Mestre em Biotecnologia

Orientador: Doutora Paula Isabel Pereira Soares, DCM – FCT/UNL

Co-Orientador: Professora Doutora Paula Alexandra Quintela Videira, DCV – FCT/UNL

Júri:

Presidente:	Professora Doutora Ana Cecília Afonso Roque
Arguente:	Doutora Vera Luísa Santos Neves
Vogais:	Doutora Paula Isabel Pereira Soares
	Professora Doutora Paula Alexandra Quintela Videira

FACULDADE DE CIÊNCIAS E TECNOLOGIA
UNIVERSIDADE NOVA DE LISBOA

Outubro 2017

Catarina Isabel Parente Chaparro

Licenciatura em Bioquímica

Application of Hyperthermia for Cancer Treatment: Synthesis and Characterization of Magnetic Nanoparticles and their internalization on Tumor Cell Lines

Dissertação para obtenção do Grau de Mestre em Biotecnologia

Orientador: Doutora Paula Isabel Pereira Soares, DCM – FCT/UNL

Co-Orientador: Professora Doutora Paula Alexandra Quintela Videira, DCV – FCT/UNL

Júri:

Presidente: Professora Doutora Ana Cecília Afonso Roque

Arguente: Doutora Vera Luísa Santos Neves

Vogais: Doutora Paula Isabel Pereira Soares

Professora Doutora Paula Alexandra Quintela Videira

Outubro 2017

Application of Hyperthermia for Cancer Treatment: Synthesis and Characterization of Magnetic Nanoparticles and their internalization on Tumor Cell Lines

“The limits of the possible can only be defined by

going beyond them into the impossible.”

Arthur C. Clarke

Acknowledgments

Em primeiro lugar, quero agradecer à minha orientadora, Doutora Paula Soares por todo o apoio prestado ao longo do desenvolvimento do meu trabalho, pela constante disponibilidade e ensinamento. Não só por estes motivos devo muito à Paula, agradeço a amizade e os conselhos, o incentivo a fazer melhor e a não desistir das minhas ambições!

Agradeço à minha co-orientadora, Professora Paula Videira, pela oportunidade que me proporcionou em fazer parte do seu grupo de investigação. Foi importante, para além do meu trabalho, ter contacto com os variados temas de investigação explorados pelo Glycoimmunology Group.

Ao Professor João Paulo Borges por me receber no seu laboratório de Biomateriais, pelo esclarecimento de dúvidas importantes e por todo o apoio prestado.

Um muito obrigado à aluna de doutoramento Liliana Loureiro, que mesmo ausente, esteve sempre a par do percurso do meu projeto e que contribui muito para o bom desenvolvimento do meu trabalho. Agradeço de igual forma à Mariana Amaro, a rápida prontificação em ajudar nas minhas necessidades. Obrigado meninas!

Aos Professores César Laia e Jaime Mota pela disponibilidade oferecida para a utilização do aparelho de DLS e do microscópio de fluorescência, respectivamente.

À Augusta, à Susete, à Ana Baptista, à Coro, à Ana Almeida e ao João Canejo pelo apoio prestado no laboratório de Biomateriais e pela boa disposição no trabalho.

Aos meus colegas deste laboratório, um especial agradecimento à Paula, à Maïssa, ao Jaime, ao Miguel e ao Ricardo pelo companheirismo, por nos aturarmos uns aos outros e pelos momentos de convívio. Agradeço ainda pela ajuda com o software Origin (salvaram-me!).

Aos meus colegas do Glycoimmunology Group: à Carlota, à Constança, à Roberta, à Fanny, ao Tiago e à Myléne, obrigado por todos os ensinamentos, pela vossa disponibilidade para o esclarecimento de qualquer dúvida e ainda pelos momentos de descontração e risada completa.

Por último, o maior agradecimento vai para aqueles que me apoiaram fora das bancadas do lab e me deram força para cada dia de trabalho, para cada mau resultado a ultrapassar, acreditando sempre no meu sucesso. Por isso, ao Bernardo faço um agradecimento especial por tudo aquilo que fez por mim, principalmente nas alturas mais complicadas da tese! Às minhas amigas, em especial à Carolina, a minha primeira amiga da faculdade e que sempre esteve presente.

Aos meus pais, à minha irmã, à minha madrinha e às minhas avós pelo carinho e apoio intermináveis, pela força que me deram e pela fé que em mim depositaram. Obrigado por me terem feito ver o quão gratificante é a recompensa. A vocês, o maior obrigado do mundo!

Resumo

O cancro é uma doença devastadora dos dias atuais com uma grande incidência e mortes associadas. Atualmente, a abordagem mais importante no tratamento do cancro é a cirurgia na remoção de tumores sólidos. Outras terapêuticas, como quimioterapia e radioterapia, são atualmente utilizadas no tratamento da doença. As respostas tumorais às terapias tradicionais são geralmente parciais, breves, imprevisíveis e associadas a alta resistência. É, portanto, necessária uma nova abordagem no tratamento do cancro, mais eficaz, mais específica e capaz de aumentar a qualidade de vida do paciente. Uma opção de tratamento alternativa é a utilização de nanopartículas magnéticas (mNPs) para a indução de hipertermia intracelular. A hipertermia é uma técnica antiga capaz de conduzir à morte de células cancerosas sem o uso de fármacos (quimioterapia) ou radiação (radioterapia) apenas pelo aumento da temperatura no local do tumor. Este método baseia-se na maior sensibilidade das células cancerosas a oscilações de temperatura quando comparada às células normais, diminuindo assim os efeitos colaterais.

Por isso, nesta tese de mestrado foi proposto o desenvolvimento e caracterização de nanopartículas superparamagnéticas constituídas por óxidos de ferro, tendo em vista a sua internalização em linhas celulares cancerosas para posteriores ensaios de hipertermia magnética *in vitro*. Um outro ponto a atingir seria a funcionalização destas nanopartículas magnéticas com um anticorpo monoclonal contra o antigénio sialil-Tn, um carbohidrato associado a tumores, sendo expresso por vários tipos de cancro. Desta forma, a prensença deste anticorpo tornaria o sistema altamente específico.

As nanopartículas foram caracterizadas por várias técnicas em diferentes fases do trabalho. Foram obtidas partículas com uma estrutura cubica cristalina simples caracterizada por difração de raio-X; com um tamanho médio de 8 nm obtido por microscopia eletrónica de transmissão; e com um diâmetro hidrodinâmico de 147.3 ± 5.5 nm e 57.1± 1.7 nm para as nanopartículas revestidas com ácido oleico e com ácido dimercaptosuccínico (DMSA), respectivamente, obtido por dispersão dinâmica da luz. De forma a perceber a internalização celular das nanopartículas revestidas, duas linhas celulares de cancro da mama foram utilizadas, comprovando-se uma maior internalização das nanopartículas revestidas com DMSA bem como uma maior acumulação de mNPs na linha celular cancerosa que expressa o antigénio sialil-Tn.

Por estes motivos, as propriedades das nanopartículas magnéticas produzidas nesta tese de mestrado consideram-se como as indicadas para representarem as mesmas como excelentes geradores de calor para a sua aplicação em hipertermia magnética *in vitro*.

Palavras-chave: Cancro, Hipertermia magnética, Nanoparticulas de óxido de ferro, Internalização celular, Antigénio sialil-Tn.

Abstract

Cancer is a devastating disease of the present days with a huge incidence and related deaths. Currently, the most important approach in cancer treatment is surgery that removes the solid tumor. Other therapeutics such as chemotherapy and radiotherapy are currently used in cancer treatment. Tumor responses to traditional therapeutics are usually partial, brief, unpredictable, and associated with high resistance. In view of this, there is a need for a new approach in cancer treatment, more effective, more specific and capable of increasing the patient quality of life. One alternative treatment option is the use of magnetic nanoparticles (mNPs) for the induction of intracellular hyperthermia. Hyperthermia is an old technique capable of killing cancer cells without the use of drugs (chemotherapy) or radiation (radiotherapy) just by increasing temperature in the tumor site. This idea is based on the higher sensitivity of cancer cells to temperature oscillations when compared to normal cells, therefore decreasing the side effects.

Therefore, in this master's thesis the development and characterization of superparamagnetic iron oxide nanoparticles was proposed, in view of their internalization in cancer cell lines for later *in vitro* magnetic hyperthermia assays. Another important point would be the functionalization of these magnetic nanoparticles with a monoclonal antibody against sialyl-Tn antigen, a tumor-associated carbohydrate antigen that is expressed by several carcinomas. In this way, the presence of this antibody would provide high specificity to the system.

Nanoparticles were characterized by several techniques at different stages of the work. Particles were obtained with a simple crystalline cubic structure characterized by X-ray diffraction; with an average size of 8 nm obtained by transmission electron microscopy; and a hydrodynamic diameter of 147.3 ± 5.5 nm and 57.1 ± 1.7 nm for nanoparticles coated with oleic acid and dimercaptosuccinic acid (DMSA), respectively, obtained by dynamic light scattering. In order to understand the cellular internalization of the coated nanoparticles, two breast cancer cell lines were used, proving a greater internalization of the nanoparticles coated with DMSA as well as a greater accumulation of mNPs in the cancer cell line that expresses the sialyl-Tn antigen.

For these reasons, the properties of the produced magnetic nanoparticles in this master's thesis are considered as those indicated to represent them as excellent heat generators for their application in magnetic hyperthermia *in vitro*.

Keywords: Cancer, Magnetic hyperthermia, Iron oxide nanoparticles, Cellular internalization, Sialyl-Tn antigen.

Table of Contents

Figure Index

Table Index

List of Abbreviations

AAS	Adsorption spectroscopy
AC	Alternating Current
ACF	Auto-Correlation Function
AMF	Alternating magnetic field
ATR	Attenuated total reflectance
cDNA	Complementary DNA
DC	Direct Current
D_H	Hydrodynamic Diameter
dH_2O	Deionized water
DLS	Dynamic Light Scattering
DMEM	Dulbecco's modified Eagle's medium
DMSA	Dimercaptosuccinic acid
DMSO	Dimethyl sulfoxide
DNA	Deoxyribonucleic acid
EDC	1-ethyl-3-(-3-dimethylaminopropyl) carbodiimide hydrochloride
ER	Endoplasmic reticulum
FBS	Fetal Bovine Serum
FDA	Food and Drug Agency
FITC	Fluorescein isothiocyanate
fsc	Forward-scatter
FTIR	Fourier Transform Infrared spectroscopy
Gal	Galactose
GalNAc	*N*-acetylgalactosamine
GlcNAc	*N*-acetylglucosamine
ICP-MS	Inductively coupled plasma mass spectrometry

mAb(s)	Monoclonal Antibody (Antibodies)
MFI	Median intensity fluorescence
mNPs	Magnetic nanoparticles
MPS	Magnetic particle spectroscopy
MRI	Magnetic resonance imaging
MTS	3-(4,5-dimethylthiazol-2-yl)-5-(3-carboxymethoxyphenyl)-2-(4-sulfophenyl)-2H-tetrazolium
MTT	3-(4,5-dimethylthiazol-2-yl)-2,5-diphenyltetrazolium bromide
MWCO	Molecular Weight Cut Off
Neu	Neuraminic acid
Neu5Ac	*N*-acetylneuraminic acid
NHS	N-hydroxysuccinimide
NMR	Nuclear magnetic resonance
NP(s)	Nanoparticle(s)
OA	Oleic acid
OD	Optical Density
OSM	Ovine submaxillary mucin
PBS	Phosphate Buffer Saline
PDT	Photodynamic therapy
RES	Reticuloendothelial system
ROS	Reactive oxygen species
RT	Room temperature
SAR	Specific absorption rate
Ser	Serine
SPIONs	Superparamagnetic iron oxide nanoparticles
SQUID	Superconducting Quantum Interference Device
ssc	Side-scatter

STn	Sialyl-Tn antigen
T or TF	Thomsen–Friedenreich
TE	Trypsin-EDTA
TEM	Transmission Electron Microscopy
Thr	Threonine
UDP-GalNAc	Uridine diphosphate *N*-acetylgalactosamine
UV	Ultraviolet
UV-Vis	Ultraviolet-visible
VSM	Vibrating sample magnetometer
WT	Wild type
XRD	X-Ray Diffraction

Symbols

μ	Ionic strength
μ_0	Magnetic permeability of free space
H	Applied Magnetic field
H_c	Coercivity
m	Magnetic moment
M	Magnetization
M_r	Remanence
M_s	Saturation magnetization
T	Temperature
T_1	Tranverse relaxation
T_2	Longitudinal relaxation
V	Volume
η	Viscosity
λ	Wavelength

τ	Relaxation time
χ	Magnetic susceptibility

Part I

General Introduction

1. Cancer

1.1 The hallmarks of cancer

Cancer is one of the leading causes of death worldwide (Figure 1.1), along with cardiovascular and neurodegenerative diseases, diabetes and chronic pulmonary diseases. In the next twenty years, the number of new cases is expected to increase by about 70%. Thus, it is important that this disease can be correctly and early diagnosed and that effective treatments that allow its cure or that can considerably prolong the patient's life are made available (World Health Organization 2015; US National Center For Health Statistics).

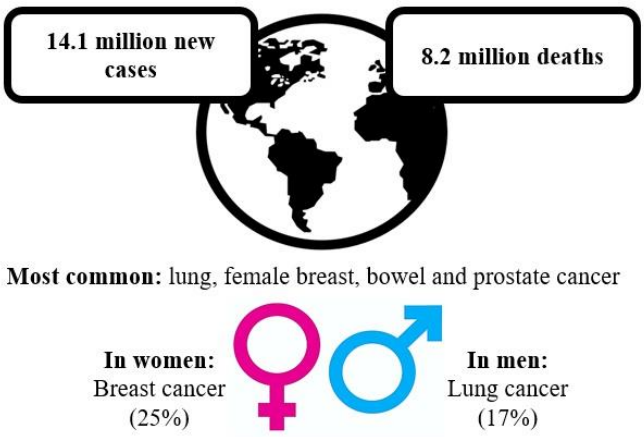

Figure 1.1. Worldwide cancer statistics: number of new cases and deaths in 2012. Most common cancers (general), and top cancers affecting woman and men. Adapted from (Cancer Research UK 2014a; Cancer Research UK 2014b).

This disease results from the accumulation of somatic mutations in the progeny of normal cells, which generates abnormal cells with a selective growth advantage and with an upregulated and uncontrolled capacity of proliferation. Cancer cells can also undergo a process known as metastasizing, in which they gain the ability of invading adjacent normal tissues and organs and spread to distant sites throughout the body, which is the main cause of death related with this disease. These mutations are mostly related with deoxyribonucleic acid (DNA) repair genes, tumor suppressor genes and proto-oncogenes, arising from exposure to physical and chemical agents, from infection with viruses, from genetic predisposition and from behaviors related with known risk factors, like smoking (Cooper 2000; Blanpain 2013). The type of cell from which a tumor arises classifies it: tumors that arise from epithelial cells are named carcinomas, tumors with origin on connective tissues are named sarcomas, tumors that arise from cells of the immune system are called lymphomas and tumors generated from blood-forming cells are named leukemias. They can also be further classified according to their primary site (Cooper 2000).

Several aspects of the cell behavior distinguish cancer cells from their normal equivalents. These aspects, known as the hallmarks of cancer, are acquired functional abilities that allow cancer cells to survive, proliferate, and disseminate. Hanahan and Weinberg (Hanahan and Weinberg 2000) defined rules that govern the transformation of normal human cells into malignant cancers. These six essential alterations in cell physiology are manifested as different cancer genotypes, although they are shared in common by most or even all human tumors. The six hallmarks of cancer defined by these authors in 2000 are the following:

- Self-sufficiency in growth signals: tumor cells are able to stimulate their own growth;
- Insensitivity to anti-growth signals: the inhibitory signals that normally govern normal cells proliferation and homeostasis do not have affect tumor cells;
- Evasion of programmed cell death (apoptosis): tumor cells are able to evade apoptosis and express less surface adhesion molecules, which results in morphological and cytoskeletal modifications which ensure their survive;
- Limitless replicative potential: contrary to normal cells, tumor cells are able to replicate indefinitely;
- Sustained angiogenesis: tumors are able to stimulate the growth of blood vessels to supply nutrient to their own cells;
- Tissue invasion and metastasis: cancer cells secrete proteases, such as collagenase, that digest components of the extracellular matrix, allowing them to invade the adjacent normal tissues and spread to distant sites once they can invade nearby blood and lymphatic vessels.

The acquisition of each of these hallmarks capabilities explain the evolution of normal cells to progressively become tumoral cells. With the combination of these traits, tumor cells are able to survive, proliferate, and disseminate. However, a decade of research later led to a change in the notion that tumor development was exclusively dependent on the tumor cells. Instead, to a better understanding of the biology of tumors, one must consider the contribution of the tumor microenvironment. Tumors are complex tissues composed of multiple distinct cell types that participate in heterotypic interactions with one another (Hanahan and Weinberg 2011).

1.2 The next generation of cancer hallmarks

The above-described hallmarks of cancer are acquired functional capabilities that allow cancer cells to survive, proliferate, and disseminate. These functions are acquired in different tumor types via distinct mechanisms and at various times during the course of multistep tumorigenesis. The acquisition of such characteristics is made possible by two enabling characteristics:

- Genomic instability and mutation in cancer cells;
- Inflammatory state of premalignant and frankly malignant lesions.

In addition, two other attributes of cancer cells have been proposed to be functionally important for the development of cancer and were therefore added to the list of core hallmarks:

- Deregulating cellular energetics;
- Avoiding immune destruction.

The first attribute is a consequence of the need to support continuous cell growth and proliferation, which involves a major reprogramming of cellular energy metabolism. In this case, the metabolic program that operates in most normal tissues and fuels the physiological operations of the associated cells is replaced. The second attribute is related to an active evasion by cancer cells from attack and elimination by immune cells. In both cases, these two attributes may facilitate the development and progression of many forms of human cancers (Hanahan and Weinberg 2011).

The six core hallmarks defined in 2000 provide a solid framework for understanding the complex biology of cancer. Nevertheless, the extended concept of cancer hallmarks and the definition of the emerging hallmark capabilities and enabling characteristics have provided the basis for the development of new means to treat human cancer. The understanding of the tumor microenvironment functionality and importance during tumorigenesis is crucial for the development of new and more effective cancer treatments.

2. Glycosylation

Glycosylation is the most common post-translational modification of proteins, having an important role on many biological functions, as immunity, cellular communication and protein folding, trafficking and activity (Moremen *et al.* 2012; Varki 1993).

Glycosylation is an enzymatic process by which glycosidic linkages are created, allowing saccharides to be bound to other saccharides, lipids or proteins, and generating glycoconjugates. The diversity of glycans (term often applied to name the carbohydrate part of a glycoconjugate) derives from the ways in which monosaccharides can be linked together. Differences in monosaccharide composition, substitutions in the existing glycans, the presence or not of branching structures and the different linkages – to other carbohydrates, to proteins or to lipids – all contribute to an increasing diversity of glycans (Pinho and Reis 2015; Bertozzi and Rabuka 2009). For this reason, a nomenclature strategy was adopted by the Nomenclature Committee of the Consortium for Functional Glycomics (CFG) (Consortium for Functional Glycomics 2012). This strategy provides a consistent system to represent glycan structures by both symbols and text (see Appendix I).

In eukaryotic cells, most of the secreted and cell-surface molecules originate in the endoplasmic reticulum (ER). They are then distributed from the trans-Golgi network to several

destinations and, in the process, proteins and lipids are modified by a series of glycosylation reactions. However, not all glycans are assembled within the ER-Golgi pathway, as some modifications occur in the cytoplasm and others at the plasma membrane. Nucleotide sugars (activated forms of monosaccharides) are often transferred in glycosylation reactions, which are mediated by glycosyltransferases, to the glycan being synthetized (Varki *et al.* 2009). The biological roles of glycans are broadly classified in four categories, all involving glycan-binding proteins: structural and modulatory roles, intrinsic recognition, extrinsic recognition and molecular mimicry of host glycans (Varki and Lowe 2009). The two general classes of protein-bound glycans occur via linkages to oxygen (*O*-glycosylation) or nitrogen (*N*-glycosylation). The process of *N*-glycosylation generates *N*-glycans through the binding of *N*-acetylglucosamine (GlcNAc) residues to the amide groups of asparagine (Asn) side chains. The process of *O*-glycosylation generates *O*-glycans, in which *N*-acetylgalactosamine (GalNAc) residues are linked to the oxygen atom of threonine (Thr) or serine (Ser) side chains (Figure 2.1) (Pinho and Reis 2015; Bertozzi and Rabuka 2009).

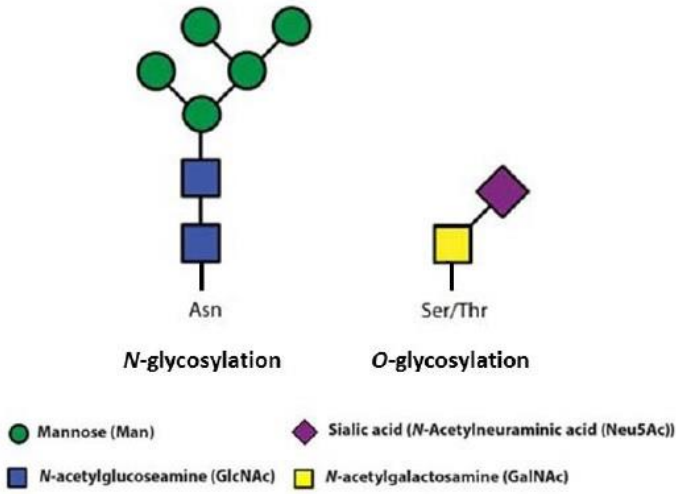

Figure 2.1. Schematic representation of a *N*-glycosylated glycoprotein (left) and of a *O*-glycosylated glycoprotein (right). Adapted from (R. Nordén).

2.1 *O*-glycosylation

Glycoproteins are often heavily *O*-glycosylated, particularly serine- and threonine-rich mucins that constitute mucous secretions and can also be found on the cell surface as transmembrane glycoproteins. The biosynthesis of *O*-glycan chains occurs in the Golgi apparatus and involves the sequential action of different glycosyltransferases. Thus, the pattern of *O*-glycans that is expressed on a certain cell depends on the level of expression, localization and substrate specificity of the glycosyltransferases. The structures generated by these enzymes can be further modified through processes such as sialylation, acetylation and fucosylation (Bertozzi and

Rabuka 2009; Reis *et al.* 2010; Steen *et al.* 1998). The initial step of *O*-glycosylation involves the transfer of a GalNAc residue from uridine diphosphate *N*-acetylgalactosamine (UDP-GalNAc) to a threonine or to a serine in the amino acid chain, generating the Tn antigen (GalNAc-Ser/Thr), which is the simplest mucin *O*-glycan and will be mentioned later in this section. The chain is then further elongated (Munkley 2016; Cazet *et al.* 2010; Brockhausen and Stanley 2015).

2.2 Sialic Acids

One of the modifications than can occur on glycan structures is sialylation, through the addition of monosaccharides, named sialic acids, which comprise a group of approximately 50 different chemical derivatives of neuraminic acid (Neu). In mammalian cells, the most common variant is the *N*-acetylneuraminic acid (Neu5Ac), with a *N*-acetyl group on carbon 5 (Figure 2.2) (Schultz *et al*. 2012; Varki and Schauer 2009).

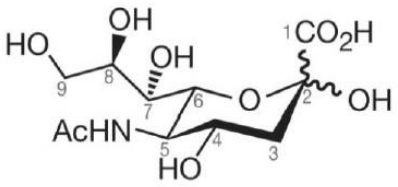

Figure 2.2. Structure of *N*-acetylneuraminic acid (Neu5Ac) (Varki and Schauer 2009)**.**

Sialic acids exhibit a significant diversity due to the different alpha linkages that can be formed. They are commonly found in the terminal positions of *N*- and *O*-glycans of glycoproteins and are added by action of specific sialyltransferases that use cytidine monophosphate-sialic acid (CMP-sialic acid) as donors (Schultz *et al.* 2012; Varki and Schauer 2009). These monosaccharides have several biological roles, such as the stabilization of membranes and molecules and the modulation of interactions of the molecules and cells with the environment; they can also serve as a biological target, allowing its recognition by a receptor protein, or shield antigenic sites and receptors, protecting molecules from the action of proteases or glycosidases and weakening the immune-reactivity (Varki and Schauer 2009; Schauer 2000).

2.3 Sialyltransferases and Sialidases

Sialylation of glycoproteins is a modification that occurs in glycans and is associated to cancer. The level of cell surface sialylation is regulated by a diverse group of enzymes. This group includes the enzymes that control the synthesis and availability of the activated donor substrate (CMP-sialic acid); sialyltransferases, the enzymes that add the sialic acids; and sialidases (or neuraminidases), the enzymes that remove the sialic acids. Most of the sialyltransferases are

localized in the Golgi apparatus, since sialic acids are added during the biosynthesis of the glycoproteins, while sialidases are usually found in lysosomes or endosomes, for the removal of sialic acids during the degradation of glycoproteins (Schultz *et al*. 2012).

Sialyltransferases are a family of enzymes that vary in tissue distribution and on the type of sialic acid linkage that they perform. Sialic acids can be added by ST3Gal-I sialyltransferase in an α2-3 linkage to galactose (Gal); by ST6Gal-I and ST6Gal-II sialyltransferases in an α2-6 linkage to galactose or by ST6GalNAc sialyltransferases to *N*-acetylgalactosamine; or by the family of polysialyltransferases in an α2-8 linkage to other sialic acid. Aberrant expression of these enzymes, as well as of sialidases, is observed in cancer (Schultz *et al.* 2012).

3. Glycosylation and Cancer: Tumor-Associated Carbohydrate Antigens

Glycosylation can be essential for the regulation of several physiopathological mechanisms. For this reason, variations in the resulting glycoconjugates can interfere with cancer cell processes, such as inflammation and immune surveillance, and with the tumor microenvironment, as they are associated with oncogenic transformation, cancer growth, progression and metastasis. Cancer cells exhibit a diverse series of differences on the levels and types of carbohydrate structures present on their surfaces. These carbohydrate structures allow them to be distinguished from normal cells and are known as tumor-associated carbohydrate antigens (TACAs). Alterations in the glycans present at the surface of the cell can result from abnormal expression and activity of glycosyltransferases or to their incorrect location in the Golgi apparatus (Pinho and Reis 2015; Feng *et al*. 2016).

The two main processes of tumor-associated carbohydrate alteration are the neo-synthesis and the incomplete synthesis. The first one is commonly observed in more advanced stages of cancer and results of a cancer-associated induction of genes that are related with the expression of carbohydrate determinants, which leads to the de novo expression of antigens in cancer tissue. The second process is more commonly found in early stages of cancer and results of a deficiency on the normal synthesis of complex glycans that are usually expressed in normal epithelial cells, which leads to the generation of truncated structures in cancer tissues (Pinho and Reis 2015; Julien *et al.* 2006; Kannagi *et al.* 2008).

The most common alterations in glycosylation are fucosylation, sialylation, truncation of *O*-glycans and branching of *O*- and *N*-linked glycans. Truncation of *O*-glycans is commonly found in secreted and transmembrane glycoproteins. Sialylated structures of Thomsen-Friedenreich antigens are examples of truncated glycans (Marcos *et al.* 2011; Kudelka *et al.* 2015). The increased expression of sialylated glycans promotes cell detachment from the original tumor site,

by disrupting cell-cell adhesion processes, leading to metastasis, which is related with poor prognosis for the patients (Pinho and Reis 2015).

3.1 Thomsen–Friedenreich antigens

Thomsen–Friedenreich antigens are *O*-glycans found mainly on serine- and threonine-rich mucins, thus being present in membrane glycoproteins. These antigens are a result of a defective elongation of the *O*-glycan on the first steps of mucin glycosylation (Yu 2007). The first Thomsen–Friedenreich antigen described was called T (or TF) antigen, forms the core 1 structure of mucin *O*-glycans and consists of the disaccharide composed by a galactose β1-3 linked to a *N*-acetylgalactosamine, α-linked to a serine or threonine residue (Gal β1-3GalNAcα1-Ser/Thr). The T antigen is the precursor of core 2 *O*-glycans, but if the cancer cells lose the ability to synthesize the core 2, this antigen can be exposed (Springer 1984). The T antigen can, in normal tissues, be substituted by other carbohydrate chains or sialic acids and form more complex glycans. In cancer tissues, however, this antigen is usually unsubstituted, occurring in approximately 90% of human cancers, such as breast, bladder and prostate, thus being considered a pan-carcinoma antigen, and is also correlated with cancer progression and metastasis (Yu 2007). If, on the contrary, the ability to synthetize the core 1 is lost, its precursor, the Tn antigen, is exposed. This antigen consists of a single *N*-acetyl-galactosamine α-linked to serine or threonine residue (GalNAcα1-Ser/Thr) (Munkley 2016; Springer 1984). The Tn antigen is not usually found on secreted or cell-surface proteins in normal tissues, but is found in most carcinomas, being also a pan-carcinoma antigen (Osako *et al.* 1993; Kudelka *et al.* 2015). As with the T antigen, an increased expression of the Tn antigen is related with an enhancement of cancer invasiveness and cellular proliferation and because they are detected on early-stages of cancer development, they have potential for being studied and used as biomarkers (Itzkowitz S *et al*. 1992). Both T and Tn antigens can be further modified by, for instance, sialylation, which is how the sialyl-Tn (STn) antigen is generated (Figure 3.1).

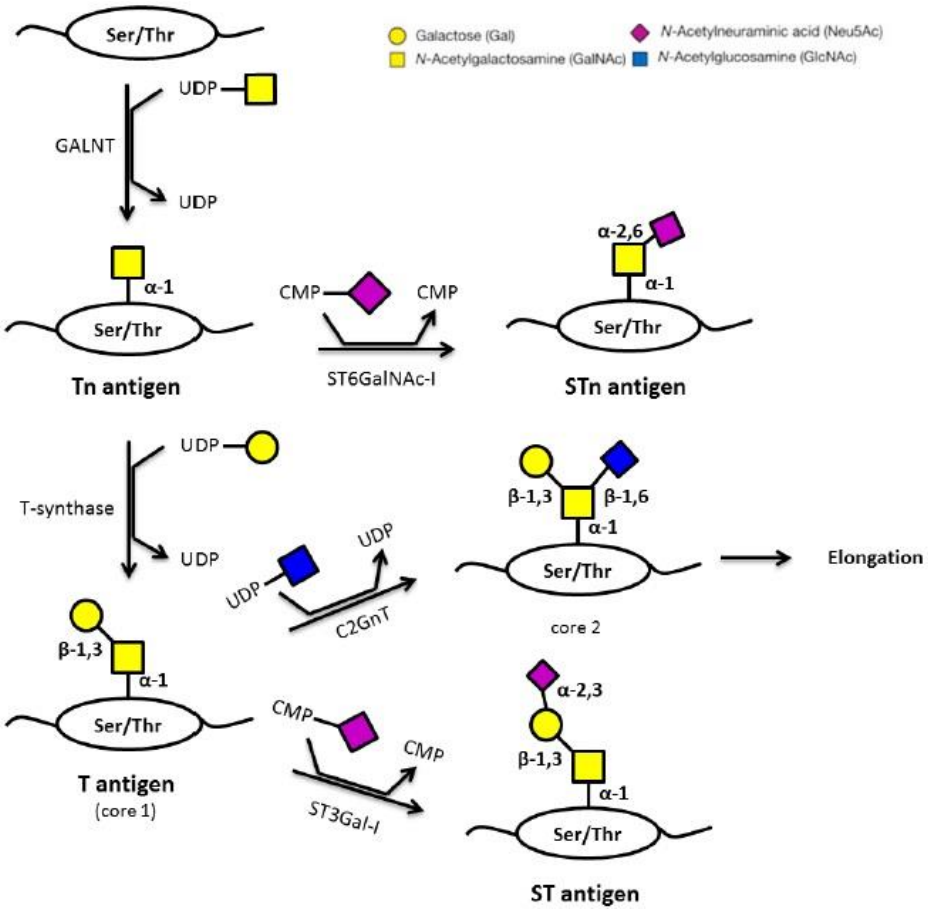

Figure 3.1. Schematic representation of the biosynthesis of Thomsen-Friedenreich antigens. Adapted from (Munkley 2016; Brockhausen and Stanley 2015; Loureiro *et al.* 2015).

3.2 Sialyl-Tn Antigen

The addition of a sialic acid residue to the carbon 6 of GalNAc (α2-6 linkage) on the Tn antigen originates the disaccharide known as sialyl-Tn (Neu5Acα2-6GalNAcα1-Ser/Thr), also referred to as CD175s (Munkley 2016; Brockhausen and Stanley 2015; Julien et al. 2012). Similarly, STn is also a pan-carcinoma antigen: is generally not expressed in normal healthy tissues but is frequently detected in most carcinomas, such as pancreatic, ovarian and lung cancers (Pinho and Reis 2015; Kudelka *et al.* 2015; Julien *et al.* 2012). Thus, the expression of this antigen is considered pathologic since it is not a normal biosynthetic precursor, as are the T and Tn antigens. In normal cells, the process of *O*-glycosylation generates elongated and branched *O*-glycans that are often modified by sialylation. However, the sialylation of the Tn antigen blocks the normal extension of the *O*-glycan chain, as the STn structure cannot be further elongated, consequently blocking the synthesis of other glycosidic structures (Munkley 2016; Schultz *et al.* 2012; Kudelka *et al.* 2015) (see Figure 3.1 in the previous section). Its overexpression results of mechanisms related to ST6GalNAc-I upregulation or the re-localization of this enzyme from the Golgi apparatus to the ER (Pinho and Reis 2015; Munkley 2016; Marcos *et al.* 2011; Ju *et al.* 2008; Ferreira *et al.* 2013; Julien *et al.* 2001).

As previously mentioned, the expression of the STn antigen is correlated with increased tumor growth and with the disruption of cell-cell adhesion mechanisms, increasing the processes of migration ad invasion and, consequently, modulating a malignant phenotype and thus being associated with a poor prognosis in cancer patients (Pinho and Reis 2015; Munkley 2016; Julien *et al.* 2006; Julien *et al.* 2012; Pinho *et al.* 2007).

Since STn is expressed early in the process of cancer development and is usually not found in healthy cells, this antigen is considered to be a helpful tumor marker in diagnosis (Pinho and Reis 2015; Kudelka *et al.* 2015; Julien *et al.* 2012). Tumor markers can be detected in serum, since it is a simple, sensitive and non-invasive method of diagnosis. However, detection of STn in serum is linked to poor prognosis, as it is related with shedding of cells from tumors into the bloodstream. This is consequently correlated with increased tumor masses found in advanced cancers, thus making the STn antigen more useful as a prognosis than as a diagnosis marker (Julien *et al.* 2012).

4. Magnetic Nanoparticles

Nanoscale magnetic materials have generated significant interest in recent years, with particular interest, magnetic nanoparticles (mNPs) with 1–100 nm have been used in biomedicine as contrast agents in magnetic resonance imaging (MRI), hyperthermia for cancer therapy, tissue repair and drug delivery (Bini *et al*. 2012; Gupta and Gupta 2005; Lim *et al.* 2013; Ruiz *et al.* 2014).

Magnetic nanoparticles can be divided in paramagnetic, ferromagnetic and superparamagnetic particles. The impact of superparamagnetic and ferromagnetic particles on MRI is similar. The composition of paramagnetic particles is different from the composition of superparamagnetic and ferromagnetic particles. Superparamagnetic and ferromagnetic particles have a magnetic core and may have a surface coating. The paramagnetic particles do not have an explicit magnetic core. Thus, their behavior on MRI is rather different from superparamagnetic and ferromagnetic particles (Rümenapp *et al*. 2012).

The mNPs are generally composed of pure metals, metal alloys or metal oxides *(*Majetich *et al.* 2013). Metallic NPs have larger magnetization compared to metal oxides, but they are not stable in air and are easily oxidized. Metal NPs may be composed of iron, cobalt, nickel and their oxides, and due to their instability are typically protected by an organic coating, forming a core-shell structure. From all iron oxide NPs, the most common biocompatible magnetic nanomaterials are pure oxides, magnetite (Fe_3O_4) and maghemite (γ-Fe_2O_3) (Gupta and Gupta 2005; Lim *et al.* 2013; Ling and Hyeon 2013; Calero *et al.* 2014; Soares *et al*. 2014).

4.1. Superparamagnetic Iron Oxide Nanoparticles

Investigations of superparamagnetic iron oxide nanoparticles (SPIONs), synthesized by several methods and functionalized for different applications, are being increasingly reported in the literature from the last decades. The simplicity of preparing nanoparticles and their stable storage in the colloidal suspensions demonstrate an increased interest of their utilization on biomedical applications (Bini *et al.* 2012; Hola *et al.* 2015). Colloidal suspensions of stabilized magnetic nanoparticles are called ferrofluids which can interact with a magnetic field (Bini *et al.* 2012; Hamley 2003). Iron oxide nanoparticles are designated by SPIONs when they are smaller than the critical size (< 15 nm) and consists of a single magnetic domain, in which all of the atomic magnetic moments are magnetized in the same direction. Single-domain particles do not have domain walls, so in the superparamagnetic (SPM) state, the entire magnetic moment of each particle is oriented in the same direction. This phenomenon is characterized by the absence of hysteresis cycles (remnant magnetization and the coercive field are null) (Goya *et al.* 2008; Hola *et al.* 2015). Another interesting property of SPIONs is their ability to generate heat when subjected to an alternating magnetic field (AMF). This thermal phenomenon may be due to energy losses during the demagnetization process (specific loss power) (Ho *et al.* 2011). Because of this magnetic property, SPIONs do not interact with each other, minimizing aggregation after the field is removed. This behavior is important for *in vivo* (drug delivery, magnetic resonance imaging and magnetic hyperthermia) and *in vitro* (bioseparation, biosensing and magnetofection) biomedical applications (Mikhaylova *et al.* 2004; Gupta and Gupta 2005; Bini *et al.* 2012).

4.1.1. Magnetic properties

The magnetic effects on magnetic nanoparticles are caused by particles with both mass and electric charges such as electrons, holes, protons, positive and negative ions. The spinning of an electric-charged particle causes a magnetic dipole – a magneton. A ferromagnetic material is composed of magnetic domains, i.e., a magnetic domain is a portion of the ferromagnetic material in which all magnetic dipoles are aligned in the same direction by the exchange forces (Akbarzadeh *et al.* 2012). Bulk ferromagnetic materials are composed of thousands of magnetic domains separated by boundaries called domain-walls, forming the so-called grains. This domain wall is a defect in the material that takes energy to form, and have significant width, generally in the tens to hundreds of nanometers. In these cases the reversal of the magnetization is controlled by the nucleation and motion of domain walls through the material (Willard *et al.* 2004). When the size of the particles is reduced, the state of lowest energy has uniform magnetization and the particle is composed of a single domain. The critical size of the single domain is affected by several factors, such as the value of the saturation magnetization (M_s), the strength of the crystal

anisotropy and exchange forces, the surface or domain-wall energy, and the shape of the particles (Akbarzadeh *et al.* 2012).

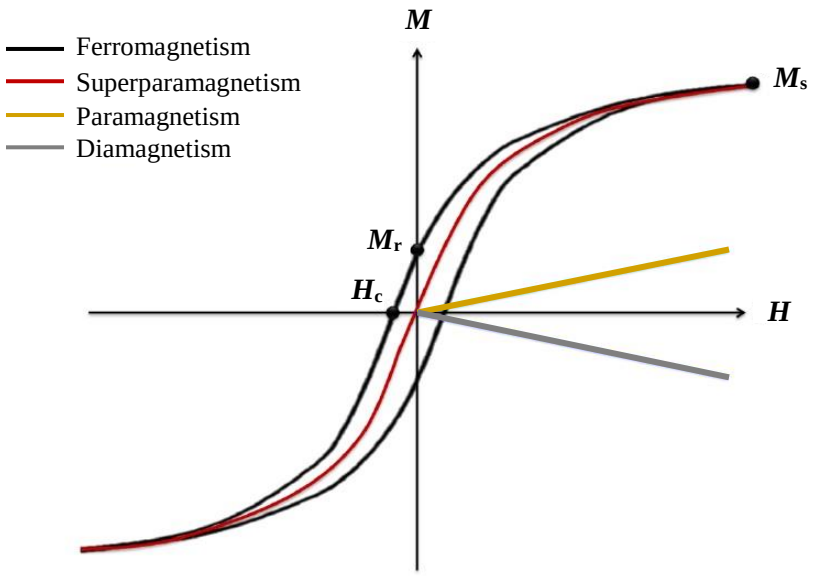

Figure 4.1. Hysteresis loops (magnetization versus applied magnetic field) for ferromagnetic, superparamagnetic, paramagnetic and diamagnetic nanoparticles. (H_c – Coercivity; M_r – Remanent magnetization; M_s– Saturation magnetization). Adpated from (Arruebo *et al.* 2007).

The properties of magnetic materials are classified according to the magnetic susceptibility (χ), which is defined by the ratio of the induced magnetization (M) to the applied magnetic field (H) (Sun *et al.* 2008; Indira 2010). This ratio is well described by a hysteresis loop (Figure 4.1), which is characterized by two main parameters: remanence (M_r) and coercivity (H_c). The remanence or remanent magnetization is the magnetization that remains after an applied field has been removed. The coercivity or coercive field is related to the 'thickness' of the curve and is the applied magnetic field required for reduction of a saturated magnetic material to zero magnetization. The coercivity has been found to be size-dependent for small particles, i.e., as the size of the particle is reduced, the coercivity increases to a maximum and then decreases toward zero (Figure 4.2) (Akbarzadeh *et al.* 2012; Willard *et al.* 2004).

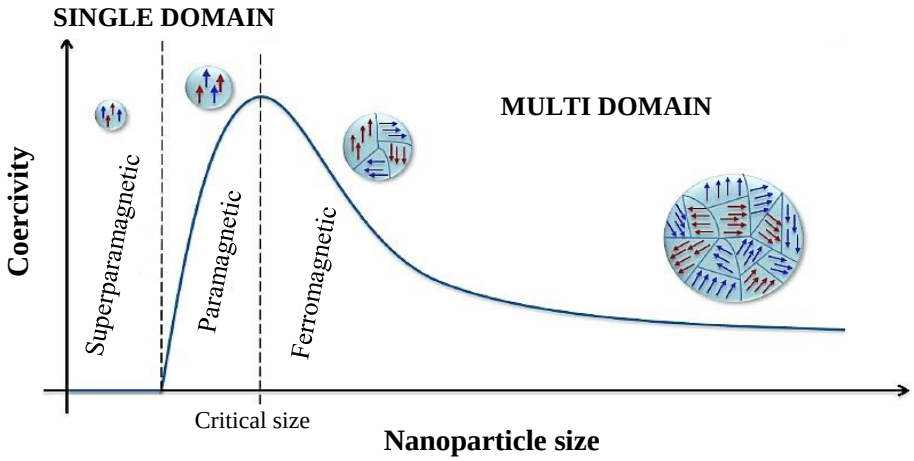

Figure 4.2. Schematic illustration of the relationship between coercivity, nanoparticles size, and magnetic domain structures. The blue and red arrows represent the magnetic dipoles. Adpated form (Akbarzadeh *et al.* 2012).

When the magnetostatic energy equalizes the domain-wall energy in magnetic nanoparticles, the single-domain phase dominates at specific dimensions. The critical diameter for a spherical Fe_3O_4 nanoparticle to possess a single-domain is believed to be 128 nm. At single domain phase, SPIONs possess one huge magnetic moment and exhibit superparamagnetism when the size of single domain particles decreases and the coercivity becomes zero. This behavior occurs above the blocking temperature (T_B) (size and shape dependent phenomena), while the thermal energy overcomes the anisotropy energy of magnetic materials. The relationships for anisotropy energy ($E(\theta)$) and superparamagnetic relaxation time (τ) (with respect to temperature) are given below:

$$E(\theta) = KV \sin^2 \theta \qquad \text{(Eq. 1)}$$

$$\tau = \tau_0 \exp\left(\frac{KV}{k_B T}\right) \qquad \text{(Eq. 2)}$$

where K is the magnetic anisotropy constant, V is the particle volume, θ is the angle between an easy axis and a magnetization vector, k_B is Boltzmann's constant and T is the temperature. τ_0 is in the range of 10^{-13}–10^{-9} s. Usually, in a colloidal solution, the magnetic moments of suspended SPIONs align themselves along the easy axis during the absence of magnetic field. However, the magnetic moments tend to align themselves in a direction parallel to the applied field, when magnetic field is applied, thereby resulting in high magnetization values. But, once the field is removed, the moments of SPIONs revert back to their original easy axis positions due to longitudinal and transverse relaxivities of SPIONs (Kandasamy and Maity 2015). The lack of remanent magnetization after removal of an applied external field enables the mNPs to maintain their colloidal stability and avoid agglomeration (Ahmed and Douek 2013).

4.2. Synthesis of Iron Oxide Nanoparticles

The synthesis methods can influence the NPs properties, such as size, dispersion of the particle-size and morphology. There are several options to synthetize NPs including chemical co-precipitation, microemulsion method, sol-gel synthesis, hydrothermal reaction, hydrolysis and thermolysis of precursors (Wu *et al.* 2008; Farhat Hadj and Joubert 1986; da Costa *et al.* 1994; Lopez Perez *et al.* 1997; Wu *et al.* 2015).

Chemical co-precipitation method is a widely used technique for synthesizing black and/or brownish SPIONs (Kandasamy and Maity 2015). The method is extremely flexible when it comes to the modulation of the core and surface properties by controlling the experimental parameters such as the reaction temperature, pH value and ionic strength of the media. Furthermore it is extremely repeatable if the experimental parameters are fixed and their synthetization in water becomes an advantage for biomedical applications (Wu *et al.* 2015).

Co-precipitation of ferric and ferrous ions in solution using a strong base leads to the formation of magnetite or maghemite (nucleation phase), depending up on the iron concentration, pH and the ratio of ferrous and ferric ions (Gnanaprakash, Mahadevan, *et al.* 2007).

4.3. Surface Modifications of SPIONs

The surface of SPIONs can be modified through the creation of atomic layers of some organic or inorganic molecules, which allows further functionalization by binding various bioactive molecules. However, more than functionalization, the major contribution of surface modifications is the colloidal stability from the SPIONs coating (Gupta and Gupta 2005).

Despite the fact that naked NPs are stable in high- and low- pH suspensions, but not in neutral pH, they must be coated for several reasons: increase the stability and protect SPIONs against aggregation, to protect the magnetic core against oxidation, to provide a reactive surface to allow their functionalization, to protect NPs against reticuloendothelial system (RES) uptake and elimination in order to enhance the blood circulation time and internalization efficiency and, finally, to avoid the generation of reactive oxygen species (ROS) upon exposure of cells to the SPIONs, preventing citotoxicity effects (Tartaj *et al.* 2011; Ling and Hyeon 2013; Ruiz *et al.* 2014; Laurent *et al*. 2008; Talelli *et al.* 2009).

The organic/inorganic surfactants/capping agents form a protective layer around SPIONs by attaching to the surface atoms of these NPs via the end functional groups either through electrostatic interactions or covalent bonding. The thickness of the protective layer can be in the range of 1–5 nm, if small organic molecules are used as surfactants/capping agents. This protective layer thickness can increase to more than 100 nm, if large polymers are used. The surfactants/capping agents usually have different end functional groups such as –OH, –COOH,

$–PO(OH)_2$, $–S(=O)_2–OH$, catechols, etc. which bring stoichiometric modifications on the surface of SPIONs (Yuen *et al.* 2012; Kandasamy and Maity 2015).

According to previous works, oleic acid (OA), a mono-unsaturated fatty acid commonly used as a surfactant to modify the surface of magnetite nanoparticles due to the high affinity to its surface is used to obtain highly stable iron oxide nanoparticles. Stabilization occurs due to the formation of strong chemical bonds between the carboxylic acid and the SPIONs. Although oleic acid is only soluble in non-polar solvents, bilayer oleic acid-coated magnetite nanoparticles can be dispersed in polar liquids with the proper adjustment of pH. Though several works have been reported with oleic acid as a surfactant for magnetite nanoparticles (Kbari *et al.* 2015; Talelli *et al.* 2009; Wormuth 2001; Portet *et al.* 2001), only few authors have reported the presence of an oleic acid bilayer that turns the iron oxide NPs soluble in aqueous solvents (Yang *et al.* 2010; Liu *et al.* 2006; Mahdavi *et al.* 2013). Maity and Agrawal have prepared iron oxide NPs coated with either a mono-layer or a bilayer of oleic acid and found that they are either stable in kerosene and dodecane or water, respectively (Maity and Agrawal 2007). This is important as for their biomedical use in magnetic resonance imaging (MRI) as contrast agents and for magnetic hyperthermia as treatment agents (Soares *et al.* 2016).

From all different polymers/molecules which can be used for coating NPs, meso-2,3-dimercaptosuccinic acid (DMSA) presents a great potential for target-drug delivery. This molecule binds to the nanoparticle through the carboxylate groups which establishes a negative surface charge of the particle and the thiol groups generates a “cage” of disulfide-cross-linked DMSA around the nanoparticle (Zhang *et al.* 2016).

Coated SPIONs with DMSA have been tested *in vitro* and *in vivo*, in particular their cell interaction process, pharmacokinetics and biodistribution in animal models with the main objective of drug delivery, nuclear magnetic resonance (NMR) imaging and magnetic hyperthermia (Ruiz *et al.* 2014). In further studies it was observed that the coating of SPIONs with DMSA enhanced endocytosis by various cell types and shows that this coating molecule improved cellular uptake efficiency significantly (Wilhelm *et al.* 2003; Billotey *et al.* 2003). Furthermore, was reported that the DMSA-coated SPIONs produced relatively weak cytotoxic and no genotoxic effects, compared to uncoated NPs (Zhang *et al.* 2015).

4.4. Biomedical Applications of SPIONs

Typically, superparamagnetic iron oxide nanoparticle conjugates are comprised of a magnetite core providing inherent contrast for MRI and a biocompatible coating that provides ample functional groups for conjugation of additional tumor targeting and therapeutic moieties like monoclonal antibodies (mAbs) commonly used for cancer treatment (some examples of these mAbs are shown in Table 10.1 in Appendix II). As some formulations of magnetite-based NPs

have already gained approval for use in humans as iron deficiency therapeutics and as MRI contrast agents by the Food and Drug Administration (FDA) (e.g. Feraheme®, Feridex I.V.®, and Gastromark®), extension of these NP configurations for uses beyond MRI contrast enhancers such as cancer therapeutics via drug delivery, biotherapeutic transport, magnetic hyperthermia, photothermal ablation, and photodynamic therapy (PDT) may be fast-tracked as compared to NP formulations lacking widespread acceptance of nontoxicity (e.g. other metal-core NPs) (Krishnan 2010).

Contrast agents are used to enhance the image obtained from magnetic resonance. Some images obtained using a common contrast agent by magnetic resonance of soft tissues have a relatively high quality, although there are some cases where it is difficult to acquire sufficient image of contrast to diagnose the pathology of interest. In this case, SPIONs can be used to overcome this difficult. Actually, paramagnetic substances, such as gadolinium (Gd^{3+}), have enhanced the magnetic resonance signal but the toxicity associated with them has led to a new focus of research in SPIONs (Li *et al.* 2013; Hola *et al.* 2015).

In contrast of gadolinium (T_1 agent), the superparamagnetic iron oxide nanoparticles are T_2 agents which alter the transverse (T_2) relaxation times of water protons, leading to signal attenuation on a T_2 or T_2*-weighted map. T_2 agents provide dark negative signal intensity in images and can be used to visualize cells grafted in organs that appear as high signal intensity. Compared to T_1 agents, SPIONs based T_2 agents appear to be the preferred MRI contrast agents for monitoring cells due to their high sensitivity and excellent biocompatibility (Yang *et al*. 2009; Li *et al*. 2013). For breast cancer, for instance, the goal of molecular imaging is to be able to accurately diagnose when the tumor diameter less is 0.3 mm (approximately 1000 cells), as opposed to the current techniques like mammography, which require more than a million cells for accurate clinical diagnosis (Majetich *et al.* 2013).

Beyond the SPIONs core use as MRI contrast, several drug delivery systems with coated SPIONs have been evaluated. Properties like NPs shape, size and surface charge must take in consideration to develop a successful drug delivery system. Some studies refer that rod-shaped and non-spherical nanoparticles showed a longer blood circulation time, when compared with spherical particles (Rümenapp *et al.* 2012; Ruiz *et al.* 2014; Wahajuddin and Arora 2012).

Moreover, the size of the NPs determines their half-life in circulation. For instance, particles smaller than 10 nm are mainly removed by renal clearance, instead particles larger than 200 nm become concentrated in the spleen or can be taken up by phagocytic cells of the body leading to a decreased their plasma concentrations. However, NPs with 10–100 nm are considered to have an optimum size, with longer circulation times because they can easily escape the reticuloendothelial system in the body (Wahajuddin and Arora 2012; Arruebo *et al*. 2007).

The NPs surface charge can provide some colloidal stability and determine their distribution in the body, thus affecting the NPs internalization in their target cells (Wahajuddin and Arora 2012).

More recently, a new strategy has been tried: formulations of theranostic systems, through the combination of diagnostic and therapeutic entities into one drug delivery vehicle. This idea highlights the considerable capacity of iron oxide NPs have for use in highly personalized medicine (Ryu *et al.* 2014; Ruiz *et al.* 2014), as researchers develop a library of synthesis protocols and discrete nanoscale modules with specific roles for cancer theranostics, individualized NP formulations exhibiting a full-suite of treatment and diagnostic capabilities may be created in an efficient and effective manner. An exemplary NP incorporating a multitude of diagnostic and therapeutic features is depicted in Figure 4.3 (Revia and Zhang 2016).

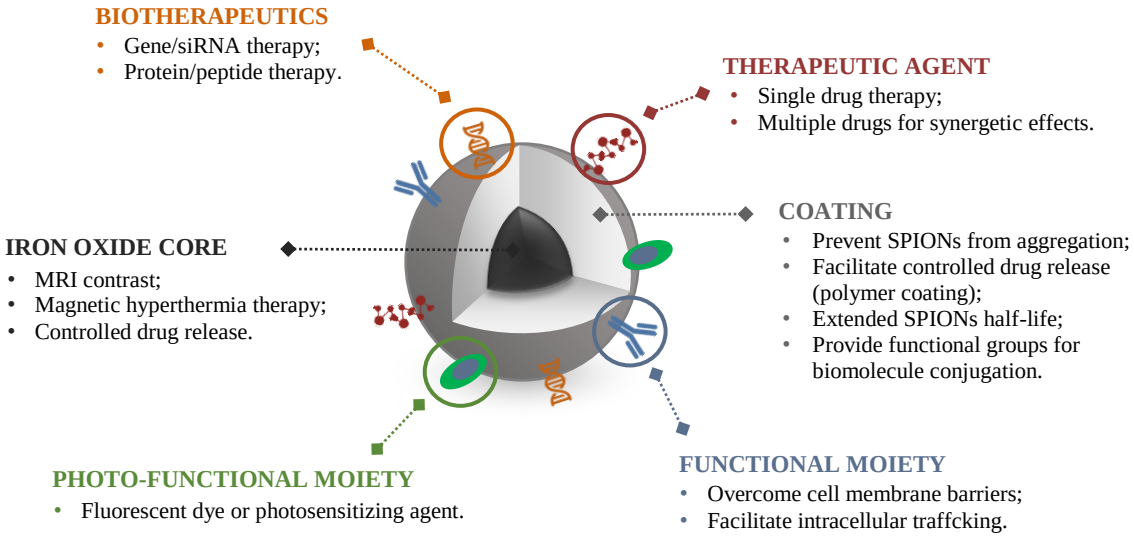

Figure 4.3. Schematic illustration of a full-suite theranostic NP. The magnetite core serves as an MRI contrast agent and heat source for magnetic hyperthermia, and a polymer coating increases biocompatibility, mitigates RES uptake, and allows for facile functionalization with chemotherapeutic, biotherapeutic, optical enhancement, and targeting moieties. Adapated from (Revia and Zhang 2016).

4.4.1. Magnetic Hyperthermia in Cancer Therapy

The preferential killing of cancer cells without damaging normal cells has been a desired goal in cancer therapy for many years. However, the various procedures used to date, including chemotherapy, radiotherapy, or surgery, can fall short of this aim. The potential of hyperthermia as a treatment of cancer was first predicted following observations that several types of cancer cells were more sensitive to temperatures in excess of 41.8ºC than their normal counterparts (Jordan *et al.* 1996; Horsman and Overgaard 2007).

In the past, external means of heat delivery were used such as tubes with hot water ultrasonic, microwave, radiofrequency, infrared radiation and magnetically excitable thermoseeds

techniques, but more recently research has focused on the injection of magnetic fluids directly into the tumor body, or into an artery supplying the tumor (Johannsen *et al.* 2005). The method relies on the theory that after localization of magnetic nanoparticles near the cancer site using magnetic targeting, an AMF is applied for a period of time to induce heat of about 42-45ºC for initiating apoptosis in cancer cells, where this heat can be controlled by manipulating the size, shape, crystallinity, corresponding magnetic properties of NPs and the applied AMF. Specific absorption rate (SAR) is a parameter to qualitatively and quantitatively measure the efficiency of mNPs which take part in converting AMF into heat based on Brownian and Néel relaxations of individual mNPs, basically SAR indicates the heat evolution rate in hyperthermia (Kandasamy and Maity 2015). Apart from the particle size and shape influencing their magnetic properties, thus consequently their heating power, there is also a dependency between temperature elevation and magnetic field amplitude which must be considered when comparing experiments with different tissue parameters. On the basis of recent studies, tumors with volumes of approximately 300 mm^3 can be heated and no potential problems were expected with larger tissue volumes (e.g. > 1000 mm^3) if there is proper regulation of the magnetic mass used and the intra tumoral particle distribution (Hilger *et al.* 2001). The frequency should be greater than that sufficient to cause any neuromuscular response, and less than that capable of causing any detrimental heating of healthy tissue, ideally in the range of 100–1000 kHz (Babincová, Leszczynska, *et al.* 2000). If suitable frequencies and field strength combinations are used, no interaction is observed between the human body and the field.

The amount of current is proportional to the size of the magnetic field and the size of the object. As these currents flow within the metal, it resists the flow of current and thereby heats, a process termed “inductive heating”. In the case of a ferromagnetic particle, it can generate heat by loss of hysteresis, while a superparamagnetic particle generates heat by relaxation of the magnetic moment. Therefore, when a magnetic fluid is exposed to alternating magnetic field, the particles become powerful heat sources, destroying the tumor cells (Babincová, Sourivong, *et al.* 2000). In that way, the magnetic fluids used are preferably suspensions of SPIONs, prepared much as described for MRI contrast agents, as these produce more heat per unit mass than larger particles (Attaluri *et al.* 2015). The level heating is simply controlled by the materials Curie temperature (42ºC-60ºC), that is, the temperature above which materials lose their magnetic properties and thus their ability to heat (Liebert *et al.* 2002).

The first investigations of the application of iron oxides for hyperthermia date back to 1957 when Gilchrist *et al.* (Gilchrist *et al.* 1957) healed various tissue samples with 20-100 nm size particles of γ-Fe_2O_3 exposed to a 1.2 MHz magnetic field. Later in 1979, Gordon *et al.* (Gordon *et al.* 1979) first proposed the concept of inducing intracellular hyperthermia using dextran-coated magnetic NPs.

The benefit of using SPIONs for cancer therapy by magnetic hyperthermia lies in the fact that, while most of hyperthermia devices are restricted in their utility because of unacceptable coincidental heating of healthy tissue, SPIONs hyperthermia is appealing because it offers a way to ensure only the intended target tissue is heated (Majetich *et al.* 2013).

Part II

Aims of the Study

Cancer is a severe disease and currently is one of the leading causes of morbidity and mortality in the world, affecting one third of the inhabitants of developed countries during their lifetime and killing one out four of them.

Currently, cancer research is considered an increasingly logical science with great potential for the development of new treatment options. Advances in nanomedicine have resulted in rapid development of nanomaterials with considerable potential in cancer diagnostics and treatment. More recently the concept of intracellular hyperthermia emerged wherein magnetic nanoparticles are concentrated at the tumor site and remotely heated using an applied magnetic field to achieve hyperthermic temperatures (42-45ºC). In this master thesis, a therapy system for cancer was propose, composed by a magnetic core, an organic surface coating and contributing with the presence of a specific targeting agent, in this case a monoclonal antibody which provides high specificity to the proposed system.

Several human carcinomas, such as breast cancer express the cell-surface carbohydrate antigen sialyl-Tn (STn) which is not observed in normal healthy tissues. This antigen is expressed in the early stage of breast cancer and so is considered an excellent candidate to target initial phases of malignancy. For these reasons, one purpose of this thesis project was the development of a complex antibody-conjugated magnetic nanoparticles. This specific antibody which will be conjugated with magnetic nanoparticles' surface is a highly specific monoclonal antibody against sialyl Tn (STn) and will confer specificity to the whole system due its action in the specific target cells.

Therefore, the main goal of this project was the development and detailed characterization of superparamagnetic iron oxide nanoparticles in order to proceed to its internalization in breast cancer cell lines for later *in vitro* magnetic hyperthermia assays.

The work was divided in five main aims:

1. Synthesis and characterization of superparamagnetic iron oxide nanoparticles (SPIONs);
2. Surface modification to obtain stable SPIONs and to provide the chemistry for bio-conjugation;
3. Functionalization of SPIONs with a monoclonal antibody against sialyl Tn (STn);
4. SPIONs cytotoxicity assessment in two breast cancer cell lines; and
5. Qualitative and quantitative evaluation of SPIONs internalization in the two breast cancer cell lines in order to understand their action as heat generators for magnetic hyperthermia *in vitro*.

Part III

Materials and Methods

5. Superparamagnetic Iron Oxide Nanoparticles

5.1. Synthesis of Superparamagnetic Iron Oxide Nanoparticles (SPIONs)

Iron oxide nanoparticles were synthesized by chemical co-precipitation using an adapted method from *Soares et al.*(Soares *et al.* 2014). Ferrous and ferric chlorides $FeCl_3.6H_2O$ and $FeCl_2.4H_2O$ (*Alfa aesar* and *Sigma-Aldrich*, respectively) were dissolved in 10 mL and 2.5 mL of deionized water (dH_2O), respectively, to obtain 1 and 2 M solutions. 50 mL of dH_2O was added to the iron mixture in order to achieve a molar ratio of 1:2 (Fe^{2+}:Fe^{3+}). The final solution was deaerated with bubbling N_2. Further, 10 mL of NH_4OH 25% (*Panreac*) was rapidly added under vigorous stirring during 5 minutes. The reaction was stopped adding 60 mL of dH_2O, the superparamagnetic iron nanoparticles (SPIONs) precipitate was left to settle by magnet attraction, and the top water layer was discarded. The magnetic nanoparticles were washed two to five times with dH_2O. A part of the suspension was freeze-dried (Vaco 2, Zirbus) in order to obtain dry nanoparticles for further characterization.

5.1.1. Spectrophotometric Determination of Iron by UV-Vis

Iron content in iron oxide nanoparticles was determined using the 1,10-phenantroline colorimetric method (Talelli *et al.* 2009; Soares *et al.* 2014). Briefly, 40 µL of diluted SPIONs suspension were placed into an eppendorf tube, followed by addition of 20 µL of HCl 37% (v/v) (*Panreac*) and incubation for 1 hour at room temperature to dissolve all the SPIONs and obtain ferrous and ferric chloride. Afterwards, in order to reduce Fe (III) to Fe (II), 100 µL of hydroxylamine hydrochloride (*Sigma-Aldrich*) solution 100 $mg.mL^{-1}$ (previously prepared in 0.01 N HCl) was added, followed by 500 µL of 1,10-phenantroline monohydrate (*Sigma-Aldrich*) solution 3 $mg.mL^{-1}$ (previously prepared in 0.01 N HCl) to form the orange-red complex of tris(1,10-phenanthroline) iron (II). Lastly, the samples were diluted to 1800 µL by adding ammonium acetate (*Panreac*) 500 mM pH 4 buffer (previously prepared in 0.01 N HCl). All the samples were made in triplicates and the absorbance was measured at 510 nm using a UV-Vis spectrophotometer (T90+ UV/VIS Spectrometer PG Instruments Ltd). The concentration of iron (II) was calculated by a calibration curve obtained using Mohr's salt solution in HCl 0.01 N in a concentration range of 10 to 1000 $\mu g.mL^{-1}$.

In order to obtain the nanoparticles concentration, the formula [Fe] = 0.7 x [NPs] was used. The ratio was obtained from control experiments.

5.2. Surface modification of SPIONs

5.2.1. Stabilization of SPIONs with Oleic Acid

Nanoparticles obtained from chemical co-precipitation technique resulted in instable colloidal suspensions in water due to the positive charge they have. NPs tend to aggregate and sediment in aqueous solutions translating a problem in their utilization on biomedical applications. One of the most effective way to stabilize these nanoparticles is by using surfactants (surface active agents) that promote charge neutralization to the NPs surface and guarantee their stabilization in an aqueous suspension (Soares *et al.* 2014; Soares *et al.* 2015). In this work one stabilizing agent was studied: oleic acid (OA).

The chemical structure of oleic acid (Figure 5.1) makes it a very good and common used surfactant for SPIONs since the oleic acid chain possesses a terminal carboxylic acid that confers high affinity to magnetite nanoparticles surface (Yang *et al.* 2010).

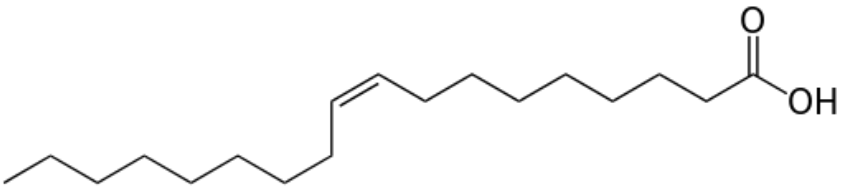

Figure 5.1. Chemical structure of oleic acid.

For stabilization of SPIONs a known concentration of oleic acid (*Panreac*), 64 mM, was added to an appropriate volume of the magnetic suspension. Taking into account the SPIONs weight, a 64% factor was applied to that value and generated the oleic acid quantity to use in order to perform the stabilization. The mixture was allowed to react for different times (1 to 5 hours) in the ultrasound bath. After the reaction, the stabilized SPIONs were subjected to dialysis in a 4 RC Dialysis Membrane Tubing 12 to 14 kDa MWCO (Spectrum™ Spectra/Por™). This procedure was done to allow the release of oleic acid that was not reacted with the magnetic nanoparticles. The dialysis water changes were done with dH_2O until the pH of the final suspension was 7.

5.2.2. Iron oxide nanoparticles oxidation and surface modification with DMSA

Dimercaptosuccinic acid (DMSA), represented in Figure 5.2, was selected as an important coating since it allows high stability of the nanoparticles in aqueous media and has free ligand groups for further biomolecule conjugation (Mejias *et al.* 2010). For this work the surface modification with DMSA was adapted from Fauconnier *et al.* and Xie *et al.* (Fauconnier *et al.* 1997; Xie *et al.* 2011). In order to achieve the production of stable NPs with sizes smaller than

200 nm an oxidation step was produced conferring them a greater stabilization in aqueous solutions.

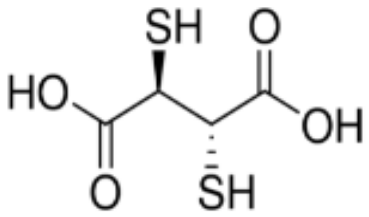

Figure 5.2. Chemical structure of dimercaptosuccinic acid (DMSA).

Before coating the NPs with DMSA, the pH of the suspension was adjusted to pH 3 with nitric acid 65% (*Merck*) under magnetic agitation to oxidize the nanoparticles.

After SPIONs oxidation, DMSA (*Sigma-Aldrich*) was added immediately at a 3 – 4 ratio of [DMSA]/[Fe^{2+}] (Fauconnier *et al.* 1997). DMSA was dissolved in 2 mL of dH_2O and the pH adjusted to 5.5 with 0.1 M NaOH (*CARLO ERBA Reagents)* solution under vigorous stirring (Massart 1980; Fauconnier *et al.* 1997). The reaction of DMSA with SPIONs was performed in the ultrasound bath during different times (1 to 5 hours). After the reaction, the stabilized NPs were subjected to dialysis in a 4 RC Dialysis Membrane Tubing 12 to 14 kDa MWCO (Spectrum™ Spectra/Por™). This procedure was done to allow the release of DMSA that was not reacted with the magnetic nanoparticles. The dialysis water changes were done with dH_2O until the pH of the final suspension was 7.

5.3. Iron oxide nanoparticles functionalization

Two molecules, EDC (1-ethyl-3-(3-dimethylaminopropyl) carbodiimide hydrochloride) and NHS (N-hydroxysuccinimide) were used to allow cross-linking to a biomolecule (i.e. an antibody in this case). The use of both molecules improves the efficiency of the reaction and the creation of a dry-stable (amine-reactive) intermediate. EDC couples NHS to carboxyl (from DMSA), forming an NHS ester that is considerably more stable than using EDC alone, while allowing for efficient conjugation to primary amines at physiologic pH (Sperling and Parak 2010; Jahan and Haddadi 2015).

20 mg of DMSA Fe_3O_4 NPs were incubated with 50 mg of EDC (*Sigma-Aldrich*) and 50 mg of NHS (*Alfa aesar*) previously dissolved in 500 mM sodium acetate (*Scharlau*), during 20 min under mechanical stirring. The activated SPIONs were washed 3 times with dH_2O and separated using a magnet between each wash.

Then, 15 mL of supernatants collected from hybridoma cell cultures (from two different clones – 2A5 and 2A6), which contain a considerable anti-STn antibody titre, were added to the 20 mg

of activated NPs and incubated during 18 hours at room temperature under mechanical stirring. The resulting reaction was washed 5 times with PBS and separated using a magnet between each wash. The functionalized NPs are designated mNPs-2A5 and mNPs-2A6. The mAb were produced by the Glycoimmunoly Group using the hybridoma technology (Loureiro *et al.* 2015).

Hybridoma technology were processed by mice immunization with seven antigens, all containing STn: ovine submaxillary mucin (OSM), a STn-rich natural mucin; membrane extracts of the STn^+ variant of MDA-MB-231, MCF-7 and MCR cell lines; cell lysates of the STn^+ variant of MDA-MB-231 and MCR cell lines; and a mixture of cell lysates of both MDA-MB-231 STn and MCR STn cell lines.

5.4. Characterization of SPIONs

Iron oxide nanoparticles (naked, OA and DMSA coated, and DMSA functionalized) were characterized using different techniques. These techniques provide information about SPIONs size, hydrodynamic size, morphology and composition.

5.4.1. X-ray Diffraction (XDR)

X-ray diffraction (XDR) is an analytical technique used for phase identification of a crystalline material and can provide information about the unit cell dimension. The sample is illuminated with X-rays of a fixed wavelength and the characteristics X-ray diffraction pattern provides a "fingerprint" of the crystals present in the sample. The diffractogram (intensity as a function of the diffraction angles) is compared with a standard reference patterns. This fingerprints allow the identification of the crystalline form (Swanson 1972; Waseda *et al.* 2011).

Samples were previously freeze-dried for 24 hours and the X-ray diffraction analysis was done in a X'Pert PRO MDP (PANalytical) X-ray diffractometer. The results were evaluated using X'Pert HighScore Plus and each peak was compared with a standard reference pattern. The 2θ values were taken from 15º to 80º using a Cu-Kα radiation (k = 1.54060 Å) with a step size of 0.033. The Scherrer's equation was used to measure the average crystallite size.

5.4.2. Fourier Transform Infrared (FTIR) spectroscopy

Fourier Transform Infrared Spectroscopy (FTIR) allows the determination of the composition of a solid, a liquid or a gas by absorption or emission spectrum. FTIR is a type of absorption spectroscopy in which the chemical bonds of molecules are detected by having characteristic vibration frequencies. By subjecting these bonds to infrared radiation, the vibrational energy of the molecules in a sample increases, exhaling these from their ground state to a higher energy state. The resulting spectrum represents the absorption and transmission of the molecule to be

studied. Taking into account that each material is a unique combination of atoms, FTIR spectrometry can be used in the qualitative analysis of any materials (Theophanides 2012; Stuart 2004).

Samples were previously freeze-dried for 24 hours and analyzed by FTIR Nicolet 6700 (Thermo Electron Corporation) with attenuated total reflectance (ATR). For each transmission spectrum of the sample, a background acquisition was done to rule out any contamination from other compounds. FTIR was used to evaluate the chemical composition of uncoated, OA coated, DMSA coated and functionalized Fe_3O_4 NPs.

5.4.3. Transmission Electron Microscopy

Transmission Electron Microscopy (TEM) is a powerful and essential technique for material science. The microscope has a high energy beam of electrons that cross though a thin specimen (sample) and the interaction between the electrons and the atoms is used to observe the morphology of the sample which is analyzed (Williams and Carter 2009).

Samples were prepared by dilution in dH_2O from the original stocks in order to obtain a final concentration of 0.5 $\mu g.mL^{-1}$ Fe_3O_4 NPs. A diluted solution of nanoparticles was placed in a Kevlar 25 mesh grid for analysis. TEM images were obtained in a Hitachi H-8100 II with thermionic emission LaB6.

5.4.4. Superconducting quantum Interference device (SQUID) and Vibrating sample magnetometer (VSM)

Superconducting quantum interference device (SQUID) and vibrating sample magnetometer (VSM) are powerful tools to study the magnetic properties of nanoparticles at a microscopic level (Russo *et al.* 2012; Dodrill 2012).

The direct current (DC) magnetic properties of naked and OA coated Fe_3O_4 NPs were performed using a 7T SQUID magnetometer (S700X; Cryogenic Ltd.). Isothermal magnetization curves were obtained for fields up to 5 T for a 320 K temperature.

On the other hand, the DC magnetic properties of DMSA coated Fe_3O_4 NPs were performed using a 10T VSM magnetometer (Cryogenic-Cryofree). Hysteresis curves were recorded at 320 K temperature in the magnetic field up to 2 T.

5.4.5. Dynamic light scattering (DLS)

Dynamic light scattering (DLS) is one of the standard methods for measuring particle sizes in fluids and has been established for many years. This method is based on the examination of random particle movement due to constant Brownian motion (Figure 5.3). The collision of

particles with surrounding liquid molecules results in a diffusional process with small particles moving faster than large particles. To monitor this diffusion, the sample is illuminated with a monochromatic laser beam. Depending on the position of the particles relative to each other, light scattered by the particles undergoes constructive or destructive interference (De Kanter *et al.* 2016).

The resulting intensity fluctuations of the scattered light are detected time-resolved by a photomultiplier positioned at a certain angle to the incident light. The autocorrelation decay of the measured intensity is correlated to the translational diffusion coefficient, which in turn is used to calculate the hydrodynamic diameter of the particles using the Stokes–Einstein equation (De Kanter *et al.* 2016; Malvern 2004).

All the samples analyzed by DLS were diluted in filtered (0.22 µm pore membrane syringe) dH_2O and prepared carefully to decrease external contaminants. The samples were prepared in different SPIONs final concentrations: 0.05, 0.075, 0.1, 0.15, 0.2 and 0.25 $mg.mL^{-1}$. For each type of coated nanoparticles, OA and DMSA coated NPs, the diluted suspensions were measured in triplicates using a disposable cell with a scattering angle equal to 90º and 173º, respectively. Data analysis was performed using cumulative statistics to measure hydrodynamic size and polydispersity unless stated otherwise.

The zeta potential of SPIONs was also measured with a scattering angle equal to 173º, in a graphite electrode cell. This parameter allows the study of colloidal stability by measuring nanoparticle charge when an electrical field is applied. The zeta potential of dH_2O diluted samples was measured at pH 7 and then another zeta potential values were obtained by diluting the nanoparticles in a KNO_3 (*Merck*) 0.01 M solution and then adding HNO_3 (*Sigma-Aldrich*) 0.01 M or KOH (*Sigma-Aldrich*) 0.01 M to vary pH in order to do the measure in a range of pH 2-10 and in this way determine the best SPIONs stabilization condition.

Both measures were performed using a SZ-100 nanopartica series (Horiba, Lda) with a laser of 532 nm and controlling temperatures with a Peltier system (25ºC).

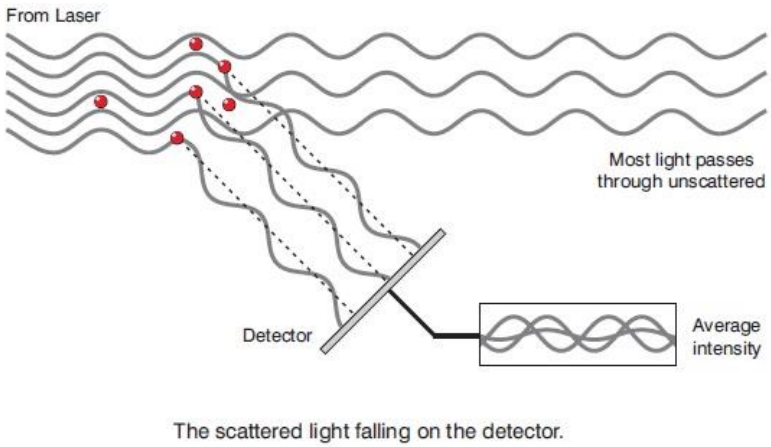

Figure 5.3. Particles are illuminated by a laser and will produced the scatter of the light in all directions. Adapted from (Malvern 2004).

6. Cell culture

6.1. Culture of breast cancer cell lines

Two cancer cell lines were used during this thesis, specifically from breast cancer. The cell lines used were of two variants - the wild type (WT) and the STn positive (STn). The breast cancer cell lines used were MDA-MB-231 WT and MDA-MB-231 STn.

The cell line MDA-MB-231 was originally established from a pleural effusion of a 51 year old woman with breast adenocarcinoma (Cailleau *et al.* 1974). This cell line was, previously, transfected with the plasmid pRc-CMV on which the complementary DNA (cDNA) of the gene that codes the enzyme ST6GalNAc-I had been inserted, generating the cell line MDA-MB-231 STn (Julien *et al.* 2001).

The cancer cell lines used are adherent and were cultured on T25 and/or T75 ventilated cap culture flasks (*Sarstedt*) and maintained in an incubator (Panasonic) at 37ºC, with a humidified atmosphere and 5% CO_2. Both MDA-MB-231 WT and MDA-MB-231 STn cells were cultivated in Dulbecco's Modified Eagle Medium (DMEM) (*Gibco*) supplemented with 10% (v/v) fetal bovine serum (FBS) (*Gibco*), Penicillin-Streptomycin (100 U/mL penicillin and 100 µg/mL Streptomycin, *Gibco/Invitrogen*), and 2 mM L-glutamine (*Gibco/Invitrogen*). The cells were detached from the culture flasks with Trypsin-EDTA (TE) (*Gibco*) when a confluence of 80-90% was observed, washed with phosphate buffered saline (PBS - solution containing 1.47 mM of KH_2PO_4, 4.29 mM of $Na_2HPO_4.7H_2O$, 137 mM of NaCl and 2.68 mM of KCl, in dH_2O water (pH=7.4)) by centrifugation (Eppendorf) at 1200x*g* for 5 minutes and subcultured according to the desired dilutions for subsequent uses. Besides being subcultured, the cell lines were also stored at -80ºC by resuspending the pellet in complete DMEM with 10% (v/v) of dimethyl sulfoxide (DMSO).

6.2. Techniques

6.2.1. Flow Cytometry

Flow cytometry is a widely used technique that allows the measurement of characteristics of a particles suspension, such as cells, in a flow system and in a short period of time. The suspension of cells flows rapidly through a beam of light, usually a laser, and ideally each cell will be analyzed individually. Several characteristics of the cell can be analyzed, such as the light scattered at different angles and the fluorescence intensity of one or more fluorophores, which can be used to identify different subsets of cells on a single suspension. The amount of scattered light that is measured is affected by the size and shape of cells, this is, by their structural complexity. This light can be scattered at larger angles, thus known as side-scatter (ssc), or at lower angles in a forward direction, thus known as forward-scatter (fsc). Therefore, the side-scatter is mostly influenced by the structural complexity, irregularities and texture of the surface or interior of the cells, while the forward-scatter is mostly influenced by their size and area, and as a result, the scattered light will provide information about the physical characteristics of the cells being analyzed. Besides, cytometers can also detect fluorescent light. Fluorescent light is a light of a long wavelength that is emitted when a molecule absorbs high energy light and then emits that energy as photons of a lower energy. This fluorescence can be either derived from natural molecules that the cells possess or via the use of fluorescent chemicals that are used to stain non-fluorescent molecules that are, in this way, undetectable in the cytometer. These chemicals absorb light of specific wavelengths and emit light of different wavelengths and for that reason the cytometer must have the appropriate filters and detectors so that they can be detected correctly, allowing the determination of the median intensity fluorescence (MFI). Sometimes these chemicals can be used to label different cell components directly, or they can be conjugated to other probes, such as antibodies, thus allowing the detection of a certain specific molecule. The MFI obtained is proportional to the amount of antibody that is binding to the cells, which is in turn proportional to the number of molecules expressed. In this way, a phenotypical analysis of the cells and functional assays can be easily performed (Ormerod 2008; Picot *et al*. 2012).

In procedures that required analysis in a flow cytometer the data was collected using an Attune Acoustic Focusing Cytometer (Applied Biosystems). This cytometer is constituted by a blue (488 nm) and a red (638 nm) lasers, which allow the use of up to six different fluorescences during the analysis. Four of them are detected by the blue laser (BL1, green; BL2, orange; BL3, red; BL4, red) and the remaining two are detected by the red laser (RL1, light red; RL2, dark red) (Corporation 2011). On all experiments, information of at least $1x10^4$ events was acquired with the use of the Attune Cytometric Software (version 2.1). The data were then analyzed with the software FlowJo (version 10).

6.2.1.1. General Flow Cytometry protocol

The desired cancer cells were detached from the culture flasks and washed with PBS by centrifugation at 1200x*g* for 5 minutes. The pellet was resuspended in 1 mL of culture medium and the cells were counted. The desired number of cells to be stained and analyzed by flow cytometry ($2x10^5$ to $3x10^5$ cells/condition) was collected into an eppendorf tube. From this point on, the cells could either be directly used for antibody staining. After collection of the desired cellular concentration, 500 µL of PBS were added and the samples were centrifuged at 1500x*g* for 2 minutes. The supernatant was discarded and the previous step was repeated. The pellets were resuspended in the desired volume of PBS, in order to then have 100 µL of cellular suspension per condition being tested. The primary antibody was added and the samples were incubated at 4ºC for 30 minutes. After the incubation, the cells were washed with 500 µL of PBS by centrifugation at 1500x*g* for 2 minutes. The supernatant was discarded and the pellets were resuspended in 100 µL of PBS. The secondary antibody (anti-mouse Ig conjugated with fluorescein isothiocyanate (FITC) (*Dako*)) was diluted 1:10 in PBS and 5 µL of this diluted antibody were added. The samples were incubated at room temperature (RT), in the dark, for 15 minutes and after the incubation time cells were washed with 500 µL of PBS by centrifugation at 1500x*g* for 2 minutes. The pellets were then resuspended in 1 mL of PBS and the cells were analyzed in the flow cytometer.

6.2.1.2. Phenotypical analysis of the expression of STn

Flow cytometry was used to evaluate the expression of STn on MDA-MB-231 cell line. This antigen was expected to be expressed in the STn variant and not on the WT variant. To do this, the flow cytometry protocol was performed as described on section 6.2.1.1. Since the goal was to detect the STn antigen and to determine the percentage of cells expressing it, an anti-STn antibody was used for this detection. Therefore, B72.3 (1.5 µL) mouse anti-STn antibody was used as primary antibody (kindly provided by collaborators). The remaining steps of the protocol were performed as described.

6.2.2. Cell exposure to OA and DMSA coated Fe_3O_4 nanoparticles

6.2.2.1. Cytotoxicity Assays

Most of cytotoxicity assays used throughout published nanoparticle studies measure cell death via colorimetric methods. These colorimetric methods can be further categorized into tests that measure plasma membrane integrity and mitochondrial activity. Mitochondrial activity can be tested using tetrazolium salts as mitochondrial dehydrogenase enzymes cleave the tetrazolium

ring. Only active mitochondria contain these enzymes; therefore, the reaction only occurs in living cells (Mosmann 1983; Lewinski *et al.* 2008).

The use of appropriate assessments is vital in evaluating the biocompatibility of SPIONs. At present, some assays are used which measure cell viability through nonspecific enzyme activity (3-(4,5-dimethylthiazol-2-yl)-2,5-diphenyltetrazolium bromide [MTT], 3-(4,5-dimethylthiazol-2-yl)-5-(3-carboxymethoxyphenyl)-2-(4-sulfophenyl)-2H-tetrazolium [MTS], CellTiter-Blue assay) or via ATP level (CellTiter-Glo assay) (Hoskins *et al.* 2012).

6.2.2.1.1. Mitochondrial impairment analysis by MTS assay

The cytotoxicity of OA and DMSA coated Fe_3O_4 NPs was examined by 3-(4,5-dimethylthiazol-2-yl)-5-(3-carboxymethoxyphenyl)-2-(4-sulfophenyl)-2H-tetrazolium (MTS) assay in MDA-MB-231 WT and MDA-MB-231 STn.

After digestion with Trypsin-EDTA (TE) (*Gibco*) and rinsing with PBS, the cells were seeded onto 96-well plates flat bottom (*Orange Scientific*) at a density of $5x10^4$ cells.mL^{-1} (200 µL per well) and incubated for 24 hours at 37ºC, with a humidified atmosphere and 5% CO_2. Next day, the medium was removed from the wells and replaced with 100 µL of fresh culture medium containing a known concentration of nanoparticles ranging from 0.05 to 4.0 mg.mL^{-1} of Fe (iron) in each well in triplicates. The medium used contained a fungicide (FUNGIZONE®) Amphotericin B (*Gibco*) solution in a 1:100 dilution and the nanoparticles samples diluted in this medium were filtered in order to prevent possible cell culture contamination because of the non-sterile NPs. To prevent an exhaustive repetition of this protocol step throughout this section, the fungicide addiction was procedure in every assay that involves the contact between NPs and the cell culture.

After a 24 hours period of incubation, with the SPIONs dilutions, at the same conditions above discriminated, the medium was discarded and the cells are washed 3-5 times with PBS until the SPIONs precipitate disappear. Fresh culture medium (100 µL) was added to each well and then proceeded with the addition of 20 µL of MTS solution (CellTiter 96® AQ_{ueous} One Solution Cell Proliferation Assay) (*Promega*). The MTS solution acted for 45 minutes and after this time, the plate was gently agitated to solubilize exiting formazan precipitates formed by the reduction of MTS in the culture medium. Then, 100 µL of supernatant was transferred to another 96-well plate to avoid a possible absorbance lecture error caused by the existing SPIONs precipitates at the bottom of the well. The plate was read on a SpectraMax 190 Microplate Reader (Molecular Devices) at an OD of 490 nm and the data were acquired using the software SoftMax Pro (version 6.4.). Control cells were treated similarly, and were incubated with the respective medium at the same dilution as the one used for incubation with nanoparticles. Cell viability was expressed as a percentage of the control, given by [% cell viability = NP treated cells/control cells x 100].

6.2.2.2. Cell exposure to SPIONs and uptake studies

Nanoparticle-cell interaction primarily depends on the nature of the NP surface. The prerequisite for improved drug delivery, improved diagnostic performance, magnetic hyperthermia and other applications of SPIONs is the efficacy of their cell uptake and internalization (Absolom *et al.* 1987; L. Harivardhan Reddy *et al.* 2012).

In this way, qualitative and quantitative studies show the SPIONs internalization behavior in terms of their accumulation and persistence inside the cells after prolonged incubations. For qualitative studies, techniques like Prussian Blue Staining indicate the visual uptake of nanoparticles (blue color) inside the cells by contrast between the red and pink colors which are produced from the nuclei and cytoplasm staining (Gu *et al*. 2011; Villanueva *et al.* 2009; Liao *et al.* 2015; Wang *et al*. 2012; Cengelli *et al.* 2009). In other hand, to study the nanoparticles subcellular localization a LysoTracker Red is used to stain the lysosomal compartment in order to conclude about their accumulation in endosome/lysosome fractions (Villanueva *et al.* 2009; Calero *et al.* 2014; Calero *et al.* 2015).

To evaluate the SPIONs internalization in a quantitative way many techniques are in use, including ultraviolet spectrophotometry (UV-Vis), magnetic particle spectroscopy (MPS), atomic adsorption spectroscopy (AAS) and inductively coupled plasma mass spectrometry (ICP-MS) (Friedrich *et al.* 2015; Liao *et al.* 2015).

Within the UV-Vis technique can be highlighted the following colorimetric methods: 1,10-phenantroline colorimetric method (Yallapu *et al.* 2010; Yallapu *et al.* 2011; Jeffery *et al.* 1989) and the colorimetric ferrozine-based method (Riemer *et al*. 2004; Fish 1988; Calero *et al.* 2015). Although the last method was the most used for iron quantification in culture cells, the first one is the simplest method and its optimization was previously done.

6.2.2.2.1. Prussian Blue Staining

The internalization of OA and DMSA coated Fe_3O_4 NPs in both cell lines was examined by Prussian Blue Staining.

After digestion with Trypsin-EDTA (TE) (*Gibco*) and rinsing with PBS, the cells were seeded onto 6-well plates (*Orange Scientific*) with 20 mm square coverslips (previously sterilized) at a density of $9x10^5$ cells.mL^{-1} (2 mL per well) and incubated for 24 hours at 37ºC, with a humidified atmosphere and 5% CO_2. Next day, the medium was removed from the wells and replaced with 2 mL of fresh culture medium containing a known concentration of nanoparticles ranging from 0.05 to 0.1 mg.mL^{-1} of Fe in each well in triplicates.

After a 24 hours period of incubation, with the SPIONs dilutions, at the same conditions above discriminated, the medium was discarded and the cells are washed 3-5 times with PBS until the SPIONs precipitate disappear. Then cells were fixed in 2% paraformaldehyde fixation buffer

(*Polysciences, Inc*.) for 40 minutes followed by PBS wash for 3 times. The wells were then treated with 2 mL of Perl's reagent (4% potassium hexacyanoferrate (II) trihydrate, $K_4[Fe(CN)_6] \cdot 3H_2O$ (w/v) (*Merck*) and 4% of HCl (v/v) (*Panreac*)) for a period of 40 minutes. After this time, the wells were rinsed 5 times with PBS and counterstained with 500 µL of nuclear fast red solution (Nuclear fast red 0.1% in 5% aluminum sulfat) (*Sigma-Aldrich*). Lastly, the wells were washed 5 times with PBS and the square coverslips, where the cells grown, were withdraw from the well, air dried and mounted in Aqua-Poly/Mount Coverslipping Medium (*Polysciences, Inc*.). The internalization of particles was analyzed using a Carl Zeiss Axio Imager D2 microscope with a 100x objective magnification and using an Olympus BX51-P polarizing microscope with a 50x objective magnification. Both of analyses were done with transmitted-light bright field and phase contrast.

6.2.2.2.2. Iron quantification in cultured cells using 1,10-phenantroline colorimetric method

After digestion with Trypsin-EDTA (TE) (*Gibco*) and rinsing with PBS, the cells were seeded onto 6-well plates (*Orange Scientific*) at a density of $9x10^5$ cells.mL^{-1} (2 mL per well) and incubated for 24 hours at 37ºC, with a humidified atmosphere and 5% CO_2. Next day, the medium was removed from the wells and replaced with 2 mL of fresh culture medium containing a known concentration of nanoparticles ranging from 0.01 to 0.5 mg.mL^{-1} of Fe in each well in triplicates.

After a 24 and 48 hours period of incubation, with the SPIONs dilutions, at the same conditions above discriminated, the medium was discarded and the cells are washed 3-5 times with PBS until the SPIONs precipitate disappear. The cells were detached from each well and placed in eppendorf tubes containing 500 µL of complete DMEM medium and washed with PBS by centrifugation at 1200x*g* for 3 minutes (this procedure was repeat 2 times). The supernatant was discarded and cell pellet obtained was rapidly lysed in 500 µL HCl 37% (v/v) (*Panreac*) and incubated for 1 hour at 55ºC. In addition to promoting the cell lysis the hydrochloric acid acts to promote the conversion of all the SPIONs and obtain ferrous and ferric chloride. Lastly, 40 µL of lysed solution were placed in a new eppendorf tube and used to start the 1,10-phenantroline colorimetric method described in 5.1.1 following the same steps as discriminated in that section without any alteration. Absorbance of all samples was measured at 510 nm using a UV-Vis spectrophotometer (T90+ UV/VIS Spectrometer PG Instruments Ltd).

Part IV

Results and Discussion

7. Iron Oxide Nanoparticles obtained from chemical precipitation

Magnetic oxides, specially magnetite (Fe_3O_4) and maghemite (γ-Fe_2O_3), have been intensively investigated because they are easy to be obtained and have properties that permit various applications, particullary in the field of biomedicine (Zhang *et al.* 2009).

The synthesis of the iron oxides using the co-precipitation method is, perhaps, the simplest chemical approach to obtain magnetic NPs. This method is commonly used since usually produces NPs with 10 nm or less. Nevertheless, there are still some difficulties, mainly related to the control of NPs size, shape and morphology. These parameters can fluctuate with iron concentration salts, pH, temperature and stirring velocity during synthesis (Kim *et al.* 2001; Gnanaprakash, Mahadevan, *et al.* 2007; Laurent *et al.* 2008; Valenzuela *et al.* 2009).

The mechanism generally accepted of the Fe_3O_4 NPs formation using ferrous and ferric salts (with a ratio of 1:2 (Fe^{2+}:Fe^{3+})) by co-precipitation method is represented by the equation below (Eq. 3) (Gupta and Gupta 2005; Faiyas *et al.* 2010):

$$Fe^{2+}(aq) + 2Fe^{3+}(aq) + 8OH^{-}(aq) \rightarrow Fe_3O_4(s) + 4H_2O(l) \qquad \text{(Eq. 3)}$$

The NPs produced in this work were precipitated using ammonia, as a base, with a final pH 8–9. Bubbling with N_2 through the solution was used to protect the critical oxidation of the magnetite at this point and also to reduce particle size.

Independently of the SPIONs application, but specifically in biomedical field, it is crucial to have a colloidal stability of NPs to avoid aggregation (Soares *et al.* 2015). For this reason, at the beginning of this work two different surface modifications were performed in order to obtain favorable chemical and physical stability of SPIONs in aqueous solution (Song *et al.* 2012; Laurent *et al.* 2008; Teja and Koh 2009). Therefore, after synthesis, the NPs solution was either stabilized with oleic acid and DMSA.

7.1. Structural characterization

X-ray diffraction (XRD) was used to confirm which species were obtained for each condition of surface modification. Magnetite and maghemite are both considered to be ferromagnetic, and to have very similar identical crystalline structures and physical properties, so their identification by XRD can be difficult (Rebodos and Vikesland 2010).

Figure 7.1 shows the XRD patterns obtained for naked Fe_3O_4 NPs (**a**), OA 64 mM coated Fe_3O_4 NPs (**b**) and DMSA 13 mM coated Fe_3O_4 NPs (**c**). For the naked SPIONs, the six characteristic 2θ peaks occurred at 30.3, 35.6, 43.3, 53.6, 57.2 and 63.1, which correspond to the diffraction planes (220), (311), (400), (422), (511) and (440), respectively (Soares *et al.* 2014). Compared to standard XRD patterns for magnetite and maghemite powders (JCPDS 00-019-0629

for magnetite and JCPDS 00-039-1346 for maghemite) the synthesized NPs have a crystalline cubic magnetite structure.

The average crystallite size was calculated for both conditions (**a**, **b** and **c**) using Scherrer's equation:

$$\tau = \frac{K\lambda}{\beta \cos\theta} \qquad \text{Eq. (4)}$$

Where τ is equivalent to the particles average core diameter; K is the grain shape factor (K = 0.94); λ is the incident X-ray wavelength; β denotes the full width at half-maximum (in radians) of the highest intensity, and θ is the corresponding diffraction angle (Soares *et al*. 2015).

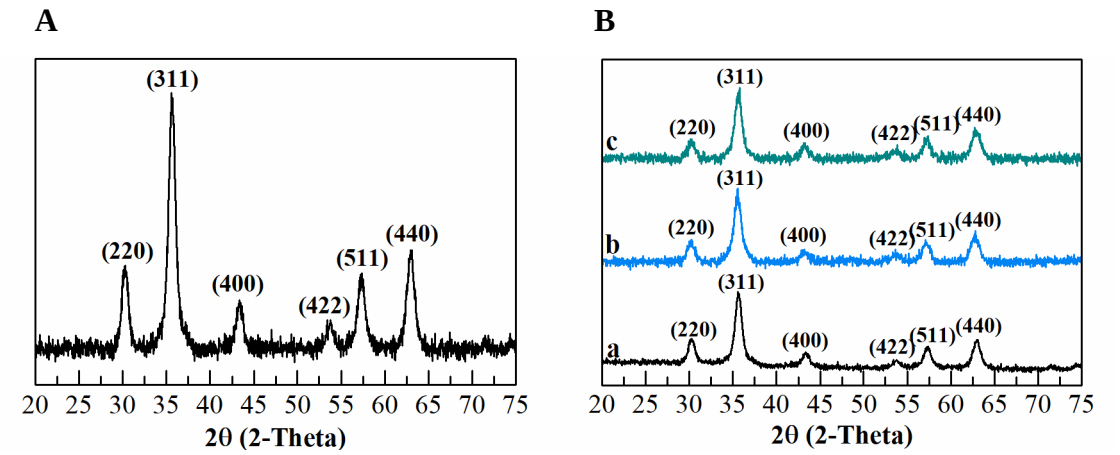

Figure 7.1. X-ray pattern of iron oxide nanoparticles produced by chemical co-precipitation. (A) Naked Fe_3O_4 NPs. **(B)** Naked Fe_3O_4 NPs (**a**) and coated NPs, oleic acid 64 mM coated Fe_3O_4 NPs (**b**), DMSA 13 mM coated Fe_3O_4 NPs (**c**).

The average crystallite size obtained from equation 4, for naked Fe_3O_4 NPs was around 9.75 nm (2θ = 35.56). The same happened with OA 64 mM coated Fe_3O_4 NPs (2θ = 35.54) and with DMSA 13 mM coated Fe_3O_4 NPs (2θ = 35.74), where both obtained a τ value around 9.75 nm. The iron oxide NPs stabilized with oleic acid and DMSA retained the crystal structure of naked NPs, as can be seen in Figure 7.1 (**b** and **c**) where naked and coated nanoparticles XRD patterns are similar, denoting that the surfactant does not change the Fe_3O_4 nanoparticles crystalline structure.

Since the percentages of magnetite and maghemite present in the analyzed samples are not known, it is not possible to discard the hypothesis of maghemite traces caused by the oxidation of SPIONs after their synthesis. However, knowing that the reaction is performed under an inert (N_2) atmosphere using degassed solutions to avoid uncontrollable oxidation of Fe^{2+} into Fe^{3+}, it can be affirmed that the NPs are mainly constituted by magnetite (Mascolo *et al*. 2013; Ali *et al*. 2016).

A higher magnetite content in iron oxide nanoparticles is important and brings advantages, namely in the use of these SPIONs in biomedical applications. Magnetite has a higher magnetic saturation than maghemite (Rebodos and Vikesland 2010), which is an important characteristic to explore their magnetic properties in magnetic hyperthermia, since the magnetic moments of this superparamagnetic nanoparticles tend to align themselves in a direction parallel to the applied field, when magnetic field is applied, thereby resulting in high magnetization values (Kandasamy and Maity 2015).

Therefore, the two surface modification conditions of SPIONs were selected for the further studies.

7.2. Surface Modification with Oleic Acid and DMSA

Nanoparticles were coated with oleic acid and dimercaptosuccinic acid (DMSA) with two main purposes: provide colloidal stability and provide the necessary chemistry for bio-conjugation.

Oleic acid is often used as a surfactant to modify the surface of magnetite particles since it has higher affinity to the surface of superfine magnetite compared to other surfactants. This affinity is due to the strong chemical bond formed between its carboxylic acid and the amorphous iron oxide nanoparticles. (Yang *et al.* 2010; Soares *et al.* 2014).

The bond between the DMSA molecule and the nanoparticle surface occurs in the same way, one of the carboxylic acid group present in this substance binds to the surface of the nanoparticle by serving as a Fe ion ligand and the other carboxylic acid moiety in its carboxylate ion form, in addition to provides hydrophilic character, has the same function as the free thiol groups in DMSA. This two different groups enable the conjugation with other biomolecules, while the –SH groups that surrounds the nanoparticle, by forming disulfide bounds, can cross-linking with neighboring DMSAs on the nanoparticle surface (Lee *et al.* 2013).

To get further insight on nanoparticles surface chemistry, samples were characterized by Fourier Transform Infrared (FTIR) spectroscopy. The couple vibrations allowed the identification of the chemical bonds between magnetite (Fe_3O_4), OA and DMSA molecules.

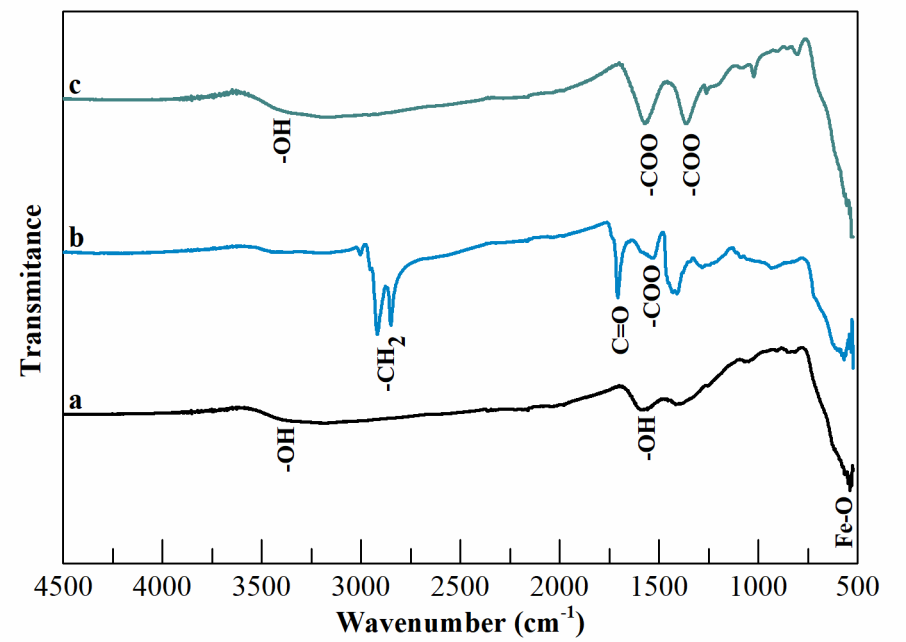

Figure 7.2. FTIR spectrum of iron oxide nanoparticles produced by chemical co-precipitation. Naked Fe_3O_4 NPs (**a**) and after surface modification with OA 64 mM (**b**) and DMSA 13 mM (**c**).

The obtained FTIR spectrum for naked Fe_3O_4 NPs is shown in Figure 7.2 (a). The strong absorbance band at 560 cm^{-1} is attributed to the Fe–O stretching vibration mode while the band at 1590 cm^{-1} is related to the O-H stretching vibration modes, and the broad band between 3000 cm^{-1} and 3500 cm^{-1} is related to the O-H stretching vibration mode due to water vapor (Soares *et al.* 2014; Gnanaprakash, Philip, *et al.* 2007).

The influence of the surface modifications in nanoparticles is shown in Figure 7.2 (b) and (c) for oleic acid and DMSA coated Fe_3O_4 NPs, respectively. It is possible to observe the presence of the above-referred bands of Fe_3O_4 in all spectra.

In OA 64 mM coated Fe_3O_4 NPs spectrum (b) it is possible to identify the following bands: bands at 2915 and 2850 cm^{-1} are attributed to the symmetric and asymmetric $–CH_2$ stretch in the oleic acid molecule, respectively. The band at 1411 cm^{-1} corresponding to the CH_3 umbrella mode of oleic acid and the bands at 1532 and 1430 cm^{-1} are respectively due to the symmetric and asymmetric $–COO^-$ stretching vibration modes which indicates that the oleic acid is bound to the surface of Fe_3O_4 nanoparticles through covalent bond between $–COO^-$ groups and Fe atom (Zhang *et al.* 2006; Aliakbari *et al.* 2015). It is worth to note that the band at 1708 cm^{-1} corresponding to the stretching vibration of C=O in oleic acid only appears when Fe_3O_4 NPs are synthesized by excess oleic acid (Yang *et al.* 2010; Soares *et al.* 2014). This characteristic band of the absorption spectrum of free oleic acid leads to the conclusion that the OA 64 mM coated Fe_3O_4 NPs represented in the above spectrum were produced with excess oleic acid (Yang *et al.* 2010; Zhang *et al.* 2006). When this happens, it is expected that the peaks corresponding to the symmetric and asymmetric $–COO^-$ stretching vibration modes tend to disappear. Since the spectrum of OA 64

mM coated Fe_3O_4 NPs shown in (b) confirm both peaks, it can be concluded that the 64 mM concentration of oleic acid which coat the NPs is the estimated concentration from which the bilayer of oleic acid is formed.

Considering that the oleic acid molecule links to the Fe_3O_4 nanoparticle surface through the carboxylic group, when oleic acid forms a monolayer, only the $–COO^-$ group appear on FTIR spectra, since none of the COOH groups are present. However, with the addition of more oleic acid, the COOH group starts to become visible in the FTIR spectra, thus justifying the formation of the bilayer. This bilayer formed by the oleic acid molecules turns the magnetite nanoparticles hydrophilic making them more stable in aqueous solutions (Soares *et al.* 2014; Yang *et al*. 2010; Tao 1993).

In the FTIR spectrum of DMSA 13 mM coated Fe_3O_4 NPs (c) the presence of DMSA at the NPs surface was identified by the characteristic asymmetric and symmetric stretching vibration modes of $–COO^-$ groups at 1570 and 1360 cm^{-1}, respectively. These peaks are shifted to lower wavenumbers compared with the carbonyl absorptions in free DMSA at around 1700 cm^{-1} (Palma *et al.* 2015; Ge *et al.* 2009; Chen *et al.* 2008).

Although some authors refer the observation of peaks corresponding to the presence of thiol groups, the spectra which represent the DMSA 13 mM coated Fe_3O_4 NPs (c) is devoid of these peaks (Palma *et al.* 2015; Galli *et al.* 2017). The main reason why this has happened is the fact that after surface modification with DMSA, the funcionalized nanoparticles were subjected to dialysis. At high DMSA surface functionalization, the free S–H groups from neighboring grafted molecules are closer together, making intraparticle S–S bridging the dominant mechanism, avoiding particle agglomeration and leading to higher colloidal stability, but when a low DMSA surface functionalization occurs, interparticle S–S bridges take place and particle agglomeration increases, leading to high values of hydrodynamic diameters (Ruiz *et al.* 2014). So, as it can be seen in Figure 7.3, chemical co-precipitation method promotes an exposure of thiol groups which helps in reaching other DMSA molecules and therefore in the particle agglomeration increase. In order to overcome this problem, the dialysis process was implemented to allow the release of DMSA that was not reacted with the nanoparticles surface and produce nanoparticles with a hydrodynamic size below to 200 nm, fitting them to one of the requirements for *in vitro* and *in vivo* biomedical applications (Villanueva *et al.* 2009).

In this way, the absence of S–H stretching vibration modes is due to the dialysis procedure which contribut for intraparticle S–S bridging.

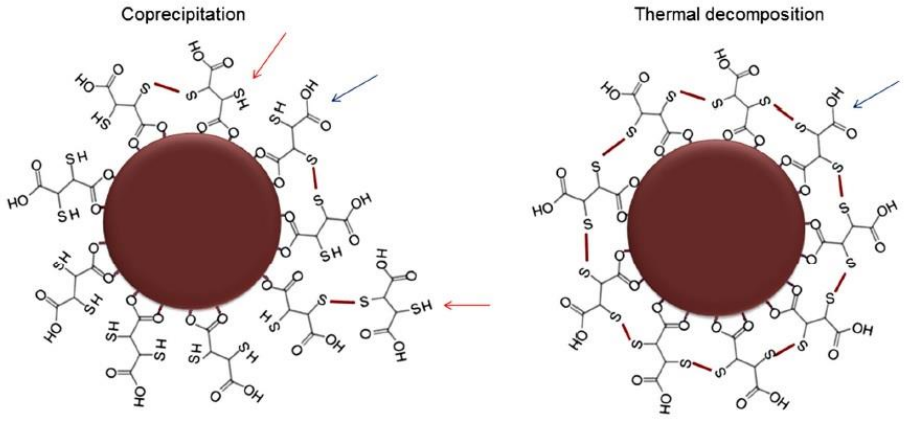

Figure 7.3. Iron oxide nanoparticles modified with dimercaptosuccinic acid. Nanoparticles obtained via co-precipitation surface-grafted with DMSA (left). Nanoparticles obtained via thermal decomposition and followed by a ligand exchange reaction with DMSA (right). (Ruiz *et al.* 2014).

7.3. Morphological characterization

Chemical co-precipitation technique is a very versatile way to synthetize iron oxide nanoparticles since it allows controlling the properties of the obtained nanoparticles by changing the synthesis parameters (Wu *et al.* 2015). OA and DMSA coated Fe_3O_4 NPs were produced to investigate the influence of the stabilizing agents in the nanoparticles size by Transmission Electron Microscopy (TEM).

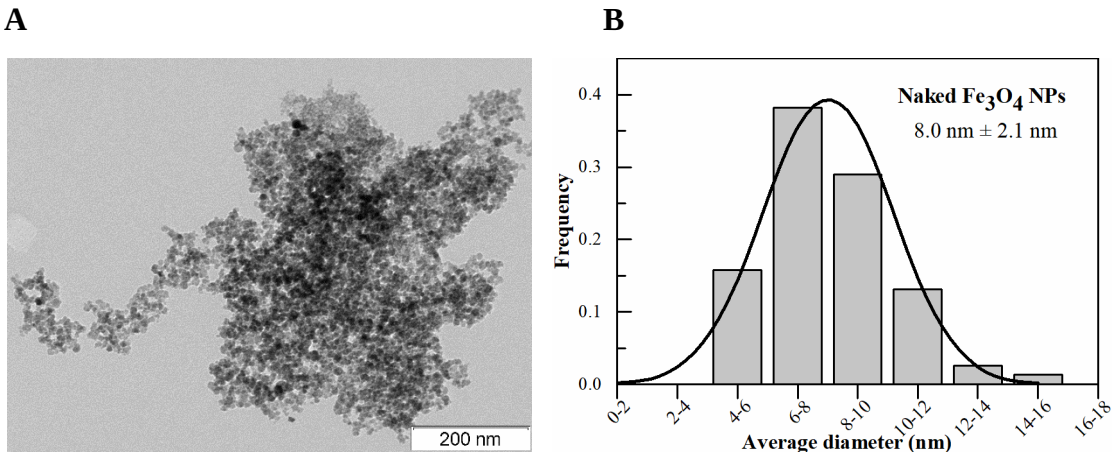

Figure 7.4. TEM image (A) and their respective size distribution graph (B) of naked iron oxide nanoparticles produced by chemical co-precipitation.

Figure 7.4 (A) shows TEM image of naked Fe_3O_4 NPs with an average diameter of 8.0 nm and a narrow size distribution. This is very interesting considering that for biomedical applications the nanoparticles must have a size below 200 nm and a narrow size distribution. In addition, for these nanoparticles to be superparamagnetic their size cannot exceed a few tens of nanometers (Laurent *et al.* 2008; Villanueva *et al.* 2009). However, the NPs show a high aggregation state,

due to the absence of stabilizers (Tartaj *et al.* 2011). In this way, the morphological characterization of surface modified nanoparticles with OA 64 mM and DMSA 13 mM was performed. For that, different times (1 to 5 hours) of reaction in ultrasound bath between the NPs and the stabilizers were performed to conclude about their influence on the nanoparticles' stabilization in aqueous solution and in their size distribution.

Figure 7.5 shows TEM images and their respective size distribution graphs of the surface modified nanoparticules. In all cases, there is a common conclusion: the used stabilizers in the tested concentrations do not change the Fe_3O_4 core size, as can be seen by the average diameter of each case. Figure 7.5 (A), (B) and (C) are relative to Fe_3O_4 NPs stabilized with oleic acid for 1, 3 and 5 hours of reaction time, respectively. Even with 1 hour (A) of reaction, the aggregation state of the NPs seems to decrease when compared with the naked Fe_3O_4 NPs, i.e., the samples seem to have smaller aggregates. By increasing the reaction time (B and C), it is observed that the clusters size decrease and isolated nanoparticles are visible. Considering that the nanoparticles produced for the *in vitro* cell assays described in section 9 must have a narrow size distribution and be as isolated as possible, the reaction time chosen for subsequent OA 64 mM coated Fe_3O_4 NPs synthesis was 3-4 hours.

Figure 7.5 (D), (E) and (F) are relative to Fe_3O_4 NPs stabilized with DMSA for 1, 3 and 5 hours of reaction time, respectively. In this case, for all the reaction times, DMSA coating seems to provide stabilization to the NPs in solution leading to a decrease in the tendency for clustering. For this reason, and to keep the same conditions to produce the surface modified nanoparticles, the reaction time chosen for subsequent DMSA 13 mM coated Fe_3O_4 NPs synthesis was 3-4 hours.

Lastly, it should be noted that the semispherical shape observed in all TEM images of Figures 7.4 and 7.5 might be due to the type of salts that were used to produce the NPs or to the molar ratio of Fe^{2+} and Fe^{3+} (Gupta and Gupta 2005).

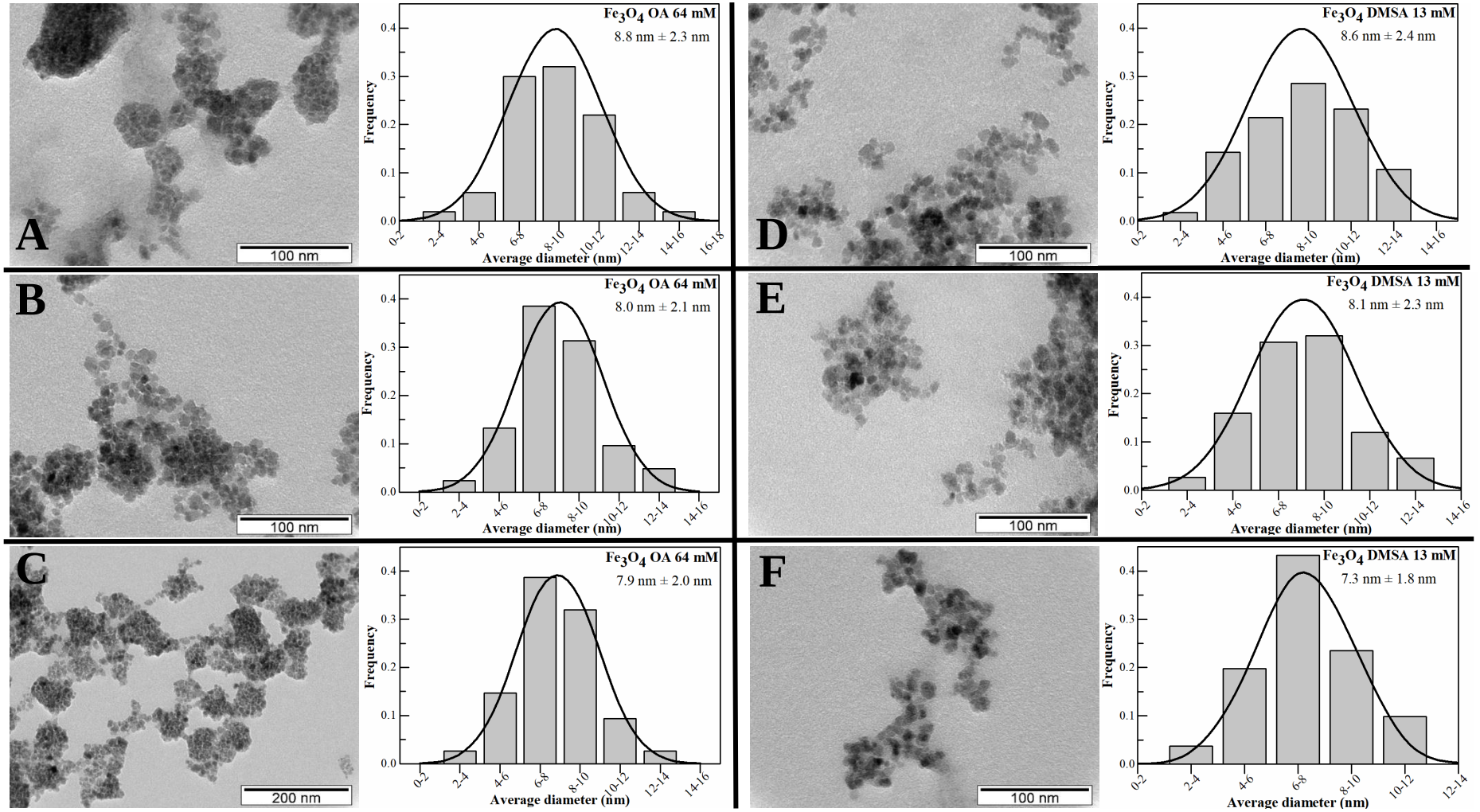

Figure 7.5. TEM images and their respective size distribution graph of iron oxide nanoparticles produced by chemical co-precipitation and surface modified with OA 64 mM and DMSA 13 mM. The surface modification reaction was performed in the ultrasound bath during different times (1 to 5 hours). OA 64 mM coated Fe_3O_4 NPs: (**A**) – 1 hour reaction; (**B**) – 3 hours reaction; (**C**) – 5 hours reaction. DMSA 13 mM coated Fe_3O_4 NPs: (**D**) – 1 hour reaction; (**E**) – 3 hours reaction; (**F**) – 5 hours reaction.

7.4. Magnetic characterization

The influence of stabilizers in the magnetic properties of Fe_3O_4 NPs was evaluated by magnetometry, using a superconducting quantum interference device for Naked and OA 64 mM coated Fe_3O_4 NPs and a vibrating sample magnetometer for DMSA 13 mM coated Fe_3O_4 NPs. The magnetization, represented as emu per gram of the whole particle (including magnetic and non-magnetic material), was evaluated in samples with and without stabilizers as it can be seen by the hysteresis loops measured at a temperature of 320 K for the both nanoparticles in Figure 7.6.

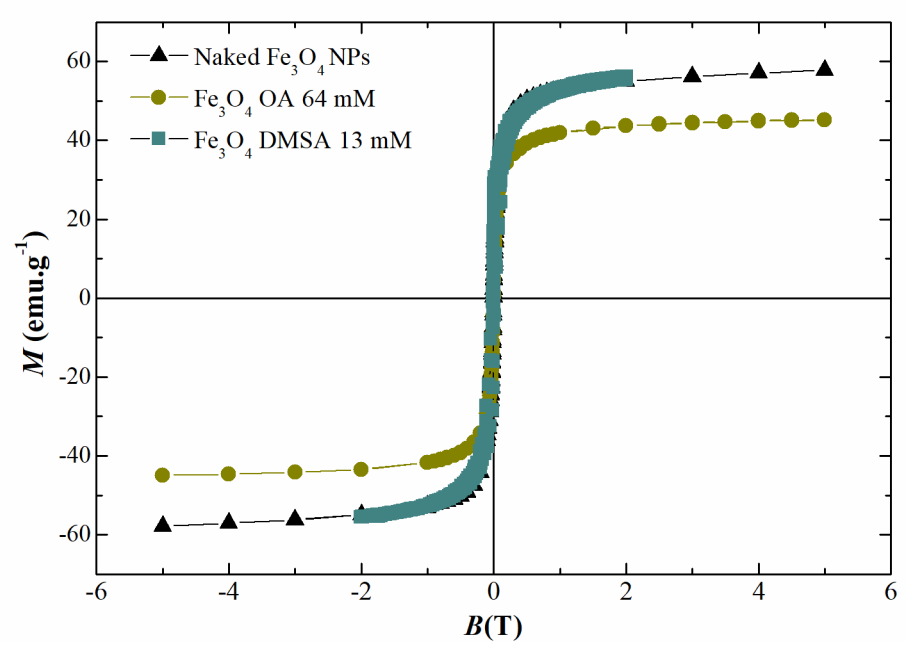

Figure 7.6. Magnetic characterization of naked (black triangles), OA 64 mM coated Fe_3O_4 (green circles) and DMSA 13 mM coated Fe_3O_4 NPs (blue squares).

Figure 7.6 shows the influence of oleic acid and DMSA on the Fe_3O_4 NPs for a concentration of 64 mM and 13 mM, respectively. The influence of DMSA in the magnetic properties of nanoparticles is not significant, since the saturation magnetization does not seem to change when comparing magnetization curves of naked and DMSA coated NPs. For these nanoparticles the magnetization value (M_s) is about to 57 emu.g^{-1}. However, it is apparent that the coating with oleic acid slightly alters the magnetic properties of NPs since the saturation magnetization value decreases to 45 emu.g^{-1}. This suggests that for a 64 mM concentration the surfactant is reducing the magnetic moments at the surface of the nanoparticles probably due to the diamagnetic contribution of the surfactant volume (Kim *et al.* 2001).

The results confirm that naked Fe_3O_4 NPs have a superparamagnetic behavior above the blocking temperature, given by the absence of coercivity and remanence at 320 K. Moreover, for the coated nanoparticles, the superparamagnetic behavior is not affected, since at 320 K the absence of coercivity and remanence remains. In all cases, the magnetic domains are not separate

by domain walls (multi-domain state). Instead, each particle represents a single magnetic domain (Liu *et al.* 2006).

Both oleic acid and DMSA were very effective in stabilizing the iron oxide nanoparticles. Their negative nature promotes the ideal environment for the stabilization of the iron oxide nanoparticles whose surface is usually positively charged (Yang *et al.* 2010; Gass *et al*. 2006; Hong *et al.* 2009). Further, coating of NPs is possible with any of these stabilizers since it allows obtaining a high number of small NPs stabilized in the suspensions. Furthermore, the tested coatings do not significantly change the physicochemical and magnetic properties of the NPs except for a 64 mM concentration of oleic acid due to the formation of a bilayer.

7.5. Zeta Potencial and DLS

The charge or electrostatic potential – zeta potential − at the surface of the nanoparticle has a significant importance in the colloidal stability of the system and can be considered an indicator of the nanoparticles stability due to the electrostatic interaction (Mahmoudi *et al.* 2011). Iron oxide nanoparticles with zeta potencial values higher than +25 mV and values lower than -25 mV usually are stable, otherwise they will have a propensity to aggregate due to Van Der Wall interparticle attraction (Mahmoudi *et al.* 2011). Therefore, *in vitro* and *in vivo* stability of magnetic particles are only possible if these effects are compensated by the (i) electrostatic repulsion between adequately charged surfaces; (ii) hydrophilic particle-particle interactions; and (iii) existence of an adequate shell (steric barrier) onto the particle surface (L. Harivardhan Reddy *et al.* 2012; López-López *et al.* 2008; Hunter *et al.* 2001).

In this way, the effect of oleic acid and DMSA on the stability of the Fe_3O_4 NPs suspended in water was evaluated by zeta potential. The samples were prepared at pH 7 since the suspension of NPs that will be used for *in vitro* cell assays must be at physiological pH. The zeta potential of these samples was measured (Table 7.1) in order to evaluate their stability as a function of the reaction time effect of the stabilizing agents.

Table 7.1. The reaction time effect in the zeta potential of the OA and DMSA coated Fe_3O_4 NPs. NPs in solution with surface modification for different reaction times, coated with OA 64 mM (**A**) and DMSA 13 mM (**B**). Mean ± SD, for 5 determinations is shown.

A

Reaction Time (h)	Zeta potential (mV)
1	-122.4 ± 2.6
2	-108.0 ± 2.1
3	-115.7 ± 1.6
4	-111.9 ± 2.6
5	-104.6 ± 2.5

B

Reaction Time (h)	Zeta potential (mV)
1	-78.3 ± 3.2
2	-83.3 ± 1.1
3	-82.0 ± 1.6
4	-84.0 ± 2.7
5	-81.5 ± 1.8

At neutral pH, the OA 64 mM (A) and DMSA 13 mM (B) Fe_3O_4 NPs have a zeta potential of around -112 mV and -82 mV, respectively. These zeta potential values are acceptable to avoid particle aggregation and therefore it is possible to conclude that the concentrations of 64 mM of oleic acid and 13 mM of DMSA used to coat the NPs are adequate to achieve a stable nanoparticles suspension at physiological pH.

The presence of carboxyl groups in oleic acid and DMSA molecules (one in OA and two in DMSA) makes them very reactive towards the iron oxide nanoparticles surface due to the strong interactions that the carboxyl groups are known to form with the iron groups at the NP surface (Lattuada and Hatton 2007; Tombácz *et al.* 2013). This observation supports the presence of negatively charged groups at the surface of OA 64 mM and DMSA 13 mM Fe_3O_4 NPs (free carboxylic acid and thiol groups).

Although NPs stabilization was verified, other parameters were evaluated. The zeta potential represents the surface charge which occurs in the presence of an aqueous solution when functional groups dissociate on surface or ions adsorb onto surfaces from the solution. Varying the pH value of the aqueous phase influences two mechanisms: functional groups dissociation and ions adsorption. In addition to the solution pH, concentration and type of salt present in the solution affect the electrical charge of the nanoparticles (Salgin *et al.* 2012; Malhotra and Coupland 2004).

In this way, the zeta potential was also measured over a large pH range from diluted OA 64 mM and DMSA 13 mM coated Fe_3O_4 NPs samples (with a surface modification reaction time of 4 hours) in a 0.01 M KNO_3 solution in order to evaluate their stability under these two implemented conditions (Figure 7.7).

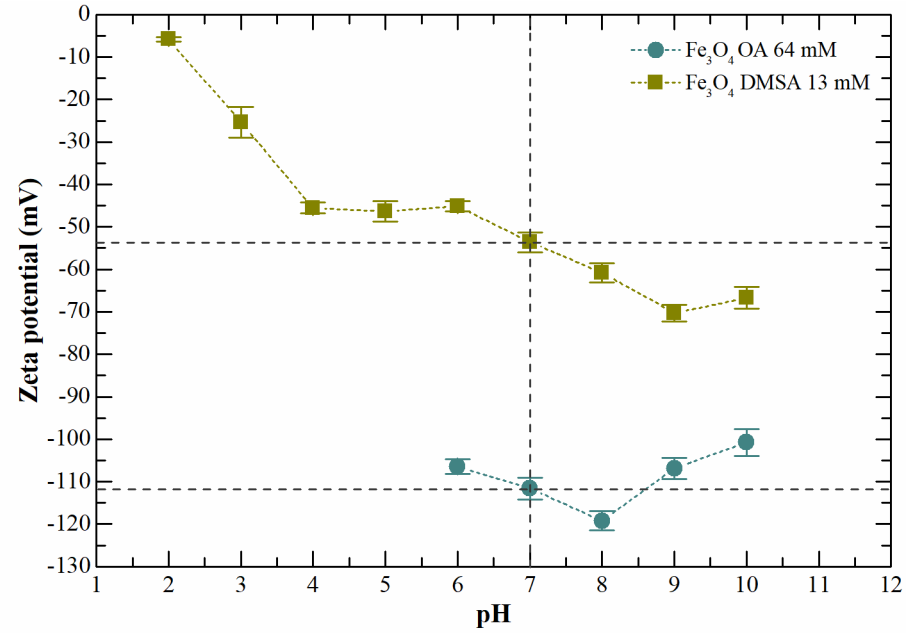

Figure 7.7. Graphical representation of zeta potential of OA and DMSA coated Fe_3O_4 NPs as a function of pH for a nanoparticles concentration of 0.15 mg.mL^{-1}. The surface modification reaction was performed for 4 hours. Mean ± SD, for 5 determinations is shown.

From the Figure 7.7 the following conclusions can be drawn: (i) at a pH range of 6 to 10, the oleic acid coated Fe_3O_4 NPs exhibit zeta potential values similar to the previously measured when the NPs were suspended in water. Particularly, for pH 7 these nanoparticles do not show any difference in their colloidal stability since the measured values were -111,9 mV (in Table 7.1 (A)) and -111.2 mV (in Figure 7.7) for NPs diluted in water and suspended in a 0.01 M KNO_3 solution, respectively; (ii) for acidic pH values was not possible to measure any zeta potential value for the OA 64 mM coated Fe_3O_4 NPs since the precipitation of these occurred momentarily when adding a 0.01 M HNO_3 solution to decrease the pH of the NPs solution. This probably occurs due to the instability of oleic acid at very low pH values; (iii) for DMSA 13 mM coated Fe_3O_4 NPs, it can be concluded that the zeta potential values vary greatly when compared with the NPs suspended in water. For pH 7 the value obtained for 4 hours of stabilization reaction time in suspensions prepared in a 0.01 M KNO_3 solution was -53.8 mV (Figure 7.7), while for the same nanoparticles suspensions diluted in water this value was much lower, -84.0 mV (Table 7.1 (B)).

It has been reported that the carboxyl (and thiol) groups of DMSA molecules not involved in the adsorption remain free at the surface of the particles and are responsible for their great negative charge, hydrophilic character and colloidal stability in aqueous phase (Huh *et al.* 2005). This indicates that the zeta potential values should have remained similar due to the net negative charge of undissociated thiols groups. This effect was not observed since a dialysis step was performed after the stabilization process of the NPs. Results similar to those presented here were obtained by other authors (Villanueva *et al.* 2009), which also carried out the use of dialysis in order to eliminate the free DMSA coating molecules that could increase the NPs hydrodynamic diameter and generate toxicity when performing *in vitro* cell assays (Lewinski *et al.* 2008).

Dynamic light scattering (DLS) measurements allow the probing of the diffusion dynamics of the NPs in a number of conditions and compare them with the zeta potential results. DLS was used to evaluate the best reaction time for the stabilizing agent binding to the NPs surface. To do this, two different studies were carried out: (i) firstly, measurements were made to determine the diluted solution concentration of NPs to be used, because there is a range of specific concentrations for which the size of the measured NPs is the lowest possible and in which the autocorrelation curves have a smooth decay pattern (Malvern 2004). Therefore, it is important to do the study of measured size *vs.* concentration; (ii) lastly, after determining the best concentration for the suspension of NPs to be used, the study of measured size *vs*. stabilization reaction time was proceeded in order to verify the reaction time required to provide better colloidal stability to the NPs. Similarly, in relation to the first study, to verify these conditions, the best hydrodynamic diameter results of NPs were considered.

Autocorrelation functions (ACF) of OA 64 mM coated Fe_3O_4 NPs and DMSA 13 mM coated Fe_3O_4 NPs are shown in Figure 7.8 (A) and (B), respectively. Autocorrelation functions of oleic acid coated NPs shows two different slight relaxation modes. A superficial slow relaxation mode

is present for NPs concentrations lower than 0.15 mg.mL^{-1} which are attributed to the presence of some NPs aggregates. On the other hand, the autocorrelation functions of DMSA coated NPs shows a typical single-exponential relaxation except for the 0.05 mg.mL^{-1} NPs concentration.

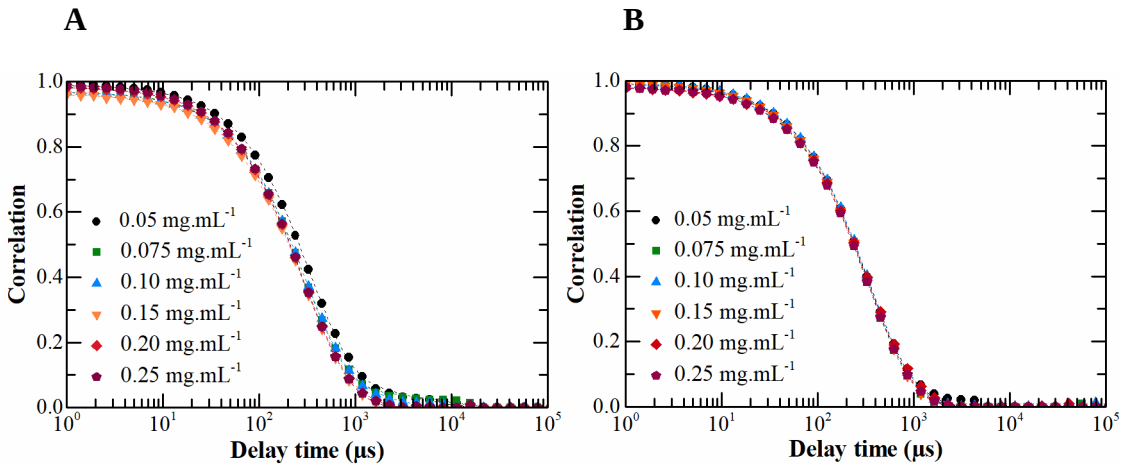

Figure 7.8. Comparison of measured (dots) and adjusted (lines) correlation curves of dynamic light scattering measurements between OA 64 mM coated Fe_3O_4 NPs (A) and DMSA 13 mM coated Fe_3O_4 NPs (B). ACF were performed for a range of NPs concentrations from 0.05 mg.mL^{-1} to 0.25 mg.mL^{-1}**.** The surface modification reaction was performed for 4 hours.

To confirm the obtained results from the autocorrelation curves the above mentioned studies of measured size *vs.* concentration and measured size *vs*. stabilization reaction time were proceeded to predict the specific suspension concentration for which the coated NPs show a higher level of stability according to the best size correlation (Figure 7.9). In order to analyze the obtained data from dynamic light scattering measurements the method of cumulants expansion was used for every measurement described above (Frisken 2001). This method is based on the expansion in Taylor series of the expression that relates the autocorrelation curve with the experimental curve, given by Equation 5:

$$C(\tau)=1+\beta\exp(-2\Gamma\tau) \qquad \text{(Eq. 5)}$$

Where τ is the delay time (µsec), C is the autocorrelation, β is a pre-exponential factor, and Γ is the decay constant, giving the average value ⟨Γ⟩. In a first order expansion: ⟨Γ⟩ = Γ and

$$\Gamma=Dq^2 \qquad \text{(Eq. 6)}$$

Being *D* the diffusion coefficient and q the scattering vector that can be determined by

$$q = \frac{4\pi n}{\lambda}\sin\frac{\theta}{2} \qquad \text{(Eq. 7)}$$

Where n is the refractive index, λ is the wavelength (532 nm) and θ is the scattering angle (90º or 173º).

Finally, the hydrodynamic diameter of the samples can be calculated using the Stokes-Einstein equation given by

$$D_h = \frac{k_B T}{3\pi\eta(T)D} \quad \text{(Eq. 8)}$$

Where k_B is the Boltzmann constant, T is the absolute temperature and η is the fluid viscosity. Under non-optimal conditions, i.e., when ACF has more than one relaxation, this type of analysis is not valid.

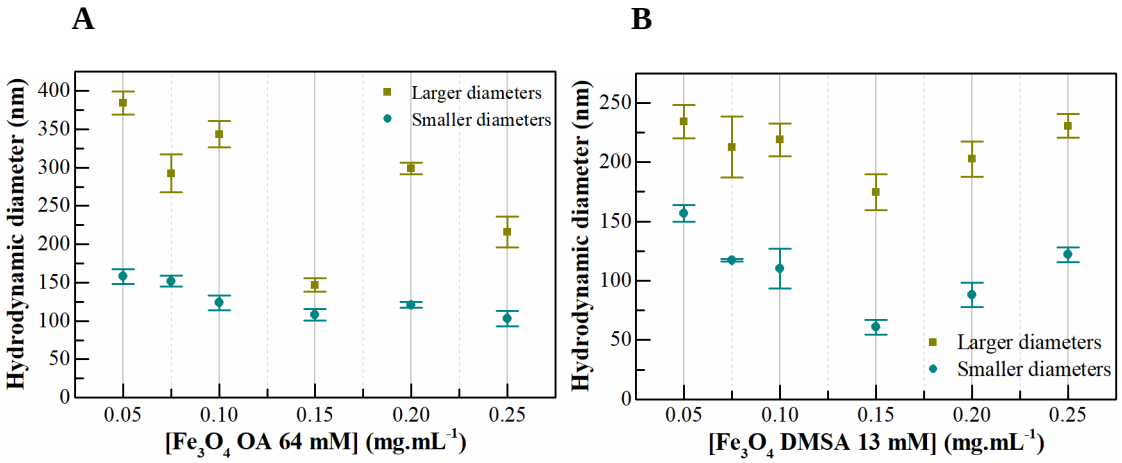

Figure 7.9. Calculated hydrodynamic diameter for OA 64 mM coated Fe_3O_4 NPs (A) and DMSA 13 mM coated Fe_3O_4 NPs (B) for the study measured size *vs.* concentration. The calculated hydrodynamic diameters were obtained using the above-described method of the cumulants expansion. The surface modification reaction was performed for 4 hours. Mean ± SD, for 5 determinations is shown.

Figure 7.9 shows the relation between the measured hydrodynamic diameters and the OA 64 mM coated Fe_3O_4 NPs (A) and DMSA 13 mM coated Fe_3O_4 NPs (B) concentration. For each case and using the method of the cumulants expansion the hydrodynamic diameters were calculated through the ACF curves. There are two calculated hydrodynamic diameters, representing the isolated NPs (smaller diameters, lower than 175 nm for both coated NPs) and the larger diameters, which represent the largest NPs aggregates.

Considering the information presented in Figure 7.9 (A) it can be conclude that for the study measured size *vs.* concentration the chosen OA 64 mM coated Fe_3O_4 NPs concentration to apply to the following measurments corresponds to a 0.15 $mg.mL^{-1}$ concentration due to the proximity of the larger and smaller hydrodynamic diameter values represented.

From Figure 7.9 (B) it can be verified that DMSA 13 mM coated Fe_3O_4 NPs does not show the same behavior as the oleic acid coated NPs and it is still apparent that the difference between values of larger and smaller hydrodynamic diameters is similar across all concentrations. These results can be corroborated by the performed autocorrelation curves of Figure 7.8 (B), where it can be verified that there are no significant differences between these curves for almost all the tested concentrations. Thus, to maintain the same conditions, the concentration of 0.15 $mg.mL^{-1}$

was chosen for the following studies. It is noteworthy that for this concentration the standard deviation values are smaller than many of the others represented for the further studied concentrations, indicating that there is a lower variability in the calculated diameters for the chosen concentration.

Lastly, the study of measured size *vs.* stabilization reaction time was carried out as can be shown in Figure 7.10. This figure shows the relation between the measured hydrodynamic diameters and the OA 64 mM coated Fe_3O_4 NPs (A) and DMSA 13 mM coated Fe_3O_4 NPs (B) stabilizing reaction time. Once the ideal concentration for the DLS technique is known, it is important to conclude about the reaction time required for the stabilization of the NPs with the respective coating molecules.

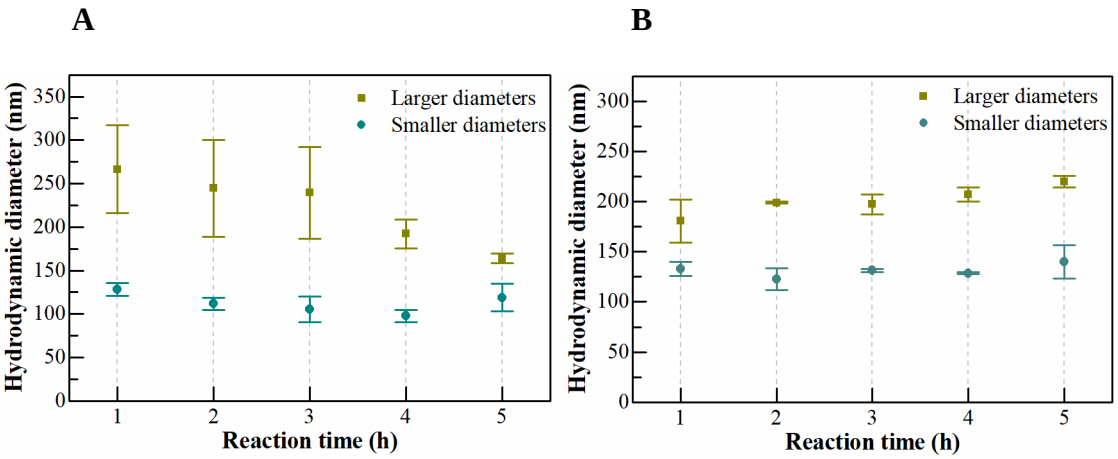

Figure 7.10. Calculated hydrodynamic diameter for OA 64 mM coated Fe_3O_4 NPs (A) and DMSA 13 mM coated Fe_3O_4 NPs (B) for the study measured size *vs.* stabilization reaction time. The calculated hydrodynamic diameters were obtained using the above-described method of the cumulants expansion. Mean ± SD, for 5 determinations is shown.

Figure 7.10 (A) shows that according to the difference between the measured hydrodynamic diameters, the best condition for the stabilization of NPs is the reaction times of 4 or 5 hours. This means that about 4 to 5 hours of ultrasound bath reaction are required for completely stabilization of nanoparticles surface in aqueous medium due the action of oleic acid as a surfactant agent (Soares *et al.* 2016).

Regarding the stabilization of the NPs with the DMSA coating, through Figure 7.10 (B) it can be concluded that as previously seen in the results of the measured size *vs.* concentration it is found that the difference between diameters is quite similar throughout the different stabilization times with DMSA. Thus, it was considered that the time required for the stabilization of NPs is about 4 to 5 hours, such as for stabilization with OA. The fact that the same conditions were maintain for the stabilization of the NPs with the two different types of coating is also due to the results obtained by TEM, in which it was verified that the chosen time for the stabilization of the nanoparticles is within this time interval.

Thus, as already mentioned in section 7.3, the stabilization of the NPs with the stabilizing agents OA and DMSA will be carried out for 4 hours in order to produce stable iron oxide nanoparticles in aqueous solution which holding the necessary conditions for their application in the posterior cellular assays.

Knowing the different conditions to produce stable nanoparticles, another parameter was evaluated: the scattering angle change in order to conclude about the true hydrodynamic diameter of NPs coated with oleic acid or DMSA.

The use of a 90° fixed angle laser consists of a classical method for detecting the brownian motions of the nanoparticles, since a movable measurement arrangement is not used and the laser focus the light beam in the center of the disposable cell, measuring only the hydrodynamic diameters of NPs passing through the fixed beam (Malvern 2004).

On the other hand, the use of a 173º movable angle is known as backscatter detection. There are several advantages to use this type of measurement: (i) because the backscatter is being measured, the incident beam does not have to travel through the entire sample. This reduces an effect known as multiple scattering, where the scattered light from one particle is itself scattered by other particles. As the light passes through a shorter path length of the sample, then higher concentrations of sample can be measured; (ii) contaminants such as dust particles within the dispersant are typically large compared to the sample size. Large particles mainly scatter in the forward direction. Therefore, by measuring the backscatter, the effect of dust is greatly reduced (Malvern 2004).

In this way, OA 64 mM coated Fe_3O_4 NPs and DMSA 13 mM coated Fe_3O_4 NPs solutions with a concentration of 0.15 $mg.mL^{-1}$ and stabilized for 4 hours were measured using the two different scattering angles in order to evaluate the autocorrelation curves behavior (Figure 7.11).

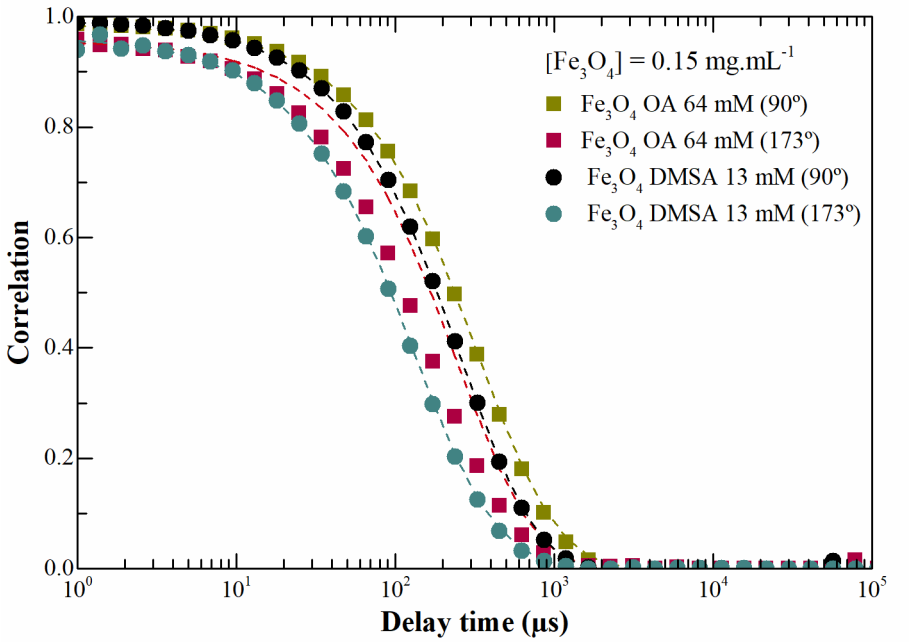

Figure 7.11. Comparison of measured (dots) and adjusted (lines) correlation curves of dynamic light scattering measurements between OA 64 mM coated Fe_3O_4 NPs and DMSA 13 mM coated Fe_3O_4 NPs with different scattering angles. ACF were performed for a 0.15 $mg.mL^{-1}$ NPs concentration and the surface modification reaction was performed for 4 hours.

If large particles are being measured, then, as they are moving slowly, the intensity of the speckle pattern will also fluctuate slowly. And simarlarly if small particles are being measured then, as they are moving quickly, the intensity of the speckle pattern will also fluctuate quickly (Malvern 2004). Figure 7.11 above shows the measurement of the autocorrelation function for different scattering angles and as can be seen, for a 173º angle the curves decay is faster than for a 90º angle. As the autocorrelation function decays faster for small particles than for large particles, it can be conclude that the DMSA 13 mM coated Fe_3O_4 NPs have a smaller real size than NPs coated with oleic acid (Lim *et al.* 2013).

This conclusion is made because for the measurement of hydrodynamic diameter of the OA coated NPs with a scattering angle of 173°, the adjusted curves do not follow the same trend as the measured points. Therefore, it can be considered that the 173° angle is not the ideal angle for determining the diameter of these NPs since they are considerably larger when compared to the DMSA coated NPs.

For this reason, the hydrodynamic diameters (D_h) shown in Table 7.2 for OA 64 mM coated Fe_3O_4 NPs and DMSA 13 mM coated Fe_3O_4 NPs were calculated according to the use of the autocorrelation curves measured at a scattering angle of 90° and at 173°, respectively.

Table 7.2. Characterization of OA 64 mM coated Fe_3O_4 NPs and DMSA 13 mM coated Fe_3O_4 NPs by DLS. A scattering angle of 90º and 173º was used to measure the D_h of oleic acid and DMSA coated NPs, respectively. [a]D_h, hydrodynamic diameter; [b]PDI, polydispersity index. Mean ± SD for 5 determinations is shown.

Stabilized NPs	D_h[a] (nm)	PDI[b]
OA 64 mM coated Fe_3O_4 NPs	147.3 ± 5.5	0.25 ± 0.02
DMSA 13 mM coated Fe_3O_4 NPs	57.1 ± 1.7	0.20 ± 0.01

A difference between the size of NPs obtained by TEM and the D_h is observed. In TEM image, the oleic acid and DMSA coating are not visible; therefore, the measured diameters correspond to the single core of the NP. When the NPs are in suspension with these stabilizer agents, the hydrodynamic diameter was measured with DLS, which incorporates also the oleic acid bilayer and the linked DMSA molecules at nanoparticles surface (Lim *et al.* 2013).

7.6. DMSA coated nanoparticles functionalization

Several human carcinomas, such as breast cancer express the cell-surface carbohydrate antigen sialyl-Tn (STn) which is not observed in normal healthy tissues. This antigen is expressed in the early stage of breast cancer and so is considered an excellent candidate to target initial phases of malignancy. Moreover, STn expression is associated with tumor invasiveness and metastasis, and recently was revealed that STn-expressing cancer cells are prone to cause immune tolerance (Loureiro *et al.* 2015; Miles *et al.* 1994). For these reasons, one purpose of this thesis was the development of a complex antibody-conjugated magnetic nanoparticles which confers specificity to the whole system due its action in the specific target cells.

Iron oxide nanoparticles coated with DMSA were functionalized with a a highly specific monoclonal antibody against sialyl Tn (STn) developed by Glycoimmunology Group using hybridoma technology described by Loureiro *et al.* (Loureiro *et al.* 2015), in order to produce the above mentioned complex. Only the DMSA coated NPs were used to performe this study since the OA coated nanoparticles do not have any further COOH disposable group to react with the EDC molecules since the only carboxylic acid group that this stabilizer agent contains is already linked to nanoparticles surface.

The coupling reaction is mediated by two molecules: EDC (1-ethyl-3-(3-dimethylaminopropyl) carbodiimide hydrocloride) and Sulfo-NHS (N-hydroxysulfosuccinimide) (Fig. 7.12). Nanoparticles have carboxylate groups on their surface created by DMSA. In the first step, EDC reacts with these carboxylate groups and creates an active-ester leaving group (*O*-acylisourea). Sulfo-NHS added in a second step, increasing the solubility and stability of the active intermediate, and promoting a better conjugation with antibodies, because the sulfo-NHS

ester is more reactive with the amine groups present at their surface (*N*-terminal and lysine side-chain) (Scientific; Hermanson 2013).

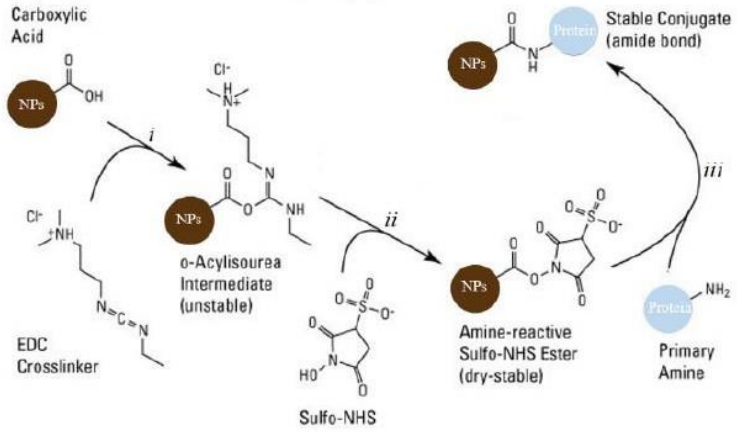

Figure 7.12. Functionalization reaction with EDC and Sulfo-NHS crosslinkers. The reaction occurs in three steps: (*i)* addition of EDC to nanoparticles to form an unstable *O*-acylisourea intermediate; (*ii)* addition of sulfo-NHS forms a stable amine-reactive ester; and (*iii*) reaction of the of the reactive sulfo-NHS ester with a primary amine of a protein. Adapted from (Scientific).

The nanoparticles functionalization was evaluated by FTIR spectrometry in order to verify the presence of the mAb at their surface. From Figure 7.13 (b and c) it can be observed that the absorption bands from 1160 to 1070 and around 950 to 862 cm^{-1} are due the stretching and bending vibration of C−O and -NH_2, respectively. This characteristics bands are due to the mAb conjugation at nanoparticles surface by the functionalization reaction with EDC and Sulfo-NHS crosslinkers (Zhang *et al*. 2009). It is possible to conclude that the conjugation process with the specific monoclonal antibody from the two different clones (b, 2A5 and c, 2A6) was successful.

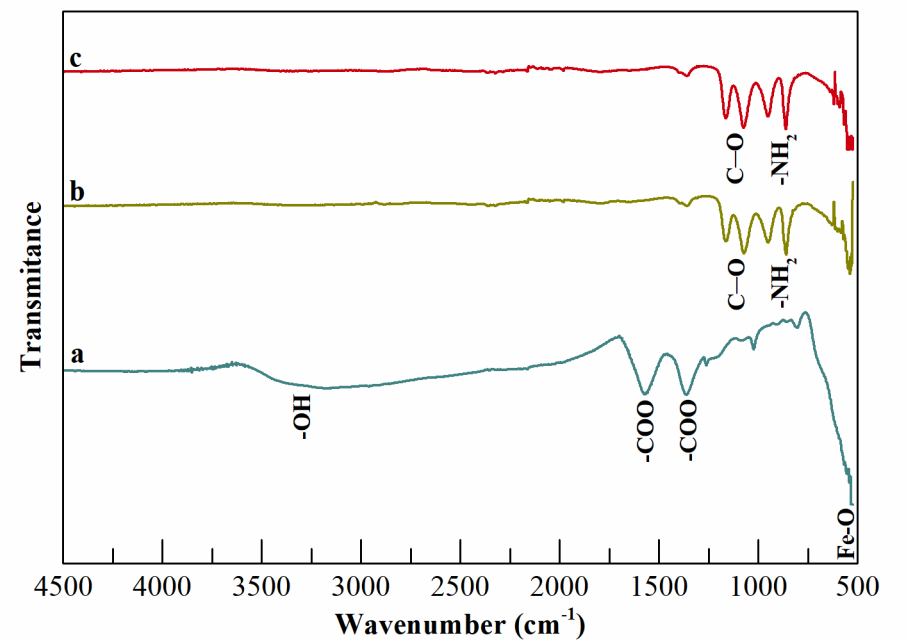

Figure 7.13. FTIR spectrum of iron oxide nanoparticles conjugated with a specific monoclonal antibody against sialyl Tn (STn). DMSA 13 mM coated NPs (**a**) and after functionalization with the mAb from 2A5 clone (**b**) and with the mAb from 2A6 clone (**c**).

It should be emphasized that the absence of the amide band peak around 1655 cm^{-1} is due to the presence of sulfo-NHS ester which is more reactive with the amine groups of the antibody, making it impossible to visualize this band in the FTIR spectrum, since the primary amine became unavailable for any molecular linkage. However, the remaining amine groups constituting the mAb are both present and may be visible in the above spectra (b and c).

8. Identification of STn presence in MDA-MB-231 STn cell line

8.1. Phenotypical characterization of MDA-MB-231 STn by flow cytometry

To perform the procedures needed for the following cell viability and internalization studies, two breast cancer cell lines were initially cultured, as it was previously mentioned in section 6.1 of Part III. A phenotypical characterization was performed by flow cytometry. In this characterization, the focus was mostly on evaluation of the expression of STn, the antigen of interest, in MDA-MB-231 STn cell line. To guarantee that the cells maintained the phenotype of interest, this is, that the expression of STn was maintained, this procedure was performed often.

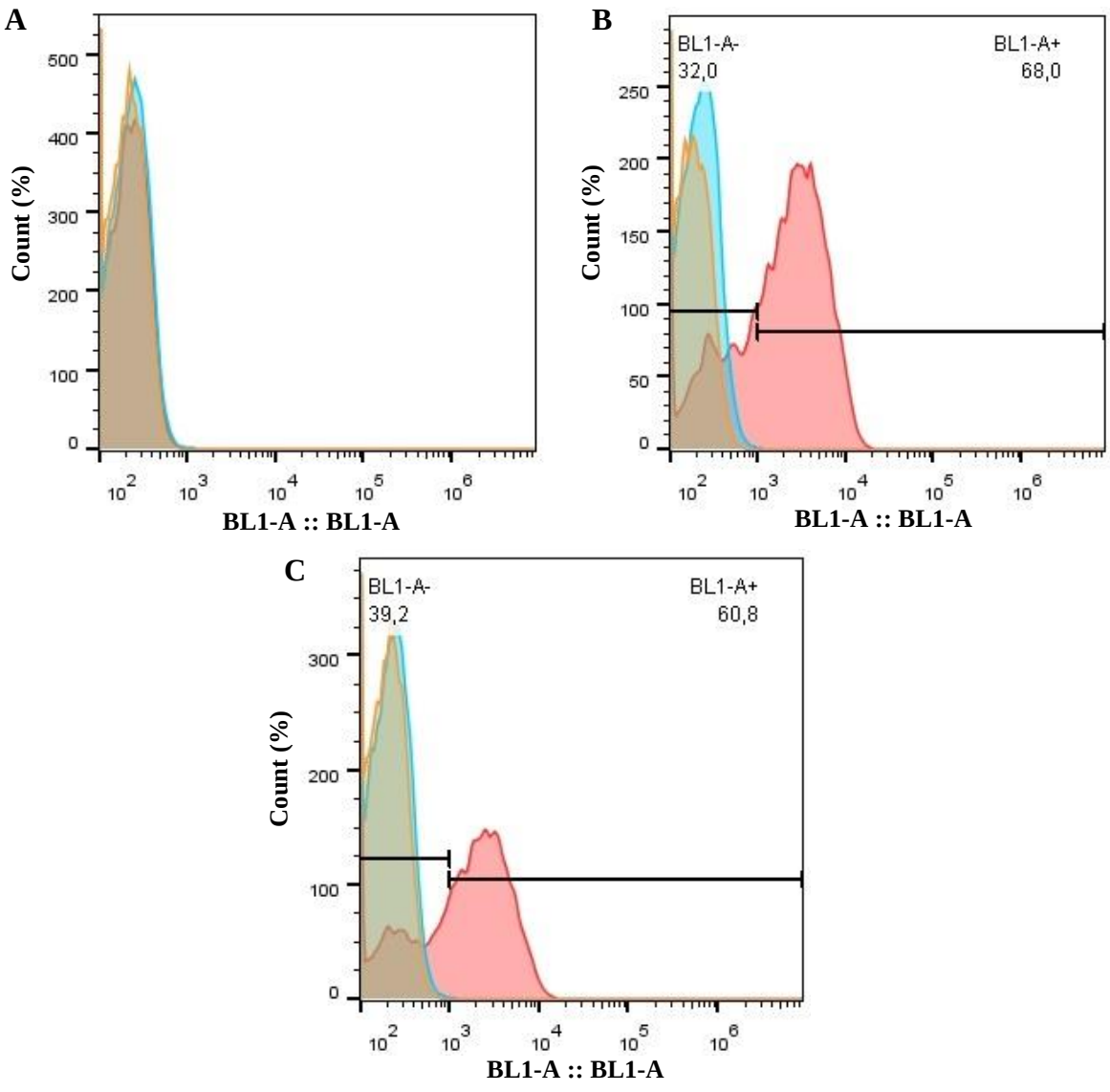

Figure 8.1. Flow cytometry analysis of MDA-MB-231 WT (A) and MDA-MB-231 STn (B and C) cell lines expression of STn. Figures B and C represents the different cellular passages of MDA-MB-231 STn cell line: passage number three and ten, respectively. Orange histograms corresponds to the negative control, i.e., only the cells; blue histograms corresponds to the negative staining control, i.e., cells stained with only the secondary antibody and red histograms represents the staining of B72.3 mouse anti-STn antibody (primary antibody).

Figure 8.1 (A) represents the experiment control, where B72.3 mouse anti-STn antibody was used only to realize that there is no binding of this antibody to the WT cells, since the sialyl Tn antigen is absent on the surface of this cells type. On the other hand, Figure 8.1 (B) allowed to observe that almost 70% of the population is positive for BL1, the channel for which the secondary antibody fluorescence, that binds to B72.3 antibody, is read. For this reason, it can be concluded that MDA-MB-231 STn cell line have approximately 70% of the cells expressing STn. Furthermore, Figure 8.1 (C) represents that the stable expression of STn in this cell line remain and is stable way throughout several passages (in this case, 9-10 passages) as already concluded by Glicoimmunology Group (Reis 2014). In this way, the subsequent cellular assays were performed taking into account the constant and high expression of STn in order to guarantee no variability in the obtained results.

9. Iron oxide nanoparticles internalization in cultured cells

9.1. Cytotoxicity Assays

The first step towards understanding how an agent will react in the body often involves cell-culture studies. In the case of cytotoxicity, it is important to recognize that cell cultures are sensitive to changes in their environment such as fluctuations in temperature, pH, and nutrient and waste concentrations, in addition to the concentration of the potentially toxic agent being tested. Therefore, controlling the experimental conditions is crucial to ensure that the measured cell death corresponds to the toxicity of the added nanoparticles versus the unstable culturing conditions. In addition, as nanoparticles can adsorb dyes and be redox active, it is important that the cytotoxicity assay is appropriate (Mosmann 1983; Lewinski *et al.* 2008). The cytotoxicity of the iron oxide cores was evaluated for OA 64 mM and DMSA 13 mM coated Fe_3O_4 NPs by 3-(4,5-dimethylthiazol-2-yl)-5-(3-carboxymethoxyphenyl)-2-(4-sulfophenyl)-2H-tetrazolium (MTS) assay in MDA-MB-231 WT and MDA-MB-231 STn cell lines as described in 6.2.2.1.1. section of Part III.

The results are expressed as % of cell viability calculated by [% cell viability = NP treated cells/control cells x 100]. Control cells were maintained with the same condition as the tested ones, without the addition of nanoparticles. Figure 9.1 and Figure 9.2 shows the obtained results for cell viability after 24 hours of exposition to OA 64 mM coated NPs and DMSA 13 mM coated Fe_3O_4 NPs on the two breast cancer cell lines, respectively.

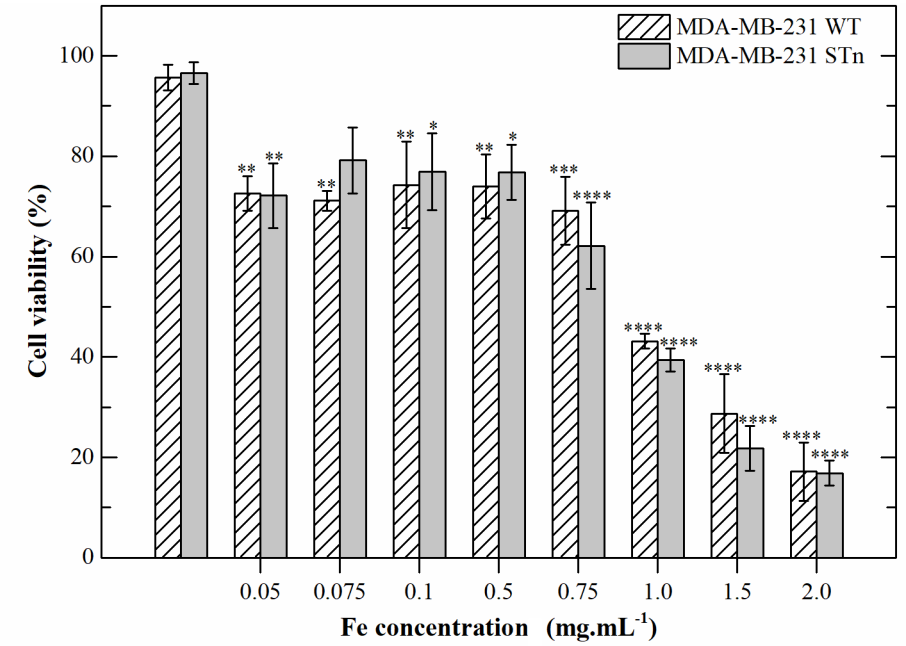

Figure 9.1. MDA-MB-231 WT and MDA-MB-231 STn cell lines viability after 24 h exposition to OA 64 mM coated NPs. Data is expressed as average ± standard deviation for at least three independent experiments. *p<0.05, **p<0.005, ****p<0.0001 compared to untreated control cells (in blank in xx axis).

The results show that for both MDA-MB-231 WT and MDA-MB-231 STn cell lines the variation in cell viability remains relatively constant over the range of concentrations described. It should be noted that from an iron concentration of 1.0 mg.mL^{-1} the cell viability is reduced up to about 40%, thus causing severe cytotoxic effects.

Although the study has been performed in different cell lines, Soares *et al.* revealed that from an iron concentration of 500 μg.mL^{-1} the cell viability of Vero cells, a fibroblast-like kidney cell, and SaOs-2, an osteosarcoma cell line, is reduced up to 20% under the effect of NPs coated with the same concentration of oleic acid as used in this study (64 mM) (Soares *et al.* 2015; Soares et al. 2016).

From the results obtained in the two breast cancer cell lines it is concluded that this stabilizing agent causes deleterious effects on the cells from lower concentrations when compared to the other used stabilizer, DMSA (Figure 9.2). As from an iron concentration of 1 mg.mL^{-1} these magnetic nanoparticles turns toxic for both cell lines, the further internalization studies were performed at lowest concentrations.

The surface coating of the NPs is an important parameter to be analyzed to allow us to know its cellular toxicity/biocompatibility potential. Therefore, these cell viability assays were done in order to understand which of the two types of stabilizing agent is the one that translates lesser cytotoxicity effects.

Several reports have described little effects on cell viability, oxidative stress, cell cycle or apoptosis for DMSA coated iron oxide nanoparticles (Calero *et al*. 2014; Singh *et al.* 2010; Mejias *et al.* 2010; Mejías *et al.* 2011).

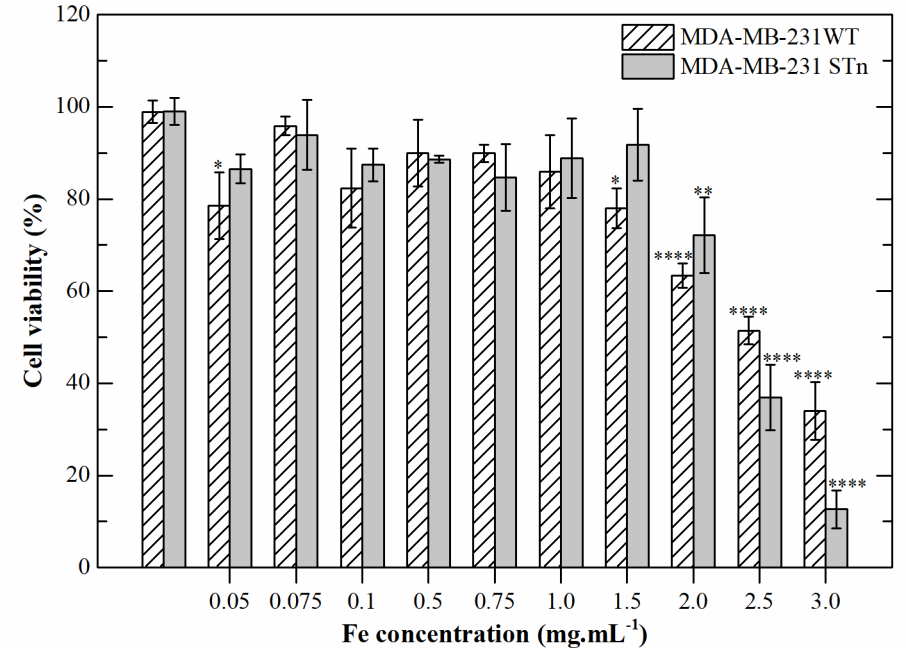

Figure 9.2. MDA-MB-231 WT and MDA-MB-231 STn cell lines viability after 24 h exposition to DMSA 13 mM coated NPs. Data is expressed as average ± standard deviation for at least three independent experiments. *p<0.05, **p<0.005, ****p<0.0001 compared to untreated control cells (in blank in xx axis).

From the results shown in Figure 9.2 it can be conclude that both MDA-MB-231 WT and MDA-MB-231 STn cell lines do not demonstrate significant toxicity to DMSA 13 mM coated Fe_3O_4 NPs in the range of 0.05–2.0 $mg.mL^{-1}$. From this concentration, these magnetic nanoparticles turns toxic for both cell lines and the cell viability is reduced up to about 60% to 40%. Dispite Mejíaz *et al.* have been performed cytotoxicity assays in HeLa cells, the cell viability for some concentrations studied here are similar to those reported by the authors where, for a concentration below 0.5 $mg.mL^{-1}$ the cell culture viability was not notably affected or modified by nanoparticles at 24 hours post-treatment as it happens with the breast cancer cells used in the present study (Mejias *et al*. 2010). Therefore, it can be concluded that the DMSA coating causes a much lower toxicity impact when compared to the use of oleic acid as a stabilizing agent.

9.2. Cell exposure to iron oxide nanoparticles and uptake studies

9.2.1. Qualitative uptake study

Size, shape and charge of SPIONs, as well as cell type, are important parameters which affect effective internalization of nanoparticles into cells in culture (Mahmoudi *et al.* 2011). The evaluation of the potential use of magnetic nanoparticles in biomedical applications requires a precise knowledge of surface modified NP internalization mechanisms at the ultrastructural level and resulting intracellular pathways, as well as on the fate of nanoparticles inside the cells. Factors such as uptake rate and internalization dynamics are the key to understand how an insufficient cellular accumulation of nanoparticles can lead to usage limitations, for example as imaging probes and in magnetic hyperthermia therapy (Huang *et al*. 2009; Calero *et al.* 2015).

Figures 9.3 and 9.4 shows the internalization qualitative study of OA 64 mM and DMSA 13 mM coated Fe_3O_4 NPs in MDA-MB-231 WT and MDA-MB-231 STn cell lines, respectively, at a range of iron concentrations from 0.05 $mg.mL^{-1}$ to 0.1 $mg.mL^{-1}$. For this test the Prussian Blue Staining technique was reproduced in both untreated control (see in Appendix III) and NPs treated cells, in which uptake of nanoparticles is visualized (blue color) inside the cells by contrast between the red and pink colors which are produced from the nuclei and cytoplasm staining (Gu *et al*. 2011; Villanueva *et al.* 2009; Liao *et al.* 2015; Wang *et al*. 2012; Cengelli *et al.* 2009).

From Figure 9.3 it can be verified that as the NPs concentration increases (A to E, B to F, G to K and H to L) also the nanoparticles internalization increases in the MDA-MB-231 WT cell line. However, a significant difference is observed: DMSA coated nanoparticles (G to L) have a larger potential for internalization due to the greater clusters formation in this cell line comparing to the oleic acid stabilized NPs (A to F), for the same range of administered NPs concentrations.

In several cases it has been shown that a simple DMSA coating can improve uptake efficiency by three orders of magnitude, presumably by engendering the NPs with an anionic charge, resulting in nonspecific adsorption to the cell surface followed by endocytosis into the cell (Pisanic *et al.* 2007; Billotey *et al.* 2003; Wilhelm *et al.* 2003).

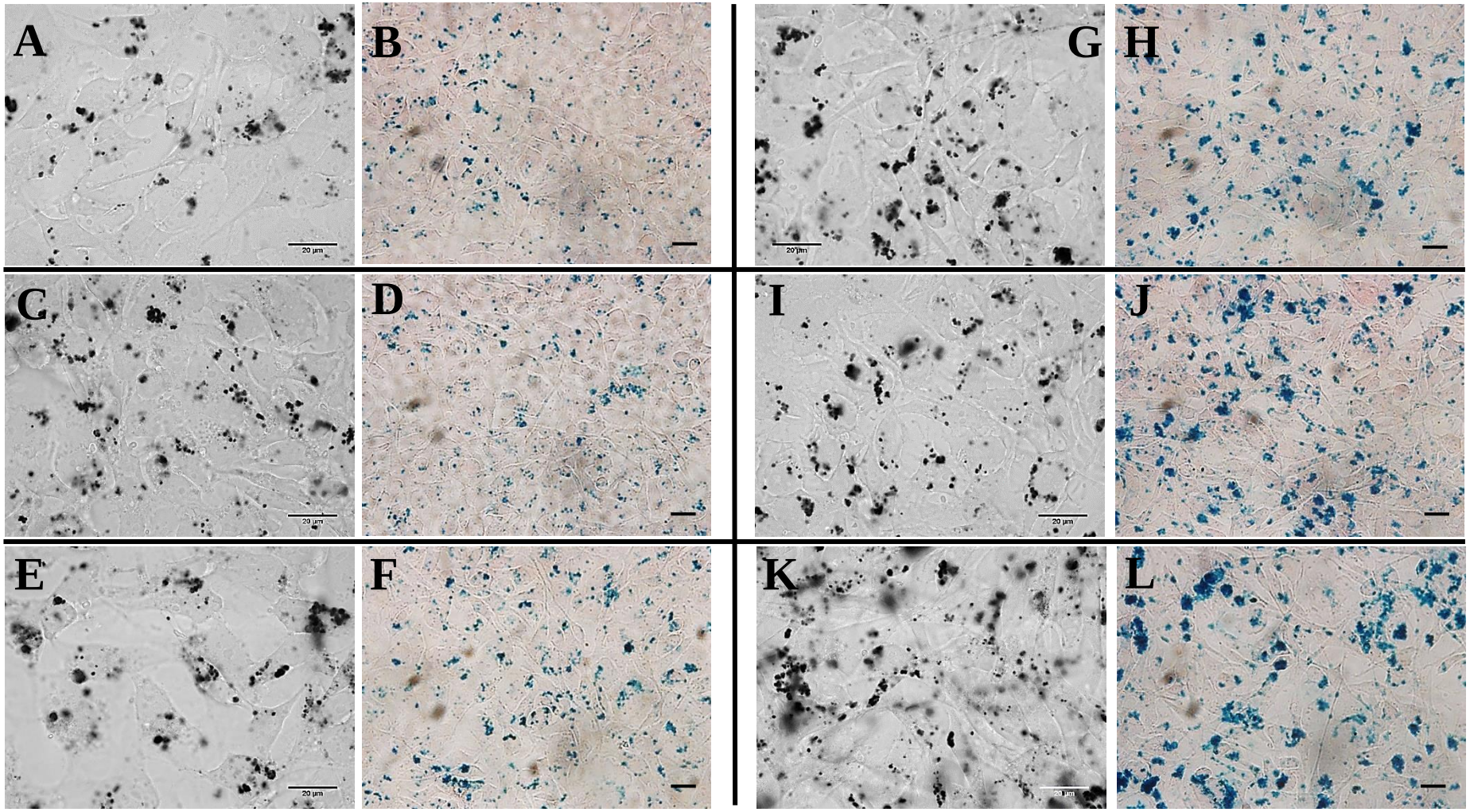

Figure 9.3. Bright field microscopy visualization of MDA-MB-231 WT cells incubated with OA 64 mM coated Fe_3O_4 NPs and DMSA 13 mM coated Fe_3O_4 NPs at a range of iron concentrations from 0.05 mg.mL^{-1} to 0.1 mg.mL^{-1}. (A, C, E and B, D, F) MDA-MB-231 WT cells incubated with 0.05, 0.075 and 0.1 mg.mL^{-1} of OA 64 mM coated Fe_3O_4 NPs, with a 100x objective magnification (black and white images) and 50x objective magnification (colored images). (G, I, K and H, J, L) MDA-MB-231 WT cells incubated with 0.05, 0.075 and 0.1 mg.mL^{-1} of DMSA 13 mM coated Fe_3O_4 NPs, with a 100x objective magnification (black and white images) and 50x objective magnification (colored images). Scale bar for both black and white and colored images represents 20 µm.

The surface charge of iron oxide nanoparticles has an important role in cell internalization. Although both coatings (OA and DMSA) provide a negative charge to the NPs, the greater internalization of DMSA coated NPs occurs since these nanoparticles have a surface charge value higher (-53.8 mV) than those conjugated with oleic acid (-111.2 mV) (Figure 7.7, section 7.5) and therefore there is a non-specific adsorption preference for DMSA coated NPs in cells.

These results are due to the fact that the cell membrane is negatively charged and thus has a greater tendency to internalize/endocyte molecules that have contrary charge, as it was shown by Calero *et al.*, where a higher internalization efficiency of cationic nanoparticles (coated with 3-aminopropyl-triethoxysilane - APS) was compared with the lower DMSA coated nanoparticles internaliazation (Calero *et al.* 2014). However, it is also proven that the anionic surfaces increase cell uptake by endocytosis and in specific, due to their small particle hydrodynamic size and anionic surface DMSA coated nanoparticles create an ideal material for cell labeling (Mejias *et al.* 2010; Berry 2009; L Harivardhan Reddy *et al*. 2012).

From Figure 9.4, which shows the internalization study of the two types of NPs in the MDA-MB-231 STn cell line, two obvious conclusions can be drawn: (i), NPs internalization increases proportionally to the increase of OA 64 mM (A to F) and DMSA 13 mM coated Fe_3O_4 NPs (G to L) concentrations as in the previous study and (ii), although it is slightly more pronounced in the DMSA coated nanoparticles, the uptake of the two types of NPs in MDA-MB-231 STn cell line seems to be similar.

This cell line has in particular a carbohydrate antigen sialyl-Tn (STn) which occurs in approximately 90% of human cancers, such as breast, bladder and prostate cancer (Yu 2007). It would be possible to predict a lower nanoparticles internalization in this type of cells, since the antigen sialyl-Tn (STn) has a negative charge (Pinho *et al.* 2007; Kim and Varki 1997; Schoonbroodt *et al.* 2008).

Despite the negative charge that STn presents, the presence of a sialic acid called *N*-Acetylneuraminic acid commonly found in the terminal position of this glycan can reveal the possibility of a specific binding with the coating molecules of NPs.

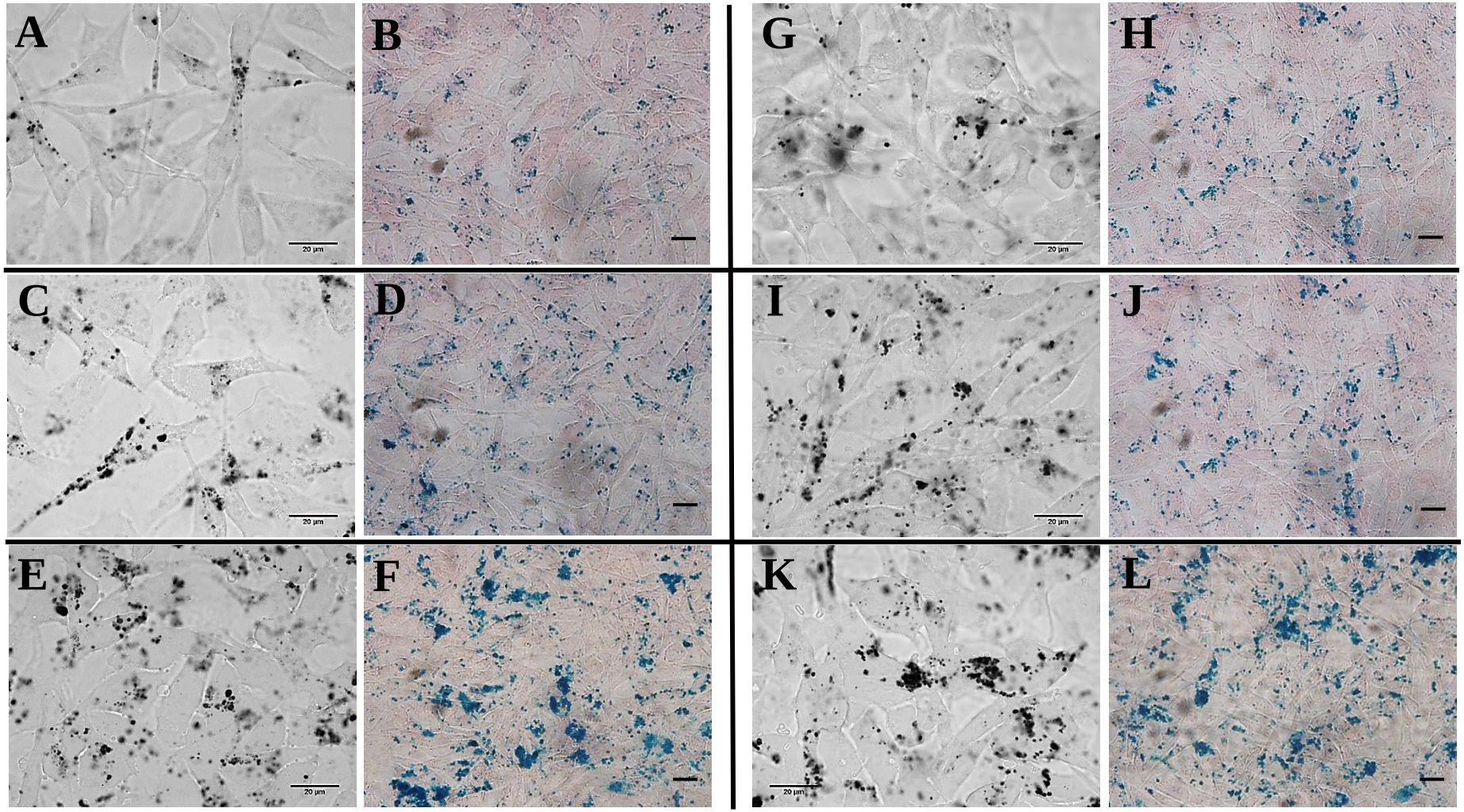

Figure 9.4. Bright field microscopy visualization of MDA-MB-231 STn cells incubated with OA 64 mM coated Fe_3O_4 NPs and DMSA 13 mM coated Fe_3O_4 NPs at a range of iron concentrations from 0.05 mg.mL^{-1} to 0.1 mg.mL^{-1}. (A, C, E and B, D, F) MDA-MB-231 STn cells incubated with 0.05, 0.075 and 0.1 mg.mL^{-1} of OA 64 mM coated NPs, with a 100x objective magnification (black and white images) and 50x objective magnification (colored images). (G, I, K and H, J, L) MDA-MB-231 STn cells incubated with 0.05, 0.075 and 0.1 mg.mL^{-1} of DMSA 13 mM coated Fe_3O_4 NPs, with a 100x objective magnification (black and white images) and 50x objective magnification (colored images). Scale bar for both black and white and colored images represents 20 µm.

These type of sialic acids have important biological roles, such as interactions of the molecules and cells with the environment (Varki and Schauer 2009; Schauer 2000). As can be seen in Figure 9.5, this monosaccharide has a carbonyl group (C=O), which may be available for a chemical bond sharing with the functional groups of the NPs stabilizing molecules (OA and DMSA).

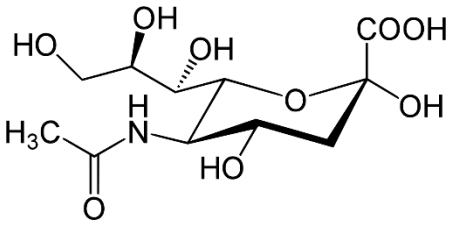

Figure 9.5. ***N*-Acetylneuraminic acid chemical structure.**

The DMSA molecules on the NPs surface have sulfur atoms that derive from the thiol (SH) groups and the carboxyl groups (COOH) which are present in the oleic acid bilayer and do not form a bond with the nanoparticles surface can be responsible for the specific binding of the NPs to the breast cancer cells expressing STn antigen. In this way it is thought that, both the occurrence of nucleophilic attacks of sulfur atoms (DMSA) and -OH group of the carboxylic acid (OA) to the carbon atom of the carbonyl group present in sialic acid can lead to the formation of covalent bonds between the different molecules, ensuring the binding of NPs to the cells.

A known method of nanoparticles internalization in cells is based on a receptor-mediated approach, whereby specific ligands are convalently linked to the NPs molecules coating in order to induce cell membrane receptor recognition followed by subsequent endocytosis, as indicated in Figure 9.6 (Wilhelm and Gazeau 2008; Berry 2009).

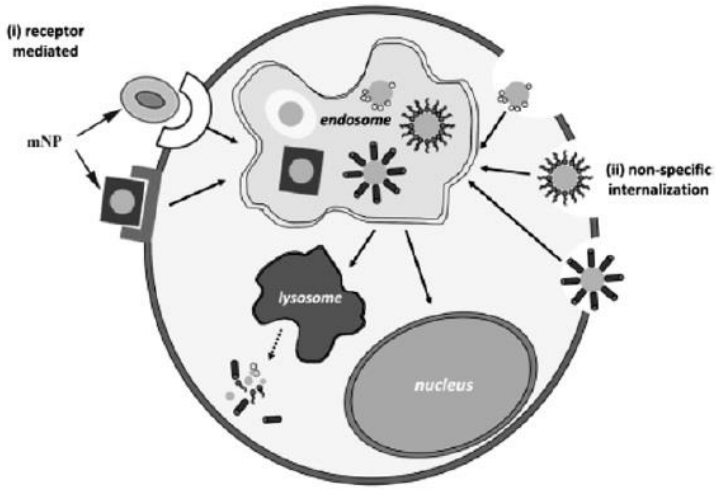

Figure 9.6. Representation of non-specific (at the right of the cell) and specific (at the left of the cell) cell uptake of NPs. In both cases the particles are localized in endosomes, being either released into the cell or trafficked to the lysosomes for degradation. Adapted from (Berry 2009).

Thus, two distinct conclusions can be done: (i) OA and DMSA coated NPs internalization in the MDA-MB-231 WT cell line is considered as non-specific, since the nanoparticles can enter the cell without any receptor involvement; (ii) while the internalization of the same nanoparticles in the MDA-MB-231 STn cell line represents an NP-cell binding mediated by a receptor, which in this case is believed to be the *N*-Acetylneuraminic sialic acid which constitutes the STn antigen. Therefore, as it can be seen the cellular internalization of NPs is much more effective in this last case.

The Prussian Blue technique implemented in this study only allows the visualization of the nanoparticles uptake in the cells. In other hand, to study the nanoparticles subcellular localization a LysoTracker Red would have to be used in order to stain the lysosomal compartment and conclude about their accumulation in endosome/lysosome fractions (Villanueva *et al.* 2009; Calero *et al.* 2014; Calero *et al.* 2015).

9.2.2. Quantitative uptake study

To evaluate the SPIONs internalization in a quantitative way many techniques are in use, including ultraviolet spectrophotometry (UV-Vis) (Liao *et al.* 2015). Colorimetric methods commonly employed for the quantitation of complexed iron in biological samples rely on an initial treatment which releases the complexed iron for its subsequent quantitative determination (Fish 1988). For this reason, 1,10-phenantroline colorimetric method was used in order to determine the iron concentration in cultured cells (Yallapu *et al.* 2010; Yallapu *et al.* 2011).

The qualitative iron uptake study can be confirmed by the quantitative analyses of intracellular iron uptake shown in Figure 9.7 (A) and (B). After 24 and 48 hours of incubation with OA 64 mM and DMSA 13 mM Fe_3O_4 NPs the iron uptake in cells shows a gradual increase, considering that from 0.1 to 0.5 $mg.mL^{-1}$ exists an exponential increase. This effect may be due to the accumulation of larger agglomerates within the cells taking into account the highest concentration administered.

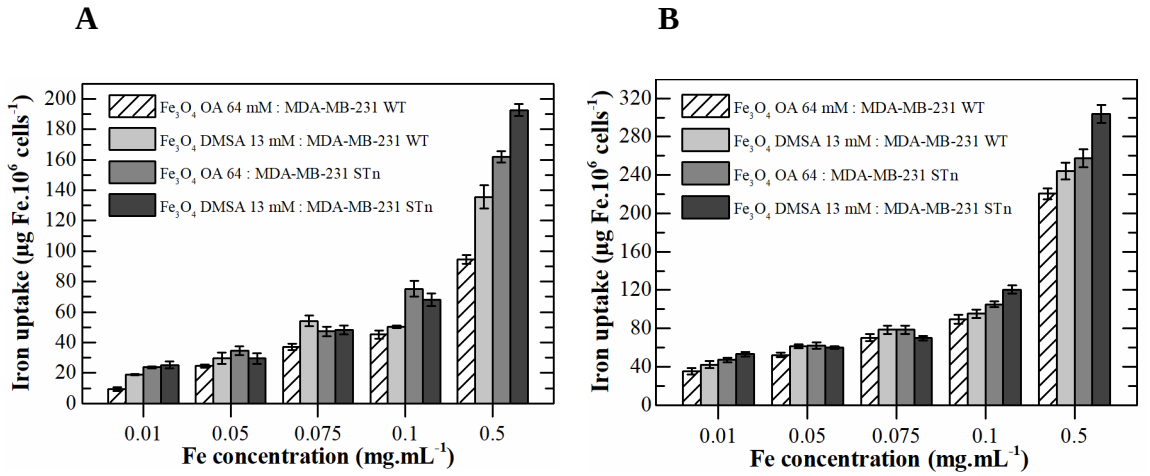

Figure 9.7. Intracellular iron content quantification by 1,10-phenantroline colorimetric method. The iron uptake is expressed as weight of iron per 1×10^6 cells and measured after 24 h (A) and 48 h (B) of OA 64 mM Fe_3O_4 NPs and DMSA 13 Fe_3O_4 NPs incubation in MDA-MB-231 WT and MDA-MB-231 STn cell lines. Data is expressed as average ± standard deviation for at least three independent experiments.

In general, it is possible to conclude that the MDA-MB-231 STn cells can absorb more NPs than the WT cell line and, for most of the concentrations tested, nanoparticles coated with DMSA have a higher internalization rate than those stabilized with oleic acid.

It can also be said that after 48 hours of nanoparticles incubation the concentration of absorbed iron is almost twice superior when compared with the values from 24 hours of iron uptake. In this way, sufficient intracellular uptake of OA 64 mM and DMSA 13 mM Fe_3O_4 NPs can predict that exists a great possibility to consider these magnetic nanoparticles as good heat generators for *in vitro* magnetic hyperthermia since larger amounts of nanoparticles inside the cells can induce a greater capacity to produce heat (Majetich *et al.* 2013).

Part V

Concluding Remarks and Future Perspectives

Cancer is a devastating disease of the present days with a huge incidence and related deaths. It is estimated that each year more than 11 million new cases of cancer are diagnosed, and more than 7 million people die from this devastating disease. If current trends continue, in 2020 new cancer cases will increase to 17 million, an increase of 30% compared to 2009.

In the past 20 years, the total medical costs of cancer have nearly doubled as a direct consequence of the increasing number of cancer cases. The dramatic increase in the number of cancer cases is because of new diagnostics among the aging population base, as well as increasing cancer prevalence.

Current cancer treatments, such as radiotherapy and chemotherapy, although effective for some cases, did no cover all of them. In addition, cancer treatment is exhaustive and expensive because of the multi-therapeutic approaches and constant admissions for treatments and side effects management. Most of cancer treatments are not specific for the type of cancer and for the patient, and treatment monitoring is not accurate.

Nanotechnology is a recent technology with a huge potential for medicine, among other applications. Properties like increased surface area, optical, electronic, magnetic, and structural properties at nanometer scale are not available for bulk solids or individual molecules, making these materials unique. The development of new materials based on multi-functional magnetic nanoparticles can open a window of opportunity for a new therapeutic approach to cancer treatment.

Therefore, the main goal of this project was to develop a possible therapy system based on superparamagnetic iron oxide nanoparticles and promote their internalization into cancer cell lines in order to predict their potential as heat sources for cancer treatment by magnetic hyperthermia.

Initially, iron oxide nanoparticles were synthesized using a chemical co-precipitation method with subsequent surface modification. To evaluate the stabilization of the coated nanoparticles with oleic acid and DMSA, several characterization techniques were performed. Through structural characterization it was possible to verify that coated nanoparticles retained the crystal structure of naked NPs and although the coating has correctly occurred, since the characteristic peaks which represents the presence of the stabilizing agents was visualized by FTIR spectroscopy.

The properties of the iron oxide nanoparticles were analyzed after modification and no alteration of properties was observed with coating (size and crystalline structure). In addition, the coating constitutes further stability to the nanoparticles. Morphological characterization showed that nanoparticles coated with OA and DMSA have a core size similar to the NPs that have not experienced stabilization (8 to 9 nm), so, it can be concluded that the binding of these molecules to nanoparticles surface does not negatively influence the NPs core structure.

However, in order to better understand the influence of these stabilizing agents, DLS and zeta potential studies were developed to determine the hydrodynamic diameter and charge/stability, respectively, of the NPs after their modification. A significant difference was observed with respect to the size of each type of coated NPs where it was found that DMSA conjugated iron oxide nanoparticles have a smaller hydrodynamic diameter when compared to NPs stabilized with the oleic acid surfactant.

Also, the charge of both NPs is different, however, both OA and DMSA coating revealed a great stability in aqueous medium for the produced NPs.

After complete characterization of the coated nanoparticles, *in vitro* internalization studies were performed in order to conclude about the influence of NPs coating in cell uptake. To perform these assays, it was necessary to found which nanoparticles concentrations could be used without causing toxic effects in two types of breast cancer cell lines: MDA-MB-231 WT and MDA-MB-231 STn. It was determined that for concentrations of 1 $mg.mL^{-1}$ and 2.5 $mg.mL^{-1}$ of NPs coated with oleic acid and DMSA, respectively, the cell viability of both cell lines drops to approximately 40-50%. Therefore, to carry out the internalization tests smaller concentrations of coated NPs were used.

Through these tests it was possible to conclude that two types of cellular internalization may occur: (i) non-specific internalization of NPs, or (ii) receptor-mediated internalization. It was possible to admit these conclusions, since when increasing the concentration of both OA and DMSA internalized NPs in MDA-MB-231 WT cell line, a greater retention of the nanoparticles coated with DMSA is verified, whereas, when it comes to the internalization of both NPs in the MDA-MB-231 STn cell line this significant difference does not occur. Knowing this effect, it can be concluded that the STn antigen present on cells surface represents a receptor capable of detecting and covalently binding to the molecules presents in nanoparticles surface and, in this way, inducing their cellular uptake by endocytosis. To better elucidate this phenomenon, qualitative studies were carried out to corroborate the previous ones, which agreed with them.

In conclusion, internalization tests were successfully developed, however more optimizations will be required, such as the cell density to be used in study and also the procedure of a subcellular NPs localization study should be taken into account in order to understand which the organelles where coated nanoparticles are preferentially located.

Another aspect to be considered is the carrying out of all the performed studies throughout this thesis with the nanoparticles functionalized with the monoclonal antibody against the sialyl-Tn (STn) antigen. In this way it will be possible to evaluate the influence of this antibody in binding, specific or not, to the cells expressing STn.

It will be of great interest to carry out *in vitro* magnetic hyperthermia assays in order to conclude about the necessary concentration of NPs to be used, the best type of coating for the desired effect, the influence that the monoclonal antibody can bring (increasing or decreasing the power of internalization and, therefore, also changing the effect of hyperthermia) and still understand the effect of the same NPs in other cancer cell lines types. All these aspects should be evaluated considering cancer cell killing as the main objective.

In addition to the use of stabilized iron oxide nanoparticles for cancer treatment, another function may be given to this type of NPs, such as their use as contrast agents for magnetic resonance imaging, since these NPs appear to be the preferred MRI contrast agents for monitoring cells due to their high sensitivity and excellent biocompatibility.

Thus, the development of a highly optimized theranostic (therapy + diagnostic) system would be a benefit for the evolution of nanomedicine in oncology field, taking the magnetic properties of superparamagnetic iron oxide nanoparticles as an advantage.

References

Absolom, D.R., Zingg, W. and Neumann, A.W., 1987. Protein adsorption to polymer particles: Role of surface properties. *Journal of Biomedical Materials Research*, 21(2), pp.161–171.

Ahmed, M. and Douek, M., 2013. The role of magnetic nanoparticles in the localization and treatment of breast cancer. *BioMed Research International*, 2013.

Akbarzadeh, A., Samiei, M. and Davaran, S., 2012. Magnetic nanoparticles: preparation, physical properties, and applications in biomedicine. *Nanoscale Research Letters*, 7(1), p.144.

Ali, A. et al., 2016. Synthesis, characterization, applications, and challenges of iron oxide nanoparticles. *Nanotechnology, Science and Applications*, 9, pp.49–67.

Aliakbari, A. et al., 2015. Influence of different synthesis conditions on properties of oleic acid-coated-Fe3O4 nanoparticles. *Materials Science*, 33(1), pp.100–106.

Arruebo, M. et al., 2007. Magnetic nanoparticles for drug delivery. *Nano Today*, 2(3), pp.22–32.

Attaluri, A. et al., 2015. Magnetic nanoparticle hyperthermia enhances radiation therapy: A study in mouse models of human prostate cancer. *International Journal of Hyperthermia*, 31(4), pp.359–374.

Babincová, M., Sourivong, P., et al., 2000. Blood-specific whole-body electromagnetic hyperthermia. *Medical hypotheses*, 55(6), pp.459–460.

Babincová, M., Leszczynska, D., et al., 2000. Selective treatment of neoplastic cells using ferritin-mediated electromagnetic hyperthermia. *Medical hypotheses*, 54(2), pp.177–179.

Berry, C.C., 2009. Progress in functionalization of magnetic nanoparticles for applications in biomedicine. *Journal of Physics D: Applied Physics*, 42(22), p.224003.

Bertozzi CR and Rabuka D, Structural Basis of Glycan Diversity, in: A. Varki, R.D. Cummings, J.D. Esko, H.H. Freeze, P. Stanley, C.R. Bertozzi, G.W. Hart, M.E. Etzler (Eds.), Essentials Glycobiol., 2nd ed., Cold Spring Harbor, NY: Cold Spring Harbor Laboratory Press. Available from: http://www.ncbi.nlm.nih.gov/books/NBK1955/, 2009.

Billotey, C. et al., 2003. Cell internalization of anionic maghemite nanoparticles: Quantitative effect on magnetic resonance imaging. *Magnetic Resonance in Medicine*, 49(4), pp.646–654.

Bini, R.A. et al., 2012. Synthesis and functionalization of magnetite nanoparticles with different amino-functional alkoxysilanes. *Journal of Magnetism and Magnetic Materials*, 324(4), pp.534–539.

Blanpain, C., 2013. Tracing the cellular origin of cancer. *Nature Cell Biology*, 15(2), pp.126–134.

Brockhausen, I. et al. O-GalNAc Glycans, in: A. Varki, R.D. Cummings, J.D. Esko, H.H. Freeze, P. Stanley, C.R. Bertozzi, G.W. Hart, M.E. Etzler (Eds.), Essentials Glycobiol., 2nd ed., Cold Spring Harbor (NY): Cold Spring Harbor Laboratory Press. Available from: http://www.ncbi.nlm.nih.gov/books/NBK1896/, 2009.

Cailleau, R. et al., 1974. Breast tumor cell lines from pleural effusions. *Journal of the National Cancer Institute*, 53(3), pp.661–674.

Calero, M. et al., 2015. Characterization of interaction of magnetic nanoparticles with breast cancer cells. *Journal of Nanobiotechnology*, 13(1), p.16.

Calero, M. et al., 2014. Efficient and safe internalization of magnetic iron oxide nanoparticles: Two fundamental requirements for biomedical applications. *Nanomedicine: Nanotechnology, Biology, and Medicine*, 10(4), pp.733–743.

Cancer Research UK, 2014a. Worldwide cancer incidence statistics. Available at: http://www.cancerresearchuk.org/health-professional/cancer-statistics/worldwide-cancer/incidence [Accessed August 30, 2017].

Cancer Research UK, 2014b. Worldwide cancer statistics. Available at: http://www.cancerresearchuk.org/health-professional/cancer-statistics/worldwide-cancer [Accessed August 30, 2017].

Cazet, A. et al., 2010. Tumour-associated carbohydrate antigens in breast cancer. *Breast Cancer Research*, 12(3), p.204.

Cengelli, F. et al., 2009. Surface-functionalized ultrasmall superparamagnetic nanoparticles as magnetic delivery vectors for camptothecin. *ChemMedChem*, 4(6), pp.988–997.

Chen, Z.P. et al., 2008. Preparation and characterization of water-soluble monodisperse magnetic iron oxide nanoparticles via surface double-exchange with DMSA. *Colloids and Surfaces A: Physicochemical and Engineering Aspects*, 316(1–3), pp.210–216.

Consortium for Functional Glycomics, 2012. Symbol and Text Nomenclature for Representation of Glycan Structure. Available at: http://www.functionalglycomics.org/static/consortium/Nomenclature.shtml [Accessed September 1, 2017].

Cooper, G., 2000. The Development and Causes of Cancer. *The Cell: A Molecular Approach. 2nd edition*. Available at: https://www.ncbi.nlm.nih.gov/books/NBK9963/ [Accessed August 30, 2017].
Corporation, L.T., 2011. Attune ® Acoustic Focusing Cytometer.

da Costa, G.M. et al., 1994. Synthesis and Characterization of Some Iron Oxides by Sol-Gel Method. *Journal of Solid State Chemistry*, 113(2), pp.405–412.

Dodrill, B., 2012. Characterizing Permanent Magnet Materials With a Vibrating Sample Magnetometer. *Magnetics Magazine*. Available at: http://www.magneticsmagazine.com/main/channels/test-measurement/characterizing-permanent-magnet-materials-with-a-vibrating-sample-magnetometer/ [Accessed August 10, 2017].

Faiyas, A.P.A. et al., 2010. Dependence of pH and surfactant effect in the synthesis of magnetite (Fe3O4) nanoparticles and its properties. *Journal of Magnetism and Magnetic Materials*, 322(4), pp.400–404.

Farhat Hadj, M.A. and Joubert, J.C., 1986. Hydrothermal synthesis and characterisation of the hexagonal ferrite Fe_2-Y., 62, pp.353–358.

Fauconnier, N. et al., 1997. Thiolation of Maghemite Nanoparticles by Dimercaptosuccinic Acid. *Journal of Colloid and Interface Science*, 194(2), pp.427–433.

Feng, D., Shaikh, A.S. and Wang, F., 2016. Recent Advance in Tumor-associated Carbohydrate Antigens (TACAs)-based Antitumor Vaccines. *ACS Chemical Biology*, 11(4), pp.850–863.

Ferreira, J.A. et al., 2013. Overexpression of tumour-associated carbohydrate antigen sialyl-Tn in advanced bladder tumours. *Molecular Oncology*, 7(3), pp.719–731.

Fish, W.W., 1988. Rapid Colorimetric Micromethod for the Quantitation of Complexed Iron in Biological Samples. *Methods in Enzymology*, 158, pp.357–364.

Friedrich, R.P. et al., 2015. Flow cytometry for intracellular SPION quantification: specificity and sensitivity comparison with spectroscopic methods. *International Journal of Nanomedicine*, 10(1), p.4185.

Frisken, B.J., 2001. Revisiting the Method of Cumulants for the Analysis of Dynamic Light-Scattering Data. *Applied Optics*, 40(24), p.4087.

Galli, M. et al., 2017. Superparamagnetic iron oxide nanoparticles functionalized by peptide nucleic acids. *RSC Adv.*, 7(25), pp.15500–15512.

Gass, J. et al., 2006. Superparamagnetic polymer nanocomposites with uniform Fe_3O_4 nanoparticle dispersions. *Advanced Functional Materials*, 16(1), pp.71–75.

Ge, Y. et al., 2009. Effect of surface charge and agglomerate degree of magnetic iron oxide nanoparticles on KB cellular uptake in vitro. *Colloids and Surfaces B: Biointerfaces*, 73(2), pp.294–301.

Gilchrist, R.K. et al., 1957. Selective Inductive Heating of Lymph Nodes. *Annals of surgery*, 146(4), pp.596–606.

Gnanaprakash, G., Philip, J., et al., 2007. Effect of digestion time and alkali addition rate on physical properties of magnetite nanoparticles. *Journal of Physical Chemistry B*, 111(28), pp.7978–7986.

Gnanaprakash, G., Mahadevan, S., et al., 2007. Effect of initial pH and temperature of iron salt solutions on formation of magnetite nanoparticles. *Materials Chemistry and Physics*, 103(1), pp.168–175.

Gordon, R.T., Hines, J.R. and Gordon, D., 1979. Intracellular hyperthermia a biophysical approach to cancer treatment via intracellular temperature and biophysical alterations. *Medical Hypotheses*, 5(1), pp.83–102.

Goya, G.F., Grazú, V. and Ibarra, M.R., 2008. Magnetic Nanoparticles for Cancer Therapy. *Current Nanoscience*, 4, pp.1–16.

Gu, J.L. et al., 2011. The internalization pathway, metabolic fate and biological effect of superparamagnetic iron oxide nanoparticles in the macrophage-like RAW264.7 cell. *Science China Life Sciences*, 54(9), pp.793–805.

Gupta, A.K. and Gupta, M., 2005. Synthesis and surface engineering of iron oxide nanoparticles for biomedical applications. *Biomaterials*, 26(18), pp.3995–4021.

Hamley, I.W., 2003. Nanotechnology with Soft Materials. *Soft Nanomaterials*, 115(15), pp.1730–1752.

Hanahan, D. and Weinberg, R.A., 2011. Hallmarks of cancer: The next generation. *Cell*, 144(5), pp.646–674.

Hanahan, D. and Weinberg, R.A., 2000. The hallmarks of cancer. *Cell*, 100(1), pp.57–70.

Hermanson G. T., Bioconjugate Techniques, Third edition ed., Elsevier, London, 2013.

Hilger, I. et al., 2001. Electromagnetic Heating of Breast Tumors in Interventional Radiology: In Vitro and in Vivo Studies in Human Cadavers and Mice. *Radiology*, 218(2), pp.570–575.

Ho, D., Sun, X. and Sun, S., 2011. Monodisperse magnetic nanoparticles for theranostic applications. *Accounts of Chemical Research*, 44(10), pp.875–882.

Hola, K. et al., 2015. Tailored functionalization of iron oxide nanoparticles for MRI, drug delivery, magnetic separation and immobilization of biosubstances. *Biotechnology advances*, 33(6), pp.1162–1176.

Hong, R.Y. et al., 2009. Preparation and characterization of silica-coated Fe3O4 nanoparticles used as precursor of ferrofluids. *Applied Surface Science*, 255(6), pp.3485–3492.

Horsman, M.R. and Overgaard, J., 2007. Hyperthermia: a Potent Enhancer of Radiotherapy. *Clinical Oncology*, 19(6), pp.418–426.

Hoskins, C. et al., 2012. Dilemmas in the reliable estimation of the in-vitro cell viability in magnetic nanoparticle engineering: which tests and what protocols? *Nanoscale Research Letters*, 7(1), p.77.

Huang, H.-C. et al., 2009. Formulation of novel lipid-coated magnetic nanoparticles as the probe for in vivo imaging. *Journal of biomedical science*, 16(1), p.86.

Huh, Y.-M. et al., 2005. In Vivo Magnetic Resonance Detection of Cancer by Using Multifunctional Magnetic Nanocrystals. *Journal of the American Chemical Society*, 127(35), pp.12387–12391.

Hunter, R.J., Midmore, B.R. and Zhang, H., 2001. Zeta Potential of Highly Charged Thin Double-Layer Systems. *Journal of colloid and interface science*, 237(1), pp.147–149.

Indira, T., 2010. Magnetic Nanoparticles: A Review. *International Journal of Pharmaceutical*, 3(3), pp.1035–1042.

Itzkowitz S et al., 1992. Mucin associated Tn and sialosyl-Tn antigen expression in colorectal polyps. *Gut*, 33, pp.518–523.

Jahan, S.T. and Haddadi, A., 2015. Investigation and optimization of formulation parameters on preparation of targeted anti-CD205 tailored PLGA nanoparticles. *International Journal of Nanomedicine*, 10, pp.7371–7384.

Jeffery, G. et al., Vogel's text book of Quantitative Chemical Analysis, Fifth edition ed., Longman Scientific and Technical, New York, 1989.

Johannsen, M. et al., 2005. Clinical hyperthermia of prostate cancer using magnetic nanoparticles: Presentation of a new interstitial technique. *International Journal of Hyperthermia*, 21(7), pp.637–647.

Jordan, A. et al., 1996. Cellular uptake of magnetic fluid particles and their effects on human adenocarcinoma cells exposed to AC magnetic fields in vitro. *International journal of hyperthermia*, 12(6), pp.705–22.

Ju, T. et al., 2008. Human tumor antigens Tn and sialyl Tn arise from mutations in Cosmc. *Cancer Research*, 68(6), pp.1636–1646.

Julien, S. et al., 2001. Expression of Sialyl-Tn antigen in breast cancer cells transfected with the human CMP-Neu5Ac: GalNAc α2,6-sialyltransferase (ST6GalNAc I) cDNA. *Glycoconjugate Journal*, 18(11/12), pp.883–893.

Julien, S. et al., 2006. ST6GalNAc I expression in MDA-MB-231 breast cancer cells greatly modifies their O-glycosylation pattern and enhances their tumourigenicity. *Glycobiology*, 16(1), pp.54–64.

Julien, S., Videira, P.A. and Delannoy, P., 2012. Sialyl-Tn in cancer: (How) did we miss the target? *Biomolecules*, 2(4), pp.435–466.

Kandasamy, G. and Maity, D., 2015. Recent advances in superparamagnetic iron oxide nanoparticles (SPIONs) for in vitro and in vivo cancer nanotheranostics. *International Journal of Pharmaceutics*, 496(2), pp.191–218.

Kannagi, R. et al., 2008. Current relevance of incomplete synthesis and neo-synthesis for cancer-associated alteration of carbohydrate determinants-Hakomori's concepts revisited. *Biochimica et Biophysica Acta - General Subjects*, 1780(3), pp.525–531.

De Kanter, M. et al., 2016. Enabling the measurement of particle sizes in stirred colloidal suspensions by embedding dynamic light scattering into an automated probe head. *Measurement: Journal of the International Measurement Confederation*, 80, pp.92–98.

Kbari, A.A. et al., 2015. Influence of different synthesis conditions on properties of oleic acid-coated-Fe_3O_4 nanoparticles. *Materials Science*, 33(1), pp.100–106.

Kim, D. et al., 2001. Synthesis and characterization of surfactant-coated superparamagnetic monodispersed iron oxide nanoparticles. *Journal of Magnetism and Magnetic Materials*, (225), pp.30–36.

Kim, Y.J. and Varki, A., 1997. Perspectives on the significance of altered glycosylation of glycoproteins in cancer. *Glycoconjugate journal*, 14(5), pp.569–576.

Krishnan, K.M., 2010. Biomedical nanomagnetics: A spin through possibilities in imaging, diagnostics, and therapy. *IEEE Transactions on Magnetics*, 46(7), pp.2523–2558.

Kudelka, M.R. et al., 2015. Simple sugars to complex disease-mucin-type O-glycans in cancer. *Advances in Cancer Research*, 126, pp.53–135.

Lattuada, M. and Hatton, T.A., 2007. Functionalization of Monodisperse Magnetic Nanoparticles Functionalization of Monodisperse Magnetic Nanoparticles. , 23(4), pp.2158–2168.

Laurent, S. et al., 2008. Magnetic iron oxide nanoparticles: Synthesis, stabilization, vectorization, physicochemical characterizations and biological applications. *Chemical Reviews*, 108(6), pp.2064–2110.

Lee, J.H., Kim, J.W. and Cheon, J., 2013. Magnetic nanoparticles for multi-imaging and drug delivery. *Molecules and Cells*, 35(4), pp.274–284.

Lewinski, N., Colvin, V. and Drezek, R., 2008. Cytotoxicity of nanopartides. *Small*, 4(1), pp.26–49.

Li, L. et al., 2013. Superparamagnetic iron oxide nanoparticles as MRI contrast agents for non-invasive stem cell labeling and tracking. *Theranostics*, 3(8), pp.595–615.

Liao, S.H. et al., 2015. Functionalized magnetic iron oxide/alginate core-shell nanoparticles for targeting hyperthermia. *International Journal of Nanomedicine*, pp.3315–3328.

Liebert, M.A. et al., 2002. Ferromagnetic Self-Regulating Reheatable Thermal Rod Implants for in Situ Tissue Ablation. *Journal of Endourology*, 16(7).

Lim, J. et al., 2013. Characterization of magnetic nanoparticle by dynamic light scattering. *Nanoscale Research Letters*, 8(1), p.381.

Ling, D. and Hyeon, T., 2013. Chemical design of biocompatible iron oxide nanoparticles for medical applications. *Small*, 9(9–10), pp.1450–1466.

Liu, X. et al., 2006. Preparation and characterization of hydrophobic superparamagnetic magnetite gel. *Journal of Magnetism and Magnetic Materials*, 306(2), pp.248–253.

López-López, M.T. et al., 2008. Preparation and characterization of iron-based magnetorheological fluids stabilized by addition of organoclay particles. *Langmuir*, 24(14), pp.7076–7084.

Lopez Perez, J.A. et al., 1997. Advances in the preparation of magnetic nanoparticles by the microemulsion method. *Journal of Physical Chemistry B*, 101(41), pp.8045–8047.

Loureiro, L.R. et al., 2015. Challenges in antibody development against Tn and sialyl-Tn antigens. *Biomolecules*, 5(3), pp.1783–1809.

Mahdavi, M. et al., 2013. Synthesis, surface modification and characterisation of biocompatible magnetic iron oxide nanoparticles for biomedical applications. *Molecules*, 18(7), pp.7533–7548.

Mahmoudi, M. et al., 2011. Superparamagnetic iron oxide nanoparticles (SPIONs): Development, surface modification and applications in chemotherapy. *Advanced Drug Delivery Reviews*, 63(1–2), pp.24–46.

Maity, D. and Agrawal, D.C., 2007. Synthesis of iron oxide nanoparticles under oxidizing environment and their stabilization in aqueous and non-aqueous media. *Journal of Magnetism and Magnetic Materials*, 308(1), pp.46–55.

Majetich, S.A.et al., Magnetic nanoparticles. Edited by S. Gubin, First edition, Wiley-VCH Verlag GmbH and Co. KGaA, Weinheim, 2013.

Malhotra, A. and Coupland, J.N., 2004. The effect of surfactants on the solubility, zeta potential, and viscosity of soy protein isolates. *Food Hydrocolloids*, 18(1), pp.101–108.

Malvern, Zetasizer Nano User Manual, Malvern, Worcestershire, 2004.

Marcos, N.T. et al., 2011. ST6GalNAc-I controls expression of sialyl-Tn antigen in gastrointestinal tissues. *Frontiers in bioscience (Elite edition)*, 3, pp.1443–1455.

Mascolo, M.C., Pei, Y. and Ring, T.A., 2013. Room Temperature Co-Precipitation Synthesis of Magnetite Nanoparticles in a Large ph Window with Different Bases. *Materials*, 6(12), pp.5549–5567.

Massart R., Magnetic fluids and process for obtaining them, in: Agence Nationale de Valorisation de la Recherche (ANVAR) (Ed.), France, 1980.

Mejias, R. et al., 2010. Liver and brain imaging through dimercaptosuccinic acid-coated iron oxide nanoparticles. *Nanomedicine*, 5(3), pp.397–408.

Mejías, R. et al., 2011. Dimercaptosuccinic acid-coated magnetite nanoparticles for magnetically guided in vivo delivery of interferon gamma for cancer immunotherapy. *Biomaterials*, 32(11), pp.2938–2952.

Mikhaylova, M. et al., 2004. BSA Immobilization on Amine - Functionalized Superparamagnetic Iron Oxide Nanoparticles. , (6), pp.2344–2354.

Miles, D.W. et al., 1994. Expression of sialyl-Tn predicts the effect of adjuvant chemotherapy in node-positive breast cancer. *British journal of cancer*, 70(6), pp.1272–5.

Moremen, K.W., Tiemeyer, M. and Nairn, A. V., 2012. Vertebrate protein glycosylation: diversity, synthesis and function. *Nature Reviews Molecular Cell Biology*, 13(7), pp.448–462.

Mosmann, T., 1983. Rapid colorimetric assay for cellular growth and survival: Application to proliferation and cytotoxicity assays. *Journal of Immunological Methods*, 65(1–2), pp.55–63.

Munkley, J., 2016. The role of sialyl-Tn in cancer. *International Journal of Molecular Sciences*, 17(3).

Ormerod, M.., 2008. Flow Cytometry - A Basic Introduction. Available at: http://flowbook.denovosoftware.com/ [Accessed August 12, 2017].

Osako, M. et al., 1993. Immunohistochemical study of mucin carbohydrates and core proteins in human pancreatic tumors. *Cancer*, 71(7), pp.2191–2199.

Palma, S.I.C.J. et al., 2015. Effects of phase transfer ligands on monodisperse iron oxide magnetic nanoparticles. *Journal of Colloid and Interface Science*, 437, pp.147–155.

Picot, J. et al., 2012. Flow cytometry: retrospective, fundamentals and recent instrumentation. *Cytotechnology*, 64(2), pp.109–130.

Pinho, S. et al., 2007. Biological significance of cancer-associated sialyl-Tn antigen: Modulation of malignant phenotype in gastric carcinoma cells. *Cancer Letters*, 249(2), pp.157–170.

Pinho, S.S. and Reis, C.A., 2015. Glycosylation in cancer: mechanisms and clinical implications. *Nature Reviews Cancer*, 15(9), pp.540–555.

Pisanic, T.R. et al., 2007. Nanotoxicity of iron oxide nanoparticle internalization in growing neurons. *Biomaterials*, 28(16), pp.2572–2581.

Portet, D. et al., 2001. Nonpolymeric coatings of iron oxide colloids for biological use as magnetic resonance imaging contrast agents. *Journal of Colloid and Interface Science*, 238, pp.37–42.

R. Nordén, Leukocyte Migration over the Endothelial Wall. *Herpesvirus-Induced Glycans. (n.d.).* Available at: http://www.glycopedia.eu/e-chapters/herpesvirus-induced-glycans/Leukocyte-Migration-over-the [Accessed September 1, 2017].

Rebodos, R.L. and Vikesland, P.J., 2010. Effects of oxidation on the magnetization of nanoparticulate magnetite. *Langmuir*, 26(22), pp.16745–16753.

Reddy, L.H. et al., 2012. Magnetic nanoparticles: Design and characterization, toxicity and biocompatibility, pharmaceutical and biomedical applications. *Chemical Reviews*, 112(11), pp.5818–5878.

Reis, C.A. et al., 2010. Alterations in glycosylation as biomarkers for cancer detection. *Journal of Clinical Pathology*, 63(4), pp.322–329.

Reis, M.A.G., 2014. *Produção de anticorpos para tratamento do cancro da mama*. Faculdade de Ciências e Tecnologia, Universidade Nova de Lisboa.

Revia, R.A. and Zhang, M., 2016. Magnetite nanoparticles for cancer diagnosis, treatment, and treatment monitoring: recent advances. *Materials today (Kidlington, England)*, 19(3), pp.157–168.

Riemer, J. et al., 2004. Colorimetric ferrozine-based assay for the quantitation of iron in cultured cells. *Analytical Biochemistry*, 331(2), pp.370–375.

Ruiz, A. et al., 2014. Magnetic nanoparticles coated with dimercaptosuccinic acid: development, characterization, and application in biomedicine. *Journal of Nanoparticle Research*, 16(11).

Rümenapp, C., Gleich, B. and Haase, A., 2012. Magnetic nanoparticles in magnetic resonance imaging and diagnostics. *Pharmaceutical Research*, 29(5), pp.1165–1179.

Russo, R. et al., 2012. Nanoparticle magnetization measurements by a high sensitive nano-superconducting quantum interference device. *Applied Physics Letters*, 101(12), pp.1–5.

Ryu, J.H. et al., 2014. Theranostic nanoparticles for future personalized medicine. *Journal of Controlled Release*, 190, pp.477–484.

Salgin, S., Salgin, U. and Bahadir, S., 2012. Zeta potentials and isoelectric points of biomolecules: The effects of ion types and ionic strengths. *International Journal of Electrochemical Science*, 7(12), pp.12404–12414.

Schauer, R., 2000. Achievements and challenges of sialic acid research. *Glycoconjugate Journal*, 17, pp.485–499.

Schoonbroodt, S. et al., 2008. Engineering antibody heavy chain CDR3 to create a phage display Fab library rich in antibodies that bind charged carbohydrates. *Journal of immunology (Baltimore, Md. : 1950)*, 181(9), pp.6213–6221.

Schultz, M.J., Swindall, A.F. and Bellis, S.L., 2012. Regulation of the metastatic cell phenotype by sialylated glycans. *Cancer Metastasis Rev.*, 31, pp.501–518.

Scientific, T., Carbodiimide Crosslinker Chemistry. Available at: https://www.thermofisher.com/pt/en/home/life-science/protein-biology/protein-biology-learning-center/protein-biology-resource-library/pierce-protein-methods/carbodiimide-crosslinker-chemistry.html [Accessed September 28, 2017].

Shire S. J. et al., Volume XI: Current Trends in Monoclonal Antibody Development and Manufacturing, Springer, New York, 2010.

Singh, N. et al., 2010. Potential toxicity of superparamagnetic iron oxide nanoparticles (SPION). *Nano Reviews*, 1(1), p.5358.

Soares, P. et al., 2015. Thermal and magnetic properties of iron oxide colloids: influence of surfactants. *Nanotechnology*, 26(42), p.425704.

Soares, P.I.P. et al., 2014. Effects of surfactants on the magnetic properties of iron oxide colloids. *Journal of Colloid and Interface Science*, 419, pp.46–51.

Soares, P.I.P. et al., 2016. Iron oxide nanoparticles stabilized with a bilayer of oleic acid for magnetic hyperthermia and MRI applications. *Applied Surface Science*, 383, pp.240–247.

Song, M. et al., 2012. Influence of morphology and surface exchange reaction on magnetic properties of monodisperse magnetite nanoparticles. *Colloids and Surfaces A: Physicochemical and Engineering Aspects*, 408, pp.114–121.

Sperling, R.A. and Parak, W.J., 2010. Surface modification, functionalization and bioconjugation of colloidal inorganic nanoparticles. *Philosophical Transactions of the Royal Society A: Mathematical, Physical and Engineering Sciences*, 368(1915), pp.1333–1383.

Springer, G., 1984. T and Tn, general carcinoma autoantigens. *Science*, 224(4654), pp.1198–1206.
Steen, P. Van den et al., 1998. Concepts and Principles of *O*-Linked Glycosylation. *Critical Reviews in Biochemistry and Molecular Biology*, 33(3), pp.151–208.

Stuart, B.H., *Infrared Spectroscopy: Fundamentals and Applications*, First Edition, Analytical Techniques in the Sciences, Wiley, 2004.

Sun, C., Lee, J.S.H. and Zhang, M., 2008. Magnetic nanoparticles in MR imaging and drug delivery. *Advanced Drug Delivery Reviews*, 60(11), pp.1252–1265.

Swanson H. E., Standard x-ray diffraction powder patterns, U.S. Dept. of Commerce For sale by the Supt. of Docs., U.S. G.P.O., Washington, DC, 1972.

Talelli, M. et al., 2009. Superparamagnetic iron oxide nanoparticles encapsulated in biodegradable thermosensitive polymeric micelles: Toward a targeted nanomedicine suitable for image-guided drug delivery. *Langmuir*, 25(4), pp.2060–2067.

Tao, Y.T., 1993. Structural Comparison of Self-Assembled Monolayers of n-Alkanoic Acids on the Surfaces of Silver, Copper, and Aluminum. *Journal of the American Chemical Society*, 115(10), pp.4350–4358.

Tartaj, P. et al., 2011. The iron oxides strike back: From biomedical applications to energy storage devices and photoelectrochemical water splitting. *Advanced Materials*, 23(44), pp.5243–5249.

Teja, A.S. and Koh, P.Y., 2009. Synthesis, properties, and applications of magnetic iron oxide nanoparticles. *Progress in Crystal Growth and Characterization of Materials*, 55(1–2), pp.22–45.

Theophanides, T., 2012. *Introduction to Infrared Spectroscopy* Infrared S. I. 978-953-51-0537-4 Prof. Theophanides Theophile (Ed.), ed., Available at: http://www.intechopen.com/books/infrared-spectroscopy-materials-scienceengineering-%0Aand-technology/introduction-to-infrared-spectroscopy.

Tombácz, E. et al., 2013. Adsorption of organic acids on magnetite nanoparticles, pH-dependent colloidal stability and salt tolerance. *Colloids and Surfaces A: Physicochemical and Engineering Aspects*, 435, pp.91–96.

US National Center For Health Statistics, Leading Causes of Death. *Heal. United States, 2015 With Spec. Featur. Racial Ethn. Heal. Disparities*. Available at: https://www.cdc.gov/nchs/fastats/leading-causes-of-death.htm [Accessed August 30, 2017].

Vacchelli, E. et al., 2014. Trial watch: Monoclonal antibodies in cancer therapy. *Oncoimmunology*, 3(1), p. e22789.

Valenzuela, R. et al., 2009. Influence of stirring velocity on the synthesis of magnetite nanoparticles (Fe3O4) by the co-precipitation method. *Journal of Alloys and Compounds*, 488(1), pp.227–231.

Varki, A., 1993. Biological roles of oligosaccharides: all of the theories are correct. *Glycobiology*, 3(2), pp.97–130.

Varki, A., Esko, J. and Colley. K., Cellular Organization of Glycosylation, in: A. Varki, R.D. Cummings, J.D. Esko, H.H. Freeze, P. Stanley, C.R. Bertozzi, G.W. Hart, M.E. Etzler (Eds.), Essentials Glycobiol., 2nd ed., Cold Spring Harbor (NY): Cold Spring Harbor Laboratory Press. Available from: http://www.ncbi.nlm.nih.gov/books/NBK1926/, 2009.

Varki, A., and Lowe, J., Biological Roles of Glycans, in: A. Varki, R.D. Cummings, J.D. Esko, H.H. Freeze, P. Stanley, C.R. Bertozzi, G.W. Hart, M.E. Etzler (Eds.), Essentials Glycobiol., 2nd ed., Cold Spring Harbor (NY): Cold Spring Harbor Laboratory Press. Available from: http://www.ncbi.nlm.nih.gov/books/NBK1897, 2009.

Varki, A. and Schauer, R., 2009. *Sialic Acids* 2nd ed., Cold Spring Harbor Laboratory Press. Available at: http://www.ncbi.nlm.nih.gov/pubmed/20301246.

Villanueva, A. et al., 2009. The influence of surface functionalization on the enhanced internalization of magnetic nanoparticles in cancer cells. *Nanotechnology*, 20(11), p.115103.

Wahajuddin and Arora, S., 2012. Superparamagnetic iron oxide nanoparticles: Magnetic nanoplatforms as drug carriers. *International Journal of Nanomedicine*, 7, pp.3445–3471.

Wang, Y.-X.J. et al., 2012. Enhanced cellular uptake of aminosilane-coated superparamagnetic iron oxide nanoparticles in mammalian cell lines. *International Journal of Nanomedicine*, p.953.

Waseda, Y., Matsubara, E. and Shinoda, K., *X-ray Diffraction Crystallography*. First edition, Springer, S. H. D. L. N. York, 2011.

Wilhelm, C. et al., 2003. Intracellular uptake of anionic superparamagnetic nanoparticles as a function of their surface coating. *Biomaterials*, 24(6), pp.1001–1011.

Wilhelm, C. and Gazeau, F., 2008. Universal cell labelling with anionic magnetic nanoparticles. *Biomaterials*, 29(22), pp.3161–3174.

Willard, M.A. et al., 2004. Chemically prepared magnetic nanoparticles. *International Materials Reviews*, 49(3–4), pp.125–170.

Williams, D.B. and Carter, C.B., *Transmission electron microscopy: a text book for materials science*. First edition, Springer Science, New York, 2009.

World Health Organization, 2015. Cancer Key Facts. *Fact Sheet no297*. Available at: http://www.who.int/mediacentre/factsheets/fs297/en/ [Accessed August 30, 2017].

Wormuth, K., 2001. Superparamagnetic latex via inverse emulsion polymerization. *Journal of Colloid and Interface Science*, 241, pp.366–377.

Wu, W., He, Q. and Jiang, C., 2008. Magnetic iron oxide nanoparticles: Synthesis and surface functionalization strategies. *Nanoscale Research Letters*, 3(11), pp.397–415.

Wu, Y. et al., 2015. Magnetic Nanoparticle for Biomedicine Applications. *Journal of Nanotechnology: Nanomedicineand Nanobiotechnology*, 1(1), pp.1–5.

Xie, H. et al., 2011. Lactoferrin-conjugated superparamagnetic iron oxide nanoparticles as a specific MRI contrast agent for detection of brain glioma in vivo. *Biomaterials*, 32(2), pp.495–502.

Yallapu, M.M. et al., 2011. Multi-functional magnetic nanoparticles for magnetic resonance imaging and cancer therapy. *Biomaterials*, 32(7), pp.1890–1905.

Yallapu, M.M. et al., 2010. PEG-functionalized magnetic nanoparticles for drug delivery and magnetic resonance imaging applications. *Pharmaceutical Research*, 27(11), pp.2283–2295.

Yang, C.Y. et al., 2009. Labeling of human mesenchymal stem cell: Comparison between paramagnetic and superparamagnetic agents. *Journal of Applied Physics*, 105(7), pp.5–8.

Yang, K. et al., 2010. Re-examination of characteristic FTIR spectrum of secondary layer in bilayer oleic acid-coated Fe3O4 nanoparticles. *Applied Surface Science*, 256(10), pp.3093–3097.

Yu, L.G., 2007. The oncofetal Thomsen-Friedenreich carbohydrate antigen in cancer progression. *Glycoconjugate Journal*, 24(8), pp.411–420.

Yuen, A.K.L. et al., 2012. The interplay of catechol ligands with nanoparticulate iron oxides. *Dalton Transactions*, 41(9), p.2545.

Zhang, L. et al., 2015. DMSA-Coated Iron Oxide Nanoparticles Greatly Affect the Expression of Genes Coding Cysteine-Rich Proteins by Their DMSA Coating. *Chemical Research in Toxicology*, 28(10), pp.1961–1974.

Zhang, L., He, R. and Gu, H.C., 2006. Oleic acid coating on the monodisperse magnetite nanoparticles. *Applied Surface Science*, 253(5), pp.2611–2617.

Zhang, S. et al., 2009. The effect of iron oxide magnetic nanoparticles on smooth muscle cells. *Nanoscale Research Letters*, 4(1), pp.70–77.

Zhang, Y.-Q. et al., 2016. Toxicity of dimercaptosuccinate-coated and un-functionalized magnetic iron oxide nanoparticles towards aquatic organisms. *Environ. Sci.: Nano*, 3(4), pp.754–767.

Appendix

Appendix I

Symbol and Text Nomenclature for Representation of Glycan Structure (Consortium for Functional Glycomics 2012)

(as selected by the Nomenclature Committee Consortium of Functional Glycomics, based on a version originally put forth by Stuart Kornfeld and later adapted by the editors of the textbook Essentials of Glycobiology (Cold Spring Harbor Laboratory Press)

Symbol Nomenclature (Figure 10.1):

- The symbol nomenclature must be convenient for the annotation of mass spectra. To this end, it was decided that:

- Each sugar type (i.e. sugars of the same mass: hexose, hexosamine and *N*-acetylhexosamine), should have the same symbol shape;

- Isomers of each sugar type (e.g. mannose/galactose/glucose) should be differentiated by color or by black/white/shading;

- Where possible, the same color or shading should be used for derivatives of hexose (e.g. the corresponding *N*-acetylhexosamine and hexosamine);

- Representing different sugars using the same shape but different orientation should be avoided so that structures can be represented either horizontally or vertically.

- Colored symbols should still appear distinguishable when copied or printed in black and white;
- Considering 10% of the population is color blind, the use of both red and green for the same shaped symbols should be avoided;
- When desired, linkage information can be represented in text next to a line connecting the symbols (e.g. alpha4, beta4).

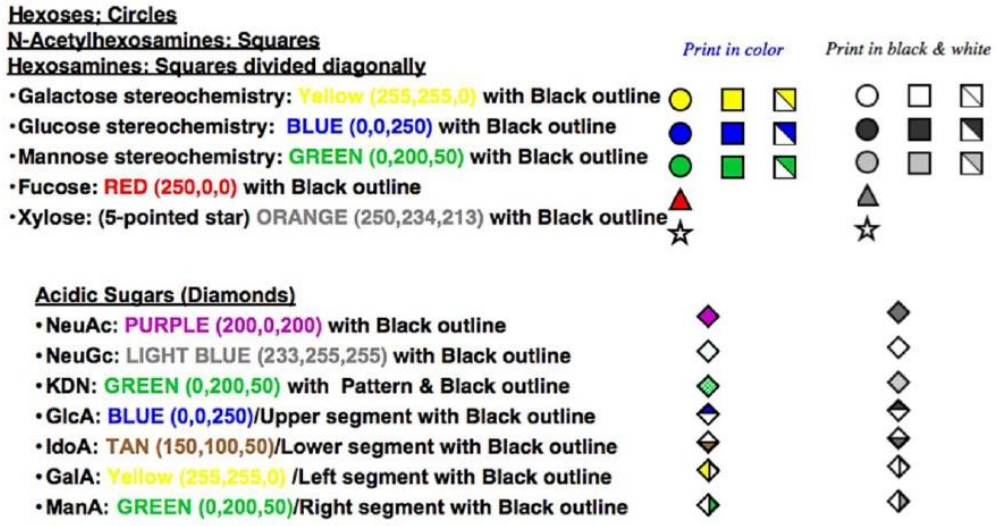

Figure 10.1. Symbol nomenclature adopted for glycan structures.

Text Nomenclature (Figure 10.2):

- A 'modified International Union of Pure and Applied Chemistry (IUPAC) condensed' text nomenclature, which includes the anomeric carbon but not the parentheses, and which can be written in either a linear or 2D version is recommended:

- Including the anomeric carbon is important, and is likely to become increasingly more so in the future as more complicated structures are discovered;

- The presence of parentheses (which then necessitates the use of brackets to indicate branching structures) is unnecessarily cumbersome, particularly when representing the structure in 2D form.

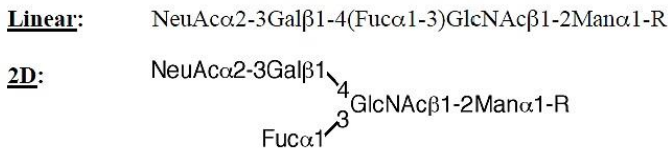

Figure 10.2. Text nomenclature adopted for glycan structures, both linear and 2D (Consortium for Functional Glycomics 2012).

Appendix II

Table 10.1. Monoclonal antibodies currently approved for cancer treatment. Adapted from (Vacchelli *et al.* 2014; Shire *et al.* 2010).

mAb (trade name)	**Antigen**	**Approval date**	**Type**	**Indications**	**Company**
Alemtuzumab (*Campath*)	CD52	2001	Hz IgG1	CLL	Genzyme
Bevacizumab (*Avastin*)	VEGF	2004	Hz IgG1	Glioblastoma multiform, colorectal, renal and lung cancer	Genentech/ Roche
Brentuximab vedotin (Adcetris)	CD30	2011	Ch IgG1	Hodgkin and anaplastic large cell lymphoma (coupled to MMAE)	Seattle Genetics
Catumaxomab (*Removab*)	CD3 Ep-CAM	2009	Murine-Rat hybrid	Malignant ascites in patients with EpCAM+ cancer	Fresenius Biotech/ Trion Pharma
Cetuximab (*Erbitux*)	EGFR	2004	Chimeric IgG1	Head and neck and colo-rectal cancer	Bristol-Meyers Squibb
Denosumab (*Prolia, Xgeva*)	RANKL	2011	H IgG2	Breast and prostate carcinoma	Amgen
Gemtuzumab (*Mylotarg*)	CD33	2000	Hz IgG4	Acute myeloid leukemia (coupled with cali-cheamicin)	Wyeth

Ibritumomab tiuxetan (*Zevalin*)	CD20	2002	Murine IgG1	NHL (coupled with 90Y or 111In)	IDEC Pharma-ceuticals
Ipilimumab (*Yervoy*)	CTLA-4	2011	Human IgG1	Melanoma	Bristol-Myers Squibb
Panitumumab (*Vectibix*)	EGFR	2006	H IgG2	Colorectal carcinoma	Amgen
Pertuzumab (*Perjeta, Omni-targ*)	HER2	2012	Hz IgG1	Breast cancer	Genen-tech/Roche
Obinutuzumab (*Gazyva, Gazyvaro*)	CD20	2013	Hz IgG1	CLL	Roche
Ofatumumab (*Arzerra*)	CD20	2009	H IgG1	CLL	Glax-oSmithKline
Rituximab (*Rituxan*)	CD20	1997	Ch IgG1	CLL and NHL	Roche
Tositumomab (*Bexxar*)	CD20	2003	H IgG1	NHL (naked or coupled with 131I)	Glax-oSmithKline
Trastuzumab (*Herceptin*)	HER2	1998	Hz IgG1	Breast carcinoma and gastric or gastroesopha-geal junction cancer	Genentech

Ch, chimeric; CLL, Chronic lymphocytic leukemia, CTLA-4, cytotoxic T lymphocyte antigen 4; EGFR, epidermal growth factor receptor; EpCAM, epithelial cell adhesion molecule; H, human; Hz, humanized; MMAE, monomethyl auristatin E; NHL, Non-Hodgkin lymphoma; RANKL, receptor activator of NFκB ligand; VEGF, vascular endothelial growth factor.

Appendix III

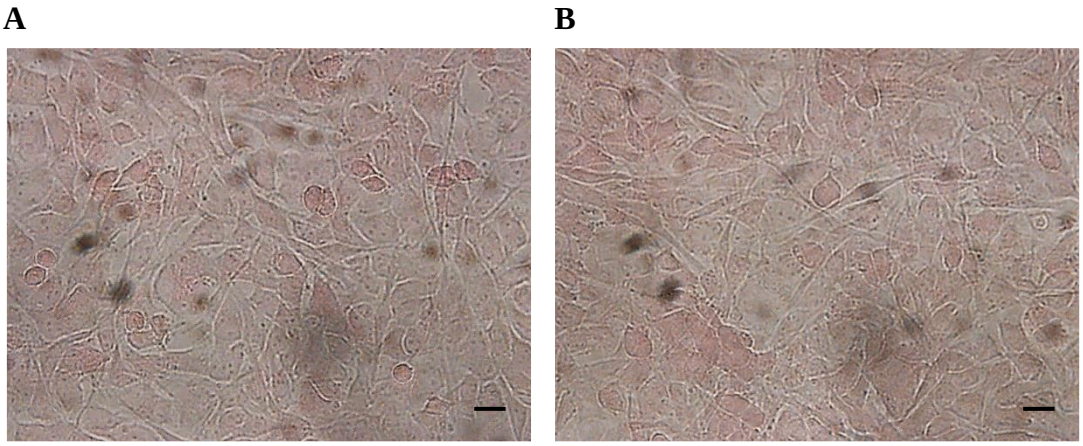

Figure 10.3. Bright field microscopy visualization of MDA-MB-231 WT (A) and MDA-MB-231 (B). A 50x objective magnification was used. Scale bar for both images represents 20 μm.